Dissertation

submitted to the

Combined Faculties of the Natural Sciences and Mathematics

of the Ruperto-Carola-University of Heidelberg, Germany

for the degree of

Doctor of Natural Sciences

put forward by

M. Sc. Niklas Michel

born in Salzkotten, Germany

Oral examination: February 6th, 2019

Nuclear structure effects in heavy atomic systems

Referees: Honorarprof. Dr. Christoph H. Keitel

PD Dr. Wolfgang Quint

Zusammenfassung

In dieser Arbeit werden im Rahmen der Quantenelektrodynamik gebundener Zustände verschiedene Einflüsse der Kernstruktur auf die Spektren wasserstoffartiger Systeme untersucht. Im ersten Teil dieser Arbeit wird der g-Faktor des gebundenen Elektrons untersucht, welcher von der Form der Ladungsverteilung im Atomkern abhängt. Ein numerischer, nicht-perturbativer Ansatz für die Berechnung der entsprechenden Kernformkorrektur zum g-Faktor wird vorgestellt und Implikationen für die Unsicherheiten theoretischer Vorhersagen werden diskutiert. Im Besonderen kann die Modellabhängigkeit der Kerngrößenkorrektur zum g-Faktor durch Nutzen von Informationen über die verformte Ladungsverteilung des Kerns verringert werden. Im zweiten Teil geht as um die Struktur gebundener Zustände zwischen einem Myon und einem Atomkern, sogenannter myonische Atome. Hierbei werden hochpräzise Berechnungen der Übergangsenergien und -wahrscheinlichkeiten mit zeitgemäßen numerischen Methoden durchgeführt. Des weiteren werden neue Methoden für die Berechnung von Korrekturen höherer Ordnung zu der Hyperfeinstruktur präsentiert. Dies beinhaltet eine vollständige Berechnung der Hyperfeinaufspaltung zweiter Ordnung und Korrekturen aufgrund von Vakuumpolarisationseffekten für Quadrupoleverteilungen im Innern des Atomkerns. Es werden hochpräzise Berechnungen des g-Faktors des gebundenen Myons in ^{4}He duchrgeführt und in Verbindung mit kürzlich durchgeführten Experimenten wird das Quadrupolemoment von ^{185}Re und ^{187}Re Kernen ermittelt.

Abstract

In this thesis, several aspects of nuclear structure effects in the spectra of hydrogen-like systems are investigated in the framework of bound-state quantum electrodynamics. The first part of this thesis is about the g factor of a bound electron, which depends on the shape of the nuclear charge distribution. A numerical, non-perturbative approach for the calculation of the corresponding nuclear shape correction is presented and implications for the uncertainties of theoretical predictions are discussed. In particular, the model-uncertainty of the finite-nuclear-size correction to the g factor can be reduced using information on the deformed charge distribution. The second part is about the structure of bound states between a muon and an atomic nucleus, so called muonic atoms. Here, high-precision calculations for transition energies and probabilities are presented, using up-to-date numerical methods. Furthermore, new methods for the calculation of higher order corrections for the hyperfine structure are presented. This includes a complete calculation of the second order hyperfine structure and leading order vacuum polarization corrections for extended electric quadrupole distributions inside the nucleus. High-precision calculations for the bound-muon g factor in ^{4}He are perfomed and in connection with recent measurements on muonic atoms, the nuclear quadrupole moment of ^{185}Re and ^{187}Re is extracted.

The following articles covered by this thesis have been published in peer-reviewed journals or have been submitted for publication:

- Niklas Michel, Natalia S. Oreshkina, Christoph H. Keitel
  Theoretical prediction of the fine and hyperfine structure of heavy muonic atoms
  Phys. Rev. A. **96**, 032510 (2017) (Ref. [1])

- Bastian Sikora, Halil Cakir, Niklas Michel, Vincent Debierre, Natalia S. Oreshkina, Nikolay A. Belov, Vladimir A. Yerokhin, Christoph H. Keitel, Zoltán Harman
  Improving the accuracy of the muon mass and magnetic moment anomaly via the bound-muon g factor
  Phys. Rev. D. **97**, 111301(R) (2018) (Ref. [2])

- Niklas Michel, Natalia S. Oreshkina
  Higher-order corrections for the dynamic hyperfine structure of muonic atoms
  submitted, arXiv:1809.06623 (2018) (Ref. [3])

- Niklas Michel, Jacek Zatorski, Natalia S. Oreshkina, Christoph H. Keitel
  Non-perturbative analysis of nuclear shape effects on the bound electron g factor
  submitted, arXiv:1806.00405 (2018) (Ref. [4])

In addition, the following article is in preparation:

- A. Adamczak, A. Antognini, K. Kirch., N. Ritjoho, A. Skawaran, N. Berger, R. Pohl, F. Wauters, T. E. Cocolios, N. Seveijns, R. Dressler, R. Eichler, A. Knecht, A. Papa, E. Rapisarda, P. Indelicato, K. Jungmann, L. Willmann, N. Michel, N. S. Oreshkina, C. H. Keitel, M. Pospelov, P. Reiter, S. Roccia
  On the analysis of the hyperfine splitting in muonic spectra: Re-185 and Re-187
  in preparation (Ref. [5])

Moreover, the following article not covered by this thesis has been published:

- Natalia S. Oreshkina, Stefano M. Cavaletto, Niklas Michel, Zoltán Harman, Christoph H. Keitel
  Hyperfine splitting in simple ions for the search of the variation of fundamental constants
  Phys. Rev. A. **96**, 030501(R) (2017) (Ref. [6])

Contents

Introduction

Advances in the field of spectroscopy have always given new insights in the physical laws which govern our world at the smallest scales. The first observation of a discrete absorption spectrum was due to Wollaston in 1802 [7] and Fraunhofer in 1814 [8], who discovered the Fraunhofer lines in the spectrum of the sun independently from each other. In the following decades, the emission spectra of different elements were explored. Especially noteworthy are the systematic investigations by Kirchhoff and Bunsen [9, 10]. It became apparent that elements can be identified by their characteristic spectrum and that laboratory emission spectra are connected to astrophysical absorption spectra [11]. Since the hydrogen atom consists of only one electron bound to a single proton, it has the simplest spectrum and therefore was particularly important for the development of theoretical models. It was recognized by Balmer in 1885 [12] that the position of spectral lines as measured by Ångström [13], Huggins [14], and Vogel [15] could be described with surprising accuracy by a simple formula. This was generalized later in terms of the Rydberg formula [16, 17]. It contains the Balmer series as a special case and also predicts the Lyman, Paschen, Brackett, Pfund, and Humphreys series, which were confirmed subsequently by experiments [18–22]. However, the Rydberg formula is purely empirical, without an underlying theoretical framework.

Additionally, the electron was discovered by the investigation of cathode rays [23, 24] and Rutherford scattering showed that the positive charge and almost the entire mass of an atom is concentrated in its center in form of an atomic nucleus [25]. Also, the spectral density of black-body radiation was explained by Planck using the quantum hypothesis [26]. This motivated the Bohr model of the atom [27], where the electron can orbit the nucleus only on certain quantized orbits. Compared to the previous Thomson [28] and Rutherford model, now the Rydberg formula and thereby the hydrogen spectrum could be derived and the discrete energies could be expressed in terms of the fine-structure constant α, the electron mass m_e, and the speed of light c. A relativistic extension is the Bohr-Sommerfeld model [29], which explains also finer features of the hydrogen spectrum. However, despite the success of describing the quantized energies, the Bohr-Sommerfeld model has difficulties with the generalization to many-electron systems. A consistent theoretical framework for non-relativistic atomic theory, also for more complicated atoms, was finally obtained with the Schrödinger equation [30–33] and matrix mechanics [34–36], which were shown to be an equivalent formulation of quantum theory [37]. Due to the Zeeman effect [38], spectral lines of atoms exposed to magnetic fields are split into sublevels. This could only be explained consistently by assigning, besides the orbital angular momentum, also the spin angular momentum to the electron [39]. The Dirac equation [40] incorporates the electron's spin naturally and predicts that the corresponding magnetic moment due to spin is twice as big compared to orbital angular momentum. Additionally, it obeys the laws of special relativity and negative energy

states occur, which led to the prediction of the positron, the electron's antiparticle. The negative energy states also lead to problems with the one-particle interpretation of the Dirac equation due to phenomena like Zitterbewegung or Klein's paradox [41].

Two experimental results pointed out that the Dirac equation, despite its success in describing the energy levels of the hydrogen atom, could not be the end of the story for the theory of atomic structure. The Dirac equation for a point-like nucleus predicts that two energy levels with the same total angular momentum are degenerate [42]. Therefore, the $2s1/2$ and $2p1/2$ levels should be degenerate according to Dirac's theory. However, Lamb and Retherford showed that they are separated by about $1060\,\text{MHz}$ by driving the transition directly with radio waves [43]. On the other hand, anomalies in the magnetic hyperfine structure of hydrogen and deuterium [44] as well as sodium and gallium [45,46] were revealed. Both phenomena were explained in the framework of quantum electrodynamics (QED) [47], which results in small corrections to the energy levels in atoms and the magnetic moment of the electron. To this date, the comparison of experiment and theory for the hyperfine and Zeeman splitting in simple atomic systems keeps challenging QED and delivering values for fundamental physical constants [48]. The following two paragraphs describe more recent developments in this field.

The magnetic moment of the electron is commonly expressed by the dimensionless gyromagnetic factor, or g factor, which is the proportionality constant between magnetic moment and angular momentum. The g factor of the free electron provides a stringent test of QED without an external electromagnetic field. It was measured with an uncertainty below the part-per-trillion level [49,50] and predicted to order α^5 theoretically, eg. [51–54]. A combination of experiment and theory allowed the extraction of the fine-structure constant α on the parts-per-billion level [55,56].

The g factor of the electron can also be measured and theoretically calculated to an extraordinary precision in case of the bound electron in a hydrogen-like (H-like) ion. Here, QED can be tested in the regime of high background fields, since the electron is exposed to the nuclear Coulomb potential. It has been measured for H-like $^{12}_{6}\text{C}^{5+}$ [57,58], $^{16}_{8}\text{O}^{7+}$ [59], and $^{28}_{14}\text{Si}^{13+}$ [60] on the part-per-billion level with Penning trap experiments using a single ion during the *Mainz g-Factor Experiment*. A Penning trap is a device for trapping charged particles with a combination of a static electric quadrupole field and a homogeneous magnetic field [61]. For these measurements, at least two Penning traps are used [62].

Two experiments aim at measuring the bound electron g factor in H-like ions also for very high charge numbers. The *ALPHATRAP* experiment [63] uses a measurement scheme with two Penning traps similar to the *Mainz g-Factor Experiment*. Now, the ions are not created in situ but can be injected from external sources, like the *Heidelberg EBIT* (electron-beam ion trap). In this way, g factors of ions up to H-like $^{208}\text{Pb}^{81+}$ can be investigated with an expected accuracy of 10 parts-per-trillion [63]. The *ARTEMIS* experiment [63,64] will use microwaves to excite transitions between Zeeman sublevels in highly charged ions. In this way, ionic and bound electron g factors can be accessed. With connection to the *HITRAP* beamline, the heaviest hydrogen-like ions, e.g. U^{91+}, will be available [65].

The precision experiments on the bound electron g factor demand theoretical calcu-

lations on a competing level of accuracy. The interaction of a bound electron with the atomic nucleus is characterized by the parameter $Z\alpha$, where Z is the nuclear charge number and $\alpha \approx 1/137$ is the fine-structure constant. For light nuclei, $Z\alpha$ is a small parameters and a power-series expansion is feasible. On the other hand, for heavy nuclei $Z\alpha$ is on the order of unity and results have to be obtained including the nuclear Coulomb potential to all orders. The leading contribution to the binding corrections of the bound-electron g factor is due to the point-like Coulomb potential and has been obtained by Breit [66]. The one- and two-loop vacuum-polarization (VP) and self-energy (SE) corrections have been obtained to order $(Z\alpha)^4$ in Refs. [67–70]. Two-loop corrections to order $(Z\alpha)^5$ have been recently presented in Ref. [71]. The most precise one-loop QED correction for the SE to all orders in $Z\alpha$ has been calculated in Ref. [72]. Two-loop calculations to all orders in $Z\alpha$ have not been completed to date. The have been presented for two VP loops and mixed VP-SE in Ref. [73], and for the SE loop-after-loop terms in Ref. [74].

Furthermore, nuclear effects beyond the point-like Coulomb potential have to be considered. Although the nucleus is much smaller than the typical extend of the electron wave function, it is an extended object and correspondingly, the Coulomb potential is modified at small distanced. This causes the finite nuclear size correction to the g factor of the bound electron. The relativistic analytic formula for this has been given in Ref. [75] and the corresponding non-relativistic limit in Ref. [67]. In two-photon exchanges, also excited nuclear states contribute and the nuclear polarization corrections have been considered in Refs. [76,77]. So far, all effects calculations assumed an infinitely heavy nuclei, which is not moving. The nuclear recoil corrections account for the finite nuclear mass. Here, besides α for QED loops and $Z\alpha$ for interactions with the nuclear potential, there is the additional expansion parameter m_e/M, where m_e is the electron mass and M is the nuclear mass. To order $\alpha(Z\alpha)^2(m_e/M)^2$, results can be found in Refs. [78] and to all orders in m_e/M and first order in $Z\alpha$ in Ref. [79]. Suitable for heavy ions, the recoil correction to first order in m_e/M, but all orders in $Z\alpha$, is given in Ref. [80, 81]. In Ref. [82], the nuclear shape effect, also called nuclear deformation effect, was introduced for spinless nuclei, which takes a deformed nuclear charge distribution into account. It is not important for light nuclei, but scales strongly with the nuclear charge and therefore becomes important for high Z.

The combination of theory and experiment for the bound electron g factor in $^{12}_{6}$C provided an improved value of the electron mass [58,83]. For $^{28}_{14}$Si [60], it was shown as a proof-of-principle that nuclear parameters like the RMS charge radius can be obtained. Extracting nuclear magnetic moments was suggested theoretically [84,85]. Also, it was argued that an independent and more accurate value for the fine-structure constant can be obtained [86,87]. With the upcoming experiments in the high-Z regime, further tests of QED in stong fields, information on nuclear parameters, and extraction of fundamental constants can be expected, and updated theoretical calculations especially for heavy nuclei are needed.

For further studies of H-like systems, either the atomic nucleus or the bound electron can be exchanged for another charged particle. This establishes the field of research on *exotic atoms*. Depending on the type of considered particles, nuclear structure effects can either

be avoided or enhanced. Bound states between two leptons are not affected by the strong interaction or nuclear effects and are therefore suitable for testing bound state QED. One example is positronium [88], a bound state between an electron and its antiparticle, the positron. The energy levels were studied up to order α^6 [89–92] and measured on a 10^{-4} up to 10^{-9} level, e.g. [93–97], despite a life time in the range of 10^{-9}s due to pair annihilation. Another interesting leptonic system is muonium [98], a bound state consisting of an antimuon and an electron. The muon is the charged lepton in the second generation of matter in the Standard Model. Since the mass ratio of muon and proton is $m_p/m_\mu \approx 8.9$, the spectrum of muonium is quite similar to hydrogen, except that effects due to proton structure are avoided. The hyperfine splitting in muonium was measured to a part-per-billion level in [99, 100] and calculated with a similar accuracy [101–105]. The *MuSEUM* collaboration plans new precision experiments on the hyperfine structure in muonium [106]. The muon-antimuon bound state is called true muonium [107], or dimuonium. It has yet to be observed, which is the aim of the $\mu\mu$tron collider, which is constructed at the Budker Institute of Nuclear Physics [108]. A similar bound state exists in principle also for third-generation matter and a tau-antitau bound state is called true tauonium. However, due to the extremely short life time of a tau lepton, it is even more difficult to observe [107].

The muon can also form bound states with atomic nuclei. These exotic atoms are commonly referred to as muonic atoms. In this case, the nuclear structure effects are very important for the following reason: The muon is about 207 times heavier than the electron. Therefore, the Bohr radius of muonic atoms, which is an estimate for the distance between bound particle and nucleus, is also 207 times smaller. As a consequence, especially for high Z, the bound muon has a big overlap with the nucleus and it comes to interesting interplays between atomic and nuclear physics. X-rays from muonic atoms were reported for the first time in Ref. [109] in cosmic ray studies and in Ref. [110] with a laboratory muon beam. The beginning of muonic atoms theory is the seminal paper by Wheeler [111]. Since then, the spectra of muonic atoms have been investigated in numerous experiments, e.g. [112–120]. In particular, absolute RMS charge radii of atomic nuclei can be obtained by analysis of muonic x-ray spectra [121]. An overview over the progress in theoretical calculations can be found in Refs. [122–124]. In the past, the codes `MUON` and `RURP` [125] have been used frequently for the comparison of theoretical predictions and measurements of muonic x-rays.

Muonic hydrogen came to attention recently because laser spectroscopy of a $2p \rightarrow 2s$ transition enabled the extraction of the proton charge radius as $r_p^{(\mu)} = 0.84184(67)$ fm and the result was smaller than CODATA value $0.8768(69)$ fm at the time by five standard deviations [126]. In 2013, a new measurement increased the deviation to seven standard deviations [127]. Measurements on muonic deuterium confirmed these results [128] for the deuterium charge radius and lately, also an experiment with atomic hydrogen measured the small proton radius [129]. Results from elastic electron-proton scattering, which are also used for the CODATA value [130], seem to confirm the large value for the proton radius, but the proton-radius extraction from scattering data is not unambiguous [131]. However, a new result from atomic hydrogen spectroscopy resulted in the large value again [132] and the so-called *proton radius puzzle* is not resolved until now. Together with

anomalies on the magnetic moment of the muon [133], this motivates further investigation of muonic systems.

Content of this thesis

To date, the nuclear deformation correction was calculated with perturbative methods only. This thesis contributes to the theory landscape by investigating the nuclear deformation correction non-perturbatively with numerical methods.

In the high-Z regime, the MuX collaboration has started an experimental campaign on x-ray spectroscopy of heavy muonic atoms, where the measurements are performed at the Paul Scherrer Institut. The aim is to measure muonic x-ray spectra for the heaviest and for the first time also radioactive nuclei, for example $^{226}_{88}$Ra and $^{248}_{96}$Cm. Therefore, the calculation of muonic spectra is necessary in connection with these experiments. This thesis presents calculations of muonic spectra, using up-to-date numerical schemes and new methods for predicting the higher order hyperfine structure, including vacuum polarization corrections due to deformed nuclei.

Structure of the thesis

This thesis is organized in the following way:
Chapter 1 gives an introduction to the framework of bound state QED. The usage of the Dirac equation is discussed, together with analytical and numerical solutions for nuclear potentials and vacuum polarization potentials.
In Chapter 2, the nuclear finite size and deformation correction to the bound electron g factor is introduced. A numerical methods for its precise calculation is introduced and compared with the previous results.
Chapter 3 is about the energy levels and transition probabilities of muonic atoms. In this connection, new methods and calculations for vacuum polarization and higher-order hyperfine splitting are presented as well as an updated numerical spectrum generator for the extraction of nuclear parameters. In connection with measurements on isotopically pure muonic Rhenium, the nuclear spectroscopic quadrupole moment is extracted.
Finally, the main findings of the thesis are summarized in the Summary & Outlook.

Chapter 1

Bound state quantum electrodynamics in the Furry picture

In this thesis, relativistic atomic structure calculations are performed in order to investigate nuclear effects on the energy levels of electrons or muons bound in the potential of an atomic nucleus. In this chapter, as an introduction, the starting point is the Lagrangian of quantum electrodynamics (QED), and results will be derived from thereon. This includes the derivation of the Dirac equation for a classical field as the zero-order solution and radiative corrections due to virtual particles. The leading order Vacuum polarization corrections, and their inclusion as potentials in the Dirac equation, are discussed. Finally, the analytical solution of the Dirac equation for the relativistic Coulomb problem is discussed, as well as numerical solutions for arbitrary nuclear potentials.

1.1 The external field approximation

A huge success of the Dirac equation [40] was the correct prediction of the fine structure of the hydrogen atom. Originally intended to be a relativistic generalization of the Schrödinger equation, it was a one-particle equation for a classical field. However, a relativistic quantum theory always has to be a many-body theory, since for high energies effects like pair creation have to be considered. The relativistic quantum field theory suitable for describing the electromagnetic interaction is QED. In this framework, the bound state energies of atomic systems can be obtained including radiative corrections due to the quantized photon field and virtual particle-antiparticle pairs.

In this thesis, hydrogen-like systems and heavy nuclei are considered, so a single fermion (electron or muon) bound to a nucleus with a high charge number Z. The interaction strength of electron and nucleus is characterized by the parameter $Z\alpha$, where $\alpha \approx 1/137$ is the fine-structure constant. For high Z, this parameter is not small and as a result the Coulomb interaction between fermion and nucleus cannot be treated in perturbation theory effectively. For heavy nuclei, the fermion-nucleus mass ratio m_f/M is small. Accordingly, the external field approximation [134, Section 13.6] $m_f/M \to 0$ can be used, which is also called the Furry picture of QED [135]. Here, recoil effects are neglected and the nucleus is considered as the source of a classical electromagnetic field, which the bound fermion is exposed to.

The starting point of the derivations in this chapter is the QED Lagrangian

$$\mathcal{L}_{\text{QED}} := \mathcal{L}_{\text{free}}^{\text{D}} \qquad\qquad + \mathcal{L}_{\text{free}}^{\text{E.M.}} \qquad + \mathcal{L}_{\text{int}} \qquad\qquad (1.1)$$

$$:= \bar{\psi}\left(i\gamma^\mu\partial_\mu - m_f\right)\psi - \frac{1}{4}F_{\mu\nu}F^{\mu\nu} - e\bar{\psi}\gamma^\mu\psi A_\mu,$$

which is the sum of free Dirac, free electromagnetic and interaction Lagrangian. Here, $\psi(x)$ is the fermion field operator, $F_{\mu\nu} = \partial_\mu A_\nu - \partial_\nu A_\mu$ the field strength tensor of the electromagnetic four-potential $A_\mu(x)$. Detailed introductions to QED starting from this Lagrangian can be found in several excellent textbooks, e.g. [134, 136, 137], thus the focus of this section is on the external field approximation and extraction of bound state energies. The counter terms are not included, so the derivations here should be understood on a formal level, for calculations including the counterterms and renormalization, see e.g. [134, Section 14], [138].

In the external field approximation, the electromagnetic four-potential is written as

$$A_\mu(x) = \mathcal{A}_\mu(x) + \hat{A}_\mu(x),$$

where $\mathcal{A}_\mu(x)$ is the classical four-potential, caused by the nuclear charge and current distribution and $\hat{A}_\mu(x)$ is the quantized field describing quantum fluctuations. Correspondingly, the interaction part in Eq. (1.1) is devided as

$$\mathcal{L}_{\text{int}} = -e\bar{\psi}\gamma^\mu\psi\mathcal{A}_\mu - e\bar{\psi}\gamma^\mu\psi\hat{A}_\mu =: \mathcal{L}_{\text{int}}^{\text{C}} + \mathcal{L}_{\text{int}}^{\text{Q}}. \qquad (1.2)$$

For hydrogen-like systems, bound state energies can be extracted from the poles of the fermion propagator. In the following, it will be demonstrated how the poles of the propagator in the interacting theory can be obtained approximately by perturbation theory in powers of the fine structure constant α, including the interaction with the classical field to all orders. For this, the full propagator is connected to the propagator in the external classical field and to the propagator of the free theory.

Propagator in the free Dirac theory

As a start, the Lagrangian of the free Dirac theory $\mathcal{L}_{\text{free}}^{\text{D}}$ from Eq. (1.1) is considered. The Euler-Lagrange equations result in the Dirac equation as the equation of motion for the quantum field as

$$\left(i\gamma^\mu\partial_\mu - m_f\right)\psi(x) = 0. \qquad (1.3)$$

The solution of Eq. (1.3) is written as a superposition of plane-wave solutions [137, Section 3.3.] as

$$\psi(x) = \int \frac{d^3p}{(2\pi)^3} \frac{1}{\sqrt{2E_{\mathbf{p}}}} \sum_{s=1}^{2} \left(a_{\mathbf{p}}^s u^{(s)}(p)\mathrm{e}^{-ip\cdot x} + b_{\mathbf{p}}^{s\dagger} v^{(s)}(p)\mathrm{e}^{ip\cdot x}\right),$$

$$\bar{\psi}(x) = \int \frac{d^3p}{(2\pi)^3} \frac{1}{\sqrt{2E_{\mathbf{p}}}} \sum_{s=1}^{2} \left(b_{\mathbf{p}}^s \bar{v}^{(s)}(p)\mathrm{e}^{-ip\cdot x} + a_{\mathbf{p}}^{s\dagger} \bar{u}^{(s)}(p)\mathrm{e}^{ip\cdot x}\right),$$

where the plane wave solutions read as

$$u^{(1)}(p) = \begin{pmatrix} \sqrt{p \cdot \sigma}\xi_1 \\ \sqrt{p \cdot \bar{\sigma}}\xi_1 \end{pmatrix}, \quad u^{(2)}(p) = \begin{pmatrix} \sqrt{p \cdot \sigma}\xi_2 \\ \sqrt{p \cdot \bar{\sigma}}\xi_2 \end{pmatrix}, v^{(1)}(p) = \begin{pmatrix} \sqrt{p \cdot \sigma}\xi_1 \\ -\sqrt{p \cdot \bar{\sigma}}\xi_1 \end{pmatrix}, v^{(2)}(p) = \begin{pmatrix} \sqrt{p \cdot \sigma}\xi_2 \\ -\sqrt{p \cdot \bar{\sigma}}\xi_2 \end{pmatrix}$$

with

$$\xi_1 = \begin{pmatrix} 1 \\ 0 \end{pmatrix}, \quad \xi_2 = \begin{pmatrix} 0 \\ 1 \end{pmatrix}.$$

The Operators $a_{\mathbf{p}}^s$, $b_{\mathbf{p}}^s$ fulfill the anticommutation relations

$$\left\{a_{\mathbf{p}}^r, a_{\mathbf{q}}^{s\,\dagger}\right\} = \left\{b_{\mathbf{p}}^r, b_{\mathbf{q}}^{s\,\dagger}\right\} = (2\pi)^3 \delta(\mathbf{p} - \mathbf{q})\delta_{rs},$$

and zero for other combinations. The vacuum state of the theory is defined as the state destroyed by the annihilation operators as

$$a_{\mathbf{p}}^s |0\rangle = b_{\mathbf{p}}^s |0\rangle = 0,$$

while the one-particle fermion and anti-fermion states are created from the vacuum as

$$|\mathbf{p}, s\rangle = \sqrt{2E_{\mathbf{p}}}a^{s\,\dagger}|0\rangle,$$
$$|\mathbf{q}, r\rangle = \sqrt{2E_{\mathbf{q}}}b^{r\,\dagger}|0\rangle.$$

Now, the Feynman propagator can be defined as the vacuum expectation value of the time-ordered product [137, Section 3.5.] and reads as

$$S_F(x - y) := \langle 0| T\psi(x)\bar{\psi}(x) |0\rangle = \int \frac{\mathrm{d}^4 p}{(2\pi)^4} \frac{(\gamma^\mu p_\mu + m_f)}{p^2 - m_f^2 + i\epsilon} \mathrm{e}^{-ip\cdot(x-y)}. \tag{1.4}$$

The Feynman propagator is a Green's function of the Dirac equation (1.3), thus

$$(i\gamma^\mu \partial_\mu - m_f) S_F(x - y) = \delta(x - y) \tag{1.5}$$

Propagator in the external field

As a next step, we will consider the sum $\mathcal{L}_{\text{free}}^{\text{D}} + \mathcal{L}_{\text{int}}^{\text{C}}$ of free Dirac Lagrangian and the interaction with the classical external field from Eq. (1.2). In the following, it is assumed that the external field is independent of time. The equations of motion for the fermion field are

$$(i\gamma^\mu \partial_\mu - m_f - e\gamma^\mu \mathcal{A}_\mu) \psi(x) = 0,$$

which simply is the Dirac equation in an external field. However, this is still an equation for the quantum field. The corresponding equation for the classical Dirac field is obtained by using a complete set of states $|n\rangle$ with energies E_n, where $|0\rangle$ is the vacuum state, and define the Dirac wave functions as matrix elements of the fermion field

operator [134, Section 14.1] as

$$
\begin{aligned}
u_n(x) &= u_n(\mathbf{x})\,\mathrm{e}^{-iE_n t} := \langle 0|\,\psi(x)\,|n\rangle \\
v_n(x) &= v_n(\mathbf{x})\,\mathrm{e}^{+iE_n t} := \langle n|\,\psi(x)\,|0\rangle\,,
\end{aligned}
\tag{1.6}
$$

where the first equality follows from time translation invariance, and is only valid in static background fields. Then, it can be shown from the anti-commutation relations of the field operator that the wave functions fulfill the completeness relation

$$
\sum_n u_n(\mathbf{x})u_n^\dagger(\mathbf{y}) + \sum_m v_m(\mathbf{x})v_m^\dagger(\mathbf{y}) = \delta(\mathbf{x} - \mathbf{y}),
$$

and that both $u_n(\mathbf{x})$ and $v_n(\mathbf{x})$ satisfy the Dirac equation, now for classical fields:

$$
\begin{aligned}
\left(i\boldsymbol{\alpha}\cdot\nabla + \beta m_f + e\,\mathcal{A}^0 - e\,\boldsymbol{\alpha}\cdot\boldsymbol{\mathcal{A}}\right)u_n(\mathbf{x}) &= E_n u_n(\mathbf{x}) \\
\left(i\boldsymbol{\alpha}\cdot\nabla + \beta m_f + e\,\mathcal{A}^0 - e\,\boldsymbol{\alpha}\cdot\boldsymbol{\mathcal{A}}\right)v_n(\mathbf{x}) &= -E_n v_n(\mathbf{x})
\end{aligned}
\tag{1.7}
$$

The propagator in the external field is defined, similar to Eq. (1.4), as the vacuum expectation value of time-ordered product

$$
S_{\mathcal{A}}(x,y) := \langle 0_{\mathcal{A}}|\,T\psi(x)\bar{\psi}(x)\,|0_{\mathcal{A}}\rangle\,,
\tag{1.8}
$$

where $|0_{\mathcal{A}}\rangle$ denotes the vacuum state in the external field. It is a Green's function of the equation of motion of the fermion field operator, analogously to Eq. (1.5):

$$
(i\gamma^\mu\partial_\mu - m_f - e\gamma^\mu A_\mu)\,S_{\mathcal{A}}(x,y) = \delta(x - y).
\tag{1.9}
$$

Since the external field violates translation invariance, the propagator in the external field no depends on x and y separately, and not only on the difference $(x - y)$. Radiative corrections in the Furry picture can be calculated by using the usual Feynman rules and the dressed propagator instead of the free propagator as well as solutions of the Dirac equation including the external field for the in and out states. Combining Eq. (1.5) with Eq. (1.9) gives a relation between the propagators of the free theory and in the external field [136, Section 2.5.], which can be solved iteratively, as

$$
\begin{aligned}
S_{\mathcal{A}}(x,y) ={}& S_F(x-y) + \int \mathrm{d}x\, S_F(x-z)\,(-e\gamma^\mu A_\mu(z))\,S_{\mathcal{A}}(z,y) \\
={}& S_F(x-y) + \int \mathrm{d}z\, S_F(x-z)(-e\gamma^\mu A_\mu(z))\,S_F(z-y) \\
& + \iint \mathrm{d}z_1\mathrm{d}z_2\, S_F(x-z_1)(-e\gamma^\mu A_\mu(z_1))\,S_F(z_1-z_2)(-e\gamma^\mu A_\mu(z_2))\,S_F(z_2-y) \\
& + \dots\,.
\end{aligned}
\tag{1.10}
$$

As demonstrated in Fig. 1.1, this gives an intuitive picture of the dressed propagator: Propagation in the external field corresponds to free propagation with all possible inter-
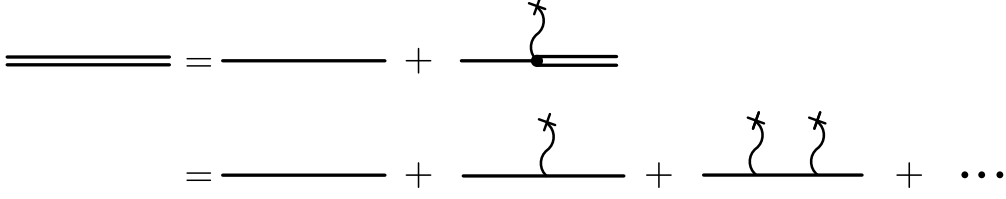
Figure 1.1: Relation between the propagator including the external field and the propagator of the free theory in Feynman diagrams corresponding to Eq. (1.10). A double line corresponds to the dressed propagator in the external field, a single line to the free Dirac propagator, and a wave line with a cross to the interaction with the external field. The propagator in the external field is obtained by including all interactions with the external field in the free propagator.

actions with the external field included. Another useful form of the propagator in the external field is the spectral representation in terms of the Dirac wave functions (1.6). By inserting a complete set of states in Eq. (1.8), one obtains

$$S_{\mathcal{A}}(x,y) = \Theta(x^0 - y^0) \sum_n u_n(x)\bar{u}_n(y) - \Theta(y^0 - x^0) \sum_m v_m(x)\bar{v}_m(y).$$

For a time-independent external field, a Fourier transformation in the zeroth component yields

$$\tilde{S}(\mathbf{x}, \mathbf{y}, E) = \sum_n \frac{u_n(\mathbf{x})\bar{u}_n(\mathbf{y})}{E_n - E - i\,\epsilon} + \sum_m \frac{v_m(\mathbf{x})\bar{v}_m(\mathbf{y})}{E_m + E - i\,\epsilon}. \tag{1.11}$$

Therefore, bound states due to the external field lead to additional isolated poles in the propagator.

Propagator of interacting theory

Finally, we will consider the propagator in the interacting theory, including the interaction with the quantized photon field. A similar argument as in the derivation of Eq. (1.11) also holds for the interacting theory [134, Section 14.2.]. This is, bound state energies including all radiative corrections appear as isolated poles of the full propagator. In order to locate the positions of these poles, perturbation theory with the propagator including the external field is used, expanding the propagator in powers of the fine-structure constant α. The zero-order term is the dressed propagator in the background field, corresponding to solving the Dirac equation with the background field. The diagrams contributing to the radiative corrections to first order in α are the vacuum-polarization (VP) and self-energy (SE) diagrams shown in Fig. 1.2 (*a*) and (*b*), respectively. Using the Feynman rules [136, Section 6.1.], the propagator of the interacting theory $S_I(x,y)$ is expanded
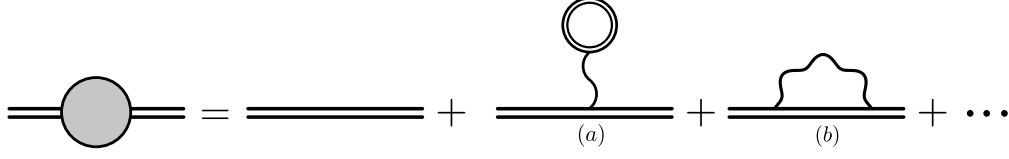
Figure 1.2: Perturbative expansion of the propagator of the interacting theory in powers of the fine-structure constant α. The zero-order contribution is the propagator in the external field. To first order in α, the contributions are the vacuum-polarization diagramm (a) and the self-energy diagram (b).

to first order in α as

$$S_I(x, y) \approx S_\mathcal{A}(x, y) + \int \mathrm{d}^4 z_1 \, \mathrm{d}^4 z_2 \, S_\mathcal{A}(x, z_1) \left[\Sigma_{\mathrm{VP}}(z_1, z_2) + \Sigma_{\mathrm{SE}}(z_1, z_2) \right] S_\mathcal{A}(z_2, y),$$

with

$$\Sigma_{\mathrm{VP}}(z_1, z_2) := -\delta(z_1 - z_2)(-ie\gamma^\mu) \int \mathrm{d}z \, S_P(z_1 - z) \mathrm{Tr}[(-ie\gamma_\mu) S_\mathcal{A}(z, z)],$$

$$\Sigma_{\mathrm{SE}}(z_1, z_2) := (-ie\gamma^\mu) S_\mathcal{A}(z_1, z_2) S_P(z_1 - z_2)(-ie\gamma_\mu),$$

where $g_{\mu\nu} S_P(x - y)$ is the photon propagator in position space (Appendix A). Using the Fourier transformed functions

$$\Sigma_{\mathrm{VP/SE}}(\mathbf{z}_1, \mathbf{z}_2, E) = \int \mathrm{d}z_1^0 \, \mathrm{e}^{iE(z_1^0 - z_2^0)} \Sigma_{\mathrm{VP/SE}}(z_1, z_2),$$

and the spectral representation of the propagator from Eq. (1.11), the levelshifts of the n-th level can be extracted from the shift of the poles [134, Section 14.2.] as

$$\Delta E_n = \int \mathrm{d}^3 \mathbf{x} \, \mathrm{d}^3 \mathbf{y} \, \bar{u}_n(\mathbf{x}) \left(-\Sigma_{\mathrm{VP}}(\mathbf{x}, \mathbf{y}, E_n) - \Sigma_{\mathrm{SE}}(\mathbf{x}, \mathbf{y}, E_n) \right) u_N(\mathbf{y}).$$

1.1.1 Vacuum polarization potentials

For practical calculations of the vacuum polarization of order α, the closed fermion loop in Fig. 1.2 b) can be expanded in numbers of interactions with the background field, using Eq. 1.10. For the case of atomic physics, since the nuclear potential is proportional to the nuclear charge number Z, this expansion is in powers of $Z\alpha$. The corresponding diagrams in order $\alpha(Z\alpha)$ (Uehling potential [139]) and $\alpha(Z\alpha)^3$ (Wichmann-Kroll potential [140]) are shown in Fig. 1.3. Since the closed loop now is formed by the free fermion propagator, all diagramms of order $\alpha(Z\alpha)^n$ with even n vanish as a consequence of Furry's theorem [137, Section 10.1.]. Formally, the order $\alpha(Z\alpha)$ correction δS_{Uehl}

from diagram (a) in Fig. 1.4 to the propagator $S_{\mathcal{A}}$ reads

$$\delta S_{\text{Uehl}}(x, y) = \int \mathrm{d}z_1 \, S_{\mathcal{A}}(x, z_1) \Sigma_{\text{Uehl}}(z_1) S_{\mathcal{A}}(z_1, y) \tag{1.12}$$

with

$$\begin{aligned} \Sigma_{\text{Uehl}}(z_1) \quad &:= - \int \mathrm{d}z_2 (-ie\gamma^\mu) S_P(z_1 - z_2) \\ &\times \int \mathrm{d}z_3 \operatorname{Tr}\left[(-ie\gamma_\mu) S_F(z_2 - z_3)(-e\gamma^\nu A_\nu(z_3)) S_F(z_3 - z_2) \right]. \end{aligned}$$

Analogously to the inclusion of the external field in the propagator from Eq. (1.9), Eq. (1.12) and the corresponding iterations from diagrams (b), (c), ... in Fig. 1.4 can be summed to define a propagator $S_{\mathcal{A}+\text{Uehl}}$ which contains all iterations both in the external field and the order $\alpha(Z\alpha)$ vacuum polarization via the integral equation

$$S_{\mathcal{A}+\text{Uehl}}(x, y) = S_{\mathcal{A}}(x, y) + \int \mathrm{d}z_1 \, S_{\mathcal{A}}(x, z_1) \Sigma_{\text{Uehl}}(z_1) S_{\mathcal{A}+\text{Uehl}}(z_1, y). \tag{1.13}$$

This propagator is a Green's function for the Dirac equation including the external field and the Uehling potential as

$$\left(i\gamma^\mu \partial_\mu - m_f - e\gamma^\mu A_\mu + \Sigma_{\text{Uehl}} \right) S_{\mathcal{A}+\text{Uehl}}(x, y) = \delta(x - y).$$

As a result, the diagrams in Fig. 1.4 can be teated by solving the Dirac equation (1.7) including the Uehling potential. The same reasoning holds as well for the Wichmann-Kroll potential (Fig. 1.3 b)) and for the order $\alpha^2(Z\alpha)$ vacuum polarization, referred to as the Källen-Sabry potential [141], where the corresponding diagrams are shown in Fig. 1.5.

Since the formal expressions for the vacuum polarization potentials contain divergences, they have to be renormalised. This Section concludes with giving the corresponding expressions for the renormalized Uehling (order $\alpha(Z\alpha)$) and Källen-Sabry (order $\alpha^2(Z\alpha)$) potentials for a virtual electron-positron pair and an extended, spherically symmetric nuclear charge distribution $\rho(r)$, which can be included in the Dirac equation. It is important to note, that the virtual particle in the loop can be a different one compared to the considered fermion. Therefore, the mass of the virtual particle is m_l, which is an additional dependency of the potential. For an electron-positron loop, correspondingly $m_l = m_e$ and for a muon-antimuon loop $m_l = m_\mu$. For example, the electronic vacuum polarization is muonic atoms is more impartent than the muonic vacuum polarization. The Uehling potential reads as [142, 143]

$$\begin{aligned} V_{\text{Uehl}}^{(m_l)}(r) = -\alpha \frac{2\alpha}{3\pi} \int_0^\infty \mathrm{d}r' \, 4\pi\rho(r') \int_1^\infty \mathrm{d}t \left(1 + \frac{1}{2t^2} \right) \\ \times \frac{\sqrt{t^2 - 1}}{t^2} \frac{\exp(-2m_l|r - r'|t) - \exp(-2m_l(r + r')t)}{4m_l rt}, \end{aligned} \tag{1.14}$$

and the Källen-Sabry potential, corresponding to the diagrams in Fig. 1.5, is derived
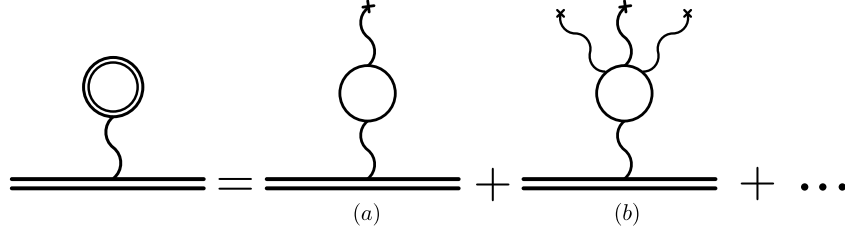
Figure 1.3: Expansion of the order α vacuum polarization in powers of $(Z\alpha)$, i.e. in number of interactions with the nuclear field. The contributions with odd powers vanish due to Furry's theorem. The $\alpha(Z\alpha)$ contribution (diagram a) is the Uehling term, the $\alpha(Z\alpha)^3$ contribution (diagram b) is the Wichmann-Kroll term.
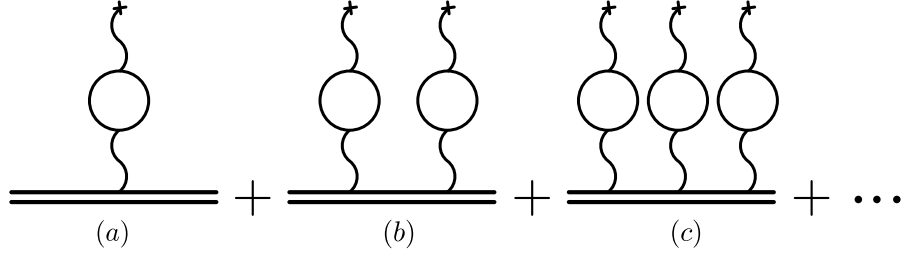
Figure 1.4: Resummation of iterations of the Uehling potential needed for the modified Propagator from Eq. (1.13).

in [144–147] and given e.g. in [142, 148] as

$$V_{\text{KS}}^{(m_l)}(r) = \frac{\alpha^2(Z\alpha)}{\pi r} \int_0^\infty dr' \, r' \rho(r') \left(L_0(2m_l|r - r'|) - L_0(2m_l(r + r'))\right), \quad (1.15)$$

with

$$L_0(x) = -\int^x dy \, L_1(y),$$

$$L_1(x) = \int_1^\infty dt \, e^{-rt} \left\{ \left(\frac{2}{3t^5} - \frac{8}{3t} \right) f(t) + \left(\frac{2}{3t^4} + \frac{4}{3t^2} \right) \sqrt{t^2 - 1} \ln[8t(t^2 - 1)] \right.$$

$$\left. + \left(\frac{2}{9t^2} + \frac{7}{108t^4} + \frac{13}{54t^2} \right) \sqrt{t^2 - 1} + \ln(\sqrt{t^2 - 1} + t) \left(\frac{2}{9t^7} + \frac{5}{4t^5} + \frac{2}{3t^3} - \frac{44}{9t} \right) \right\},$$

$$f(t) = \int_t^\infty dx \left[\frac{(3x^2 - 1)\ln(\sqrt{x^2 - 1} + x)}{x(x^2 - 1)} - \frac{\ln(8x(x^2 - 1))}{\sqrt{x^2 - 1}} \right].$$
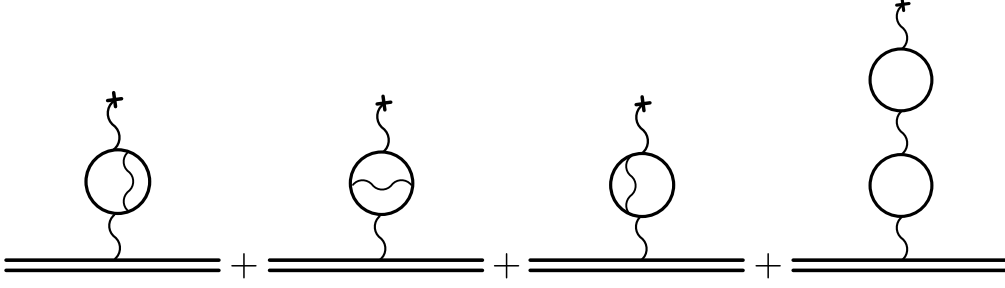
Figure 1.5: Feynman diagrams corresponding contribution to the Källen-Sabry potential of order $\alpha^2(Z\alpha)$, as given in Eq. (1.15).

1.2 Dirac equation in central potentials

In the previous Section, the binding energies of a fermion bound by an atomic nucleus were analyzed in the framework of the Furry picture of QED. The zeroth order approximations were shown to be the eigenenergies of the solutions of the Dirac equation (for a $\mathbb{C}$-number field) including the nuclear background field. Furthermore, it was demonstrated that certain radiative corrections can be included as potentials in the Dirac equation as well. To a first approximation, the nuclear potential can be described by a static electric field which possesses spherical symmetry, and deviations thereof may be treated by perturbation theory later on. Thus, in this Section, the solutions of the Dirac equation for a spherical symmetric potential are discussed, mainly following [42, 134]. Then, the case of the pure Coulomb potential is discussed, where the solution can be given in closed form due to the high degree of symmetry. Finally, the dual-kinetic-balance method [149] for obtaining numerical solutions for arbitrary spherical symmetric potentials is discussed.

Firstly, the Dirac equation (1.7) for the functions v_n is rewritten, such that it has the same form as for u_n. For this, add a new range of indices $\tilde{n}$ to the original n and define $u_{\tilde{n}}(x) \coloneqq v_n(x)$, $E_{\tilde{n}} \coloneqq -E_n$. Secondly, static electric background fields are considered, which corresponds to a four potential

$$\mathcal{A}_\mu(x) = (\Phi(\mathbf{x})/e, \mathbf{0}),$$

where the electric potential $\Phi(\mathbf{r})$ can be expressed in terms of a spherically symmetric nuclear charge distribution $\rho(|\mathbf{r}|)$ as

$$\Phi(\mathbf{r}) = -Z\alpha \int \mathrm{d}V' \, \frac{\rho(|\mathbf{r}'|)}{|\mathbf{r} - \mathbf{r}'|}, \tag{1.16}$$

where $\int \mathrm{d}V \, \rho(|\mathbf{r}|) = 1$. Since Φ only depends on $|\mathbf{r}|$, we define

$$V(r) \coloneqq \Phi((r, 0, 0))$$

for spherical coordinates $\mathbf{r} = (r, \vartheta, \varphi)$. Thereby, the Dirac equation (1.7) reads as

$$\mathrm{H}_D\, u_n(\mathbf{r}) \coloneqq (i\boldsymbol{\alpha} \cdot \nabla + \beta m_f + V(r))\, u_n(\mathbf{r}) = E_n u_n(\mathbf{r}), \qquad (1.17)$$

where the eigenenergies E_n are both positive and negative and the spectrum contains both continuum and discrete parts. $u_n(\mathbf{r})$ are the corresponding solutions in form of four-component spinors. For an arbitrary potential $V(r)$ possessing spherical symmetry, the solution can be simplified significantly by transforming the partial differential equation (1.17) into an ordinary differential equation.

For the Dirac Hamiltonian with spherically symmetry, energy eigenfunctions can be found, which also have a well-defined parity and total angular momentum. At first, the relativistic angular quantum number κ is introduced as a function of the orbital angular momentum quantum number l and total angular momentum quantum number j as

$$\kappa(j, l) \coloneqq (-1)^{j+l+1/2}\left(j + \frac{1}{2}\right).$$

Since for a Dirac particle every value of l has two possible values $j = l \pm 1/2$, the mapping $\kappa \leftrightarrow (j, l)$ is bijective with $j(\kappa) = |\kappa| - 1/2$; $l(\kappa) = |\kappa| + (\mathrm{sgn}(\kappa) - 1)/2$. Eigenfunctions of the total angular momentum can be constructed by the eigenfunctions of the orbital angular momentum and spin operator, the spherical harmonics $\mathrm{Y}_{lm}(\vartheta, \varphi)$ and two-component spinors $\chi_{1/2} = (1, 0)^T$; $\chi_{-1/2} = (0, 1)^T$, respectively as

$$\Omega_{\kappa m}(\vartheta, \varphi) \coloneqq \sum_{m_l = -l(\kappa)}^{l(\kappa)} \sum_{m_s = -1/2}^{1/2} \mathrm{C}_{l(\kappa)m_l\, 1/2\, m_s}^{j(\kappa)m}\, \mathrm{Y}_{l(\kappa)m_l}(\vartheta, \varphi)\chi_{m_s}, \qquad (1.18)$$

where $\mathrm{C}_{l_2 m_2\, l_3 m_3}^{l_1 m_1}$ are the Clebsch-Gordan coefficients [150]. The functions defined in Eq. (1.18) are called *spherical spinors*. Direct calculations shows that a pair $(\Omega_{\kappa m}, \Omega_{-\kappa m})$ have the same values for j, but opposite parity. Motivated by the solutions of the free Dirac equation, the solution is written with an ansatz in two component spinors, with a priori different values for κ_1, κ_2, m_1, m_2. However, for a well defined total angular momentum and z-component of the total angular momentum $|\kappa_1| = |\kappa_2|$ and $m_1 = m_2$ is needed. Furthermore, applying the parity operator reveals that the lower component needs to have the opposite parity compared to the upper component in order for the four-component spinor having a well-defined parity, which corresponds to the parity of the upper component, and therefore $\kappa_1 = -\kappa_2$. As a result, the solutions are written as

$$u_{n\kappa m_j}(\mathbf{r}) = \begin{pmatrix} g_{n\kappa}(r)\Omega_{\kappa m_j}(\vartheta, \varphi) \\ if_{n\kappa}(r)\Omega_{-\kappa m_j}(\vartheta, \varphi) \end{pmatrix}. \qquad (1.19)$$

Using this ansatz in Eq. (1.17) leads to the following system of equations for the radial

functions $g_{n\kappa}(r)$ and $f_{n\kappa}(r)$:

$$\frac{\mathrm{d}g(r)}{\mathrm{d}r} + (1+\kappa)\frac{g(r)}{r} - [E + m_f - V(r)]\,f(r) = 0$$

$$\frac{\mathrm{d}f(r)}{\mathrm{d}r} + (1-\kappa)\frac{f(r)}{r} + [E - m_f - V(r)]\,g(r) = 0. \tag{1.20}$$

1.2.1 Bound state solutions of the Coulomb problem

For a point-like nucleus with charge number Z, the pure Coulomb potential reads

$$V_C(r) = -\frac{Z\alpha}{r}, \tag{1.21}$$

and the radial equations (1.20) can be solved analytically in this case. As a first step, the radial wave functions are substituted with

$$g_{n\kappa}(r) = \sqrt{1 + E_{n\kappa}}\,\mathrm{e}^{-\lambda r}(\varphi_1(r) + \varphi_2(r))$$
$$f_{n\kappa}(r) = \sqrt{1 - E_{n\kappa}}\,\mathrm{e}^{-\lambda r}(\varphi_1(r) - \varphi_2(r)),$$

and for the functions $\varphi_i(r)$ the power-series ansatz

$$\varphi_i(r) = (2\lambda r)^\gamma \sum_{k=0}^{\infty} a_k^{(i)}(2\lambda r)^k,$$

is assumed, where $\lambda = \sqrt{1 - E_{n\kappa}^2}$ and $\gamma = \pm\sqrt{\kappa^2 - (Z\alpha)^2}$. Plugging this ansatz into Eq. (1.20) results in recurrence relations, such that the solution can be expressed only in terms of the normalization coefficient $a_0^{(1)}$ as

$$\varphi_1(r) = a_0^{(1)}(2\lambda r)^\gamma\, \mathrm{F}(1 - n_r, 2\gamma + 1, 2\lambda r)$$
$$\varphi_2(r) = a_0^{(1)}(\kappa - Z\alpha/\lambda)(2\lambda r)^\gamma\, \mathrm{F}(-n_r, 2\gamma + 1, x)/n_r,$$

where $n_r = Z\alpha E_{n\kappa}/\lambda - \gamma$ and $\mathrm{F}(a, b, c)$ are the hypergeometric function, as defined in Eq. (B.3). Now, for the positive value of γ, the solutions are regular at the origin, but behave as $\mathrm{e}^{\lambda r}$ as $r \to \infty$. On the other hand, linear combination of positive and negative values of γ enable solutions which are regular at infinity but are divergent at the origin. Solutions regular both at the origin and at infinity can only be obtained for certain energies, corresponding to integer values of n_r [151]. Therefore, with $n = n_r + |\kappa|$, the bound state energies read

$$E_{n\kappa} = \frac{(m_f c^2)}{\sqrt{1 + \dfrac{(Z\alpha)^2}{\left(n - |\kappa| + \sqrt{|\kappa|^2 - (Z\alpha)^2}\right)^2}}}, \tag{1.22}$$

for $n \in \{1, 2, 3, ...\}$ and $\kappa \in \{-n, ..., -1, 1, ..., n-1\}$. These solution explains the spectrum of hydrogen-like atoms to a reasonable accuracy, including fine structure splitting, as long as $Z\alpha \ll 1$. The solutions are degenerate in the sign of κ, i.e. states with the same j but different l have the same energy. As a result, the $2s^1/2$ and $2p^1/2$ states are degenerate. The lifting of this degeneracy (Lamb shift) is explained by radiative corrections and finite nuclear size effects. However, in situations where $Z\alpha$ is not much smaller than unity, the point-like approximation becomes increasingly worse and solutions of the Dirac equation for non-Coulomb, extended potentials have to be used.

1.2.2 Numerical solution in a cavity for arbitrary potentials

Except the rare cases, where the radial equations (1.20) can be solved exactly (eg. Coulomb potential, spherical potential well), numerical methods have to be used to obtain solutions for $g(r)$ and $f(r)$. Especially for atomic systems with large finite nuclear size effects, like highly charged, heavy ions and muonic atoms, the nuclear potential deviates from the Coulomb potential significantly and numerical solutions have to be found, including the extended nuclear charge distribution.

Generally, for finite basis set solutions of the Dirac equation, the radial equations (1.20) are considered, but the domain is changed from $r \in [0, \infty)$ to a finite cavity $r \in [0, R]$. On the original domain, the spectrum of the energy eigenvalues E has a negative continuum $E \in (-\infty, -m_f]$, a positive continuum $E \in [m_f, \infty)$, and a discrete part $E \in (-m_f, m_f)$ of infinitely many bound states, where m is the mass of the bound fermion. On the modified domain, the positive and negative continuum become discrete [152], but still infinite. A problem with numerical solutions of the Dirac equation is the appearance of unphysical, or spurious states [152, 153]. A method circumventing this problem was presented in [149], which is shortly described in the following.

The radial equations (1.20) can be rewritten in matrix form as

$$\begin{pmatrix} m_f + V(r) & (-\partial_r + \kappa/r) \\ (\partial_r + \kappa/r) & -m_f + V(r) \end{pmatrix} \nu(r) =: \mathrm{H}_\kappa \nu(r) = E\,\nu(r) \tag{1.23}$$

for the function $\nu(r) = (G(r), F(r))^T = (rg(r), rf(r))^T$. As a finite set of basis functions, B-splines $\Pi_{i,k}(r)$ of order k with a suitable knot sequence as described in [152] are selected, where the first and last spline is set to zero. With the size of the basis set n, the solutions are expressed with $2n$ coefficients c_i as

$$\nu(r) = \sum_{i=1}^{2n} c_i\,\nu_i(r) := \sum_{i=1}^{n} c_i \begin{pmatrix} \Pi_{i,k}(r) \\ (\partial_r + \kappa/r)\Pi_{i,k}(r)/(2m_f). \end{pmatrix} + \sum_{i=n+1}^{2n} c_i \begin{pmatrix} (\partial_r - \kappa/r)\Pi_{i,k}(r)/(2m_f) \\ \Pi_{i,k}(r) \end{pmatrix}. \tag{1.24}$$

Thereby, the infinite amount of discrete states in the cavity are reduced to $2n$ states. The finite basis expansion (1.24) can be plugged into the radial equations (1.23) which results in the generalized eigenvalue problem [149] for the $2n$ coefficients c_j

$$\sum_{j=1}^{2n} \left(\nu_i^T(r)\mathrm{H}_\kappa(r)\nu_j(r) + \nu_j^T(r)\mathrm{H}_\kappa(r)\nu_i(r) \right)/2 \times c_j = E \sum_{j=1}^{2n} (\nu_i(r)^T\nu_j(r)) \times c_j, \tag{1.25}$$

where $i \in [1, ..., 2n]$, which can be solved efficiently with existing libraries for B-splines and linear algebra.

In the case of a positively charged nucleus with $Z\alpha < 1$, the eigenvalues of the solution of (1.25) consist of n negative values, forming a discrete representation of the negative continuous spectrum and of n positive values representing the bound state spectrum and the positive continuous spectrum [153]. Besides the eigenenergies, approximations of the bound and continuum Dirac wave functions are obtained in terms of the coefficients c_i and Eq. (1.24). This enables the numerical evaluation of intermediate sum of states occurring in second order perturbation theory or in the spectral representation of the Dirac propagator.

Chapter 2

Nuclear shape effects on the bound-electron g factor

In this chapter, non-perturbative calculations of the nuclear deformation (ND) correction to the bound electron g factor are presented and the corresponding values for nuclei across the entire nuclear chart are shown, quantifying the non-perturbative corrections in the values of the bound electron g factor. Furthermore, it is shown how the model dependence and therefore uncertainty of the finite nuclear size correction can be reduced using deformed nuclear charge distributions and that in this connection the numerical calculations are necessary for obtaining precise results. A part of the work described in this chapter was previously submitted in Ref. [4].

2.1 Motivation

The electron's g factor characterizes its magnetic moment in terms of its angular momentum. For an electron bound to an atomic nucleus, the g factor can be predicted in the framework of bound state quantum electrodynamics (QED) as well as measured in Penning traps, both with a very high degree of accuracy, e.g. [58, 60]. This enables extraction of information on fundamental interactions, constants and nuclear structure. For example, the combination of theory and precise measurements of the bound electron g factor has recently provided an enhanced value for the electron mass [58], and bound state QED in strong fields was tested with unprecedented precision [57,59,83,154]. It also enables measurement on characteristics of nuclei such as electric charge radii, as shown for Si^{13+} ion [60], or the isotopic mass difference as demonstrated for ^{48}Ca and ^{40}Ca in [155], or, as proposed theoretically, magnetic moments [84]. Also, it was argued that g-factor experiments with heavy ions could result in a independent determination of the fine-structure constant which is more accurate than the presently established one [86]. With planned experiments involving high Z nuclei [65, 156] and current experimental accuracies on the 10^{-10} level for low Z, it is important to keep track also of higher order effects. In this context, besides QED, e.g. [70–72,157,158], and nuclear polarization [76] corrections, also the influence of nuclear size and deformation is critical. In [82], the nuclear shape correction to the bound electron g factor was introduced and calculated for spinless nuclei using the perturbative effective radius method (ERM) [159,160]. This effect takes the influence of a deformed nuclear charge distribution into account, and changes the g factor up to a 10^{-6} level for heavy nuclei, thus being potentially visible in future experiments. Additionally, the uncertainty of the finite nuclear size correction to

the Lamb shift in hydrogenlike ^{238}U was shown to be sensitive on nuclear deformation effects [160]. This motivates the possibility of a lowering of uncertainties for the bound electron g factor by considering ND. Therefore, a comparison of experiment and theory for heavy nuclei demands a further improvement and critical scrutiny of the validity of the previously used perturbative methods, as pointed out in [161].

2.2 Averaged Nuclear Potential

In this section, the electric interaction energy between a spinless atomic nucleus, described by a rigid rotor (Appendix D), and an electron in a hydrogen-like ion is investigated, following [82, 160]. In Chapter 1, it is shown that to leading order, without radiative corrections, the bound state energies can be obtained by solving the Dirac equation for the electron in the nuclear potential. For a rigid rotor, the charge density $\rho(\mathbf{r}'_N)$ is given in the nuclear body fixed frame, and the position of the body fixed frame in the laboratory frame is described in terms of the Euler angles (ϕ, θ, ψ). In the following, primed coordinates refer to the body fixed system and unprimed coordinates to the laboratory system, and vectors are written in spherical coordinates as $\mathbf{r}_i = (r_i, \vartheta_i, \varphi_i)$. The passive picture of rotations is used, i.e. the vectors are considered as invariant geometric objects and the Euler angles are used to describe the rotations of the coordinate axes. The electric potential energy of an electron at position $\mathbf{r}'_e$ due to the nuclear electric field is

$$V(\mathbf{r}'_e) = -Z\alpha \int \mathrm{d}^3\mathbf{r}'_N \frac{\rho(\mathbf{r}'_N)}{|\mathbf{r}'_e - \mathbf{r}'_N|}.$$

Now, the denominator is expanded in spherical multipoles [162] without assumptions about the distance of nuclear charge distribution and electron, which results in radial distribution functions of the l-th multipoles, instead of the usual scaling $\sim 1/r^{l+1}$. Hereby, the potential is rewritten as

$$V(\mathbf{r}'_e) = \sum_{l=0}^{\infty} \sum_{m=-l}^{l} V_{lm}(\mathbf{r}'_e) = \sum_{l=0}^{\infty} \sum_{m=-l}^{l} -Z\alpha \int \mathrm{d}^3\mathbf{r}'_N \frac{r_<^l}{r_>^{l+1}} \rho(\mathbf{r}'_N) C^*_{lm}(\vartheta'_N, \varphi'_N) C_{lm}(\vartheta'_e, \varphi'_e),$$

(2.1)

where $r_> = \max(r'_N, r'_e)$ and $r_< = \min(r'_N, r'_e)$, and $C_{lm}(\vartheta, \varphi) = \sqrt{4\pi/(2l+1)} Y_{lm}(\vartheta, \varphi)$ are the normalized spherical harmonics. Since the laboratory frame and the body fixed frame are related by a rotation, the absolute value of vectors stays the same, i.e. $r'_i = r_i$. Since the angular variables are separated by the multipole expansion, the electronic angles can be transformed to the laboratory system in a simple way, while keeping the nuclear variables in the body-fixed frame. The body-fixed variables ϑ'_e, φ'_e are in general a function of the laboratory ϑ_e, φ_e and the Euler angles (ϕ, θ, ψ). For the special case of spherical harmonics, the connection is

$$C_{l0}(\vartheta'_e, \varphi'_e) = \sum_{\tilde{m}=-l}^{l} C^*_{l\tilde{m}}(\theta, \phi) C_{l\tilde{m}}(\vartheta_e, \varphi_e).$$

Furthermore, nuclear polarization effects [76] are neglected, so it is assumed that the nucleus is in its ground state only and the interaction with the electron does not induce nuclear transitions. These assumption is a valid approximation, since the typical nuclear energy scales are on the order of $100 \, \text{keV}$, which is much larger than typical energies in atomic physics. Under these conditions, the nuclear degrees of freedom can be integrated out via the expectation value of the electric potential with the nuclear ground state wave functions, which correspond in the rigid rotor model to $I = M = K = 0$. Due to the vanishing nuclear spin, only $l = m = \tilde{m} = 0$ terms are non-zero, and the potential (2.1) reduces to

$$
\begin{aligned}
V(r_e) &= -Z\alpha \int \mathrm{d}^3 \mathbf{r}'_N \frac{\rho(\mathbf{r}'_N)}{r_>} \\
&= -\frac{Z\alpha}{r_e} 4\pi \int_0^{r_e} \mathrm{d}r'_N r'^2_N \rho_0(r'_N) - Z\alpha 4\pi \int_{r_e}^\infty \mathrm{d}r'_N r'_N \rho_0(r'_N),
\end{aligned}
\tag{2.2}
$$

with the averaged charge distribution

$$
4\pi \rho_0(r'_N) = \int_0^{2\pi} \mathrm{d}\varphi'_N \int_0^\pi \mathrm{d}\vartheta'_N \sin\theta \, \rho(\mathbf{r}'_N).
$$

Thus, for spinless nuclei, the potential is spherically symmetric, although the charge distribution of the nucleus does not have to be. Therefore, the theory of the bound electron g-factor in a spherical potential can be applied also in this case.

2.3 Bound-electron g factor in central potentials

In the previous Section, it was shown that for spinless nuclei the electric potential for a bound electron is still spherically symmetric, also for deformed nuclear charge distributions. Therefore, in this Section, the theory of the bound-electron g factor in a spherically symmetric potential is presented, following [151, 163]. In a weak magnetic field, the g factor is determined by the energy splitting in a homogeneous magnetic field, which is linear in the field strength. Therefore, an electron moving in an arbitrary central potential $V(r_e)$ of the nucleus and in a homogeneous magnetic field $\mathbf{B}$ is considered. The z axis is aligned along the magnetic field, i.e. $\mathbf{B} = B\mathbf{e}_z$, where $\mathbf{A}(\mathbf{r}) = \mathbf{B} \times \mathbf{r}/2$ is the corresponding vector potential in Coulomb gauge. The stationary Dirac equation for the electron thereby reads as

$$
[\boldsymbol{\alpha} \cdot \mathbf{p} + \beta m_e + V(r) - e\boldsymbol{\alpha} \cdot \mathbf{A}(\mathbf{r})] \, |\psi\rangle = E \, |\psi\rangle .
$$

Since only the energy splitting linear in the magnetic field strength is needed for the g factor in a weak field, it is enough to solve the Dirac equation with only the nuclear potential as

$$
[\boldsymbol{\alpha} \cdot \mathbf{p} + \beta m_e + V(r)] \, |n\kappa m\rangle = E \, |n\kappa m\rangle ,
$$

where the methods presented in Section 1.2 for spherical potentials can be used. Then, the first order energy splitting due to the magnetic field is considered as

$$\Delta E_B = -e \langle n\kappa m | \boldsymbol{\alpha} \cdot \mathbf{A}(\mathbf{r}) | n\kappa m \rangle .$$

Using angular momentum theory, the energy splitting can be calculated as

$$\Delta E_B = m \, g\mu_B B,$$

where the g factor is defined as the proportionality constant between energy shift and product of the quantum number m, Bohr magneton μ_B and field strength B as

$$g = \frac{2m_e\kappa}{j(j+1)} \int_0^\infty \mathrm{d}r r^3 f_{n\kappa}(r) g_{n\kappa}(r). \tag{2.3}$$

It has been shown in [163], that the radial integral in Eq. (2.3) is related to the derivative of the electron energies with respect to its mass. As a first step, a transformation of the radial integral in Eq. (2.3) can be performed. For this, the first line of the radial equations (1.20) is multiplied by $g(r)$ and the second line is multiplied by $f(r)$. Then, the sum of these equation is independent of the energy E and the potential $V(r)$ and by integrating this sum over r, the following identity of radial integrals is obtained:

$$\int \mathrm{d}r r^3 f(r) g(r) = -\frac{1}{4m_e} \Big(1 - 2\kappa \int_0^\infty \mathrm{d}r r^2 (f(r)^2 - g(r)^2) \Big).$$

Now, the radial integral on the right hand side can be expressed in terms of the expectation value of the β matrix, using its definition from Appendix A, as

$$\int_0^\infty \mathrm{d}r r^2 (f(r)^2 - g(r)^2) = \langle n\kappa m | \beta | n\kappa m \rangle$$

Since for potentials which do not depend on the mass of the electron, β can be expressed by the derivative of the Dirac Hamiltonian (1.17) as $\beta = \partial \mathrm{H}_D/\partial m_e$, it follows that

$$\langle n\kappa m | \beta | n\kappa m \rangle = \langle n\kappa m | \partial \mathrm{H}_D/\partial m_e | n\kappa m \rangle = \partial E_{n\kappa}/\partial m_e,$$

and the g factor (2.3) can be written as

$$g = \frac{-\kappa}{j(j+1)} \left(1 - 2\kappa \frac{\partial E_{n\kappa}}{\partial m_e} \right). \tag{2.4}$$

This formula is valid for arbitrary central potentials and can be used for numerical and analytical calculations. Using the expression for the energies in the pure Coulomb potential from Eq. (1.22), the ground state g factor for a point-like nucleus with charge number Z reads as

$$g_{\mathrm{Point}} = \frac{2}{3} \left(1 + 2\sqrt{1 - (Z\alpha)^2} \right), \tag{2.5}$$

a result which can also be obtained by integration of Eq. (2.3) with the known wave functions of the Coulomb problem and was obtained first by Breit [66].

For an extended nuclear charge distribution, the resulting bound-electron g factor is different from the point-like value (2.5). Correspondingly, the finite nuclear size correction is defined as the difference between the g factor of the extended charge distribution (2.4) and the point-like nucleus as

$$\delta g_{\text{FS}} = g - g_{\text{Point}}.$$

2.4 Non-perturbative analysis of nuclear shape effects

In this work, we focus on quadrupole deformations and beyond, since atomic nuclei do not possess static dipole moments. Here, the deformed Fermi distribution

$$\rho_{ca\beta}(r, \vartheta) = \frac{N}{1 + \exp(\frac{r - c(1 + \beta_2 \text{Y}_{20}(\vartheta) + \beta_4 \text{Y}_{40}(\vartheta))}{a})} \tag{2.6}$$

as a model of the nuclear charge distribution has proved to be very successful, e.g. in heavy muonic atom spectroscopy with deformed nuclei [112,117]; the normal Fermi distribution ($\beta_i=0$) has also been used in electron-nucleus scattering experiments determining the nuclear charge distribution [164]. Here, a is a skin thickness parameter and c the half-density radius, while β_2, β_4 are deformation parameters. $\text{Y}_{lm}(\vartheta, \varphi)$ are the spherical harmonics and $\text{Y}_{l0}(\vartheta)$ depend only on the polar angle ϑ, and not on the azimuthal angle φ. The normalization constant N is determined by the condition

$$\int \text{d}^3 r \, \rho_{ca\beta}(r, \vartheta) = 1.$$

For the deformed Fermi distribution (2.6) with a fixed charge number Z, the g factor (2.3) is completely determined by the parameters c, a and β_i, and therefore can be written for the ground state as

$$g = g_{\text{point}} + \delta g_{\text{FS}}^{(ca\beta)}, \tag{2.7}$$

where $\delta g_{\text{FS}}^{(ca\beta)}$ is the finite size correction depending on the parameters c, a, and β_i. In [82], the ND correction to the bound electron g factor is defined as the difference of the finite size effect due a deformed charge distribution and due to a symmetric charge distribution (i.e. $\beta_i=0$) with the same nuclear radius as

$$\delta g_{\text{ND}} = \delta g_{\text{FS}}^{(c_1 a\beta)} - \delta g_{\text{FS}}^{(c_2 a 0)},$$

where $a = 2.3 \, \text{fm}/(4\ln(3))$, and c_i are determined such that $\sqrt{\langle r^2 \rangle_\rho}$ of the corresponding charge distribution agrees with the root-mean-square (RMS) values from literature [165]. The n-th moment of a charge distribution $\rho(\vec{r})$ is defined as

$$\langle r^n \rangle_\rho = \int \text{d}^3 \mathbf{r} \, r^n \rho(\mathbf{r}).$$
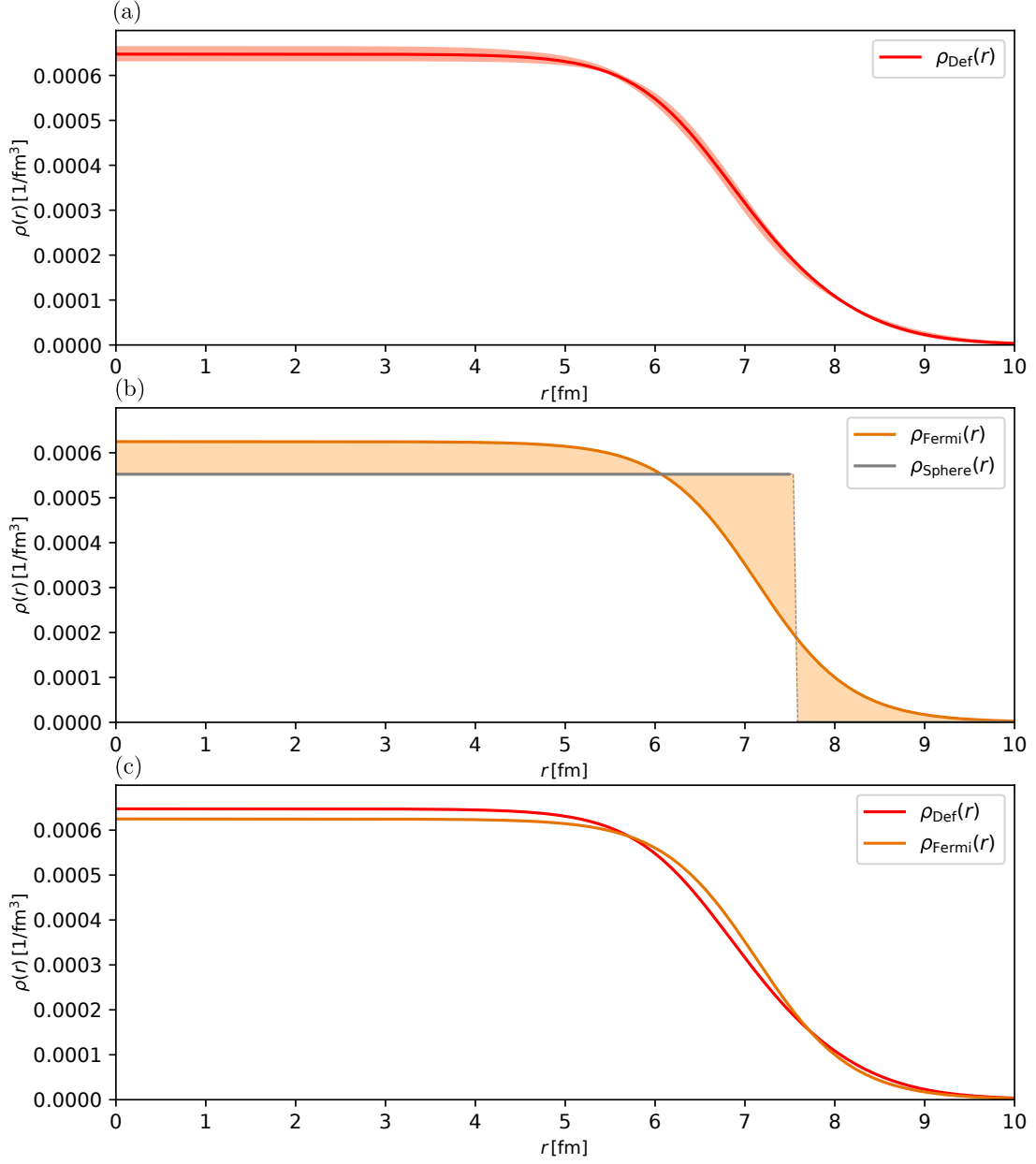
Figure 2.1:
(a): Averaged deformed Fermi distribution from Eq. 2.2 for ^{238}U, where the parameters and their uncertainties are taken from [160]. The light red border shows the uncertainties due to the parameters a, β_2, β_4, which is the remaining model uncertainty once the nuclear charge radius is fixed and which enables a reduced model uncertainty in the finite nuclear size g-factor correction.
(b): (Non-deformed) Fermi distribution with $a = 0.5234$ fm and homogeneously charged sphere with the same RMS charge radius as the deformed Fermi distribution. The difference (in light orange) is the conventional model uncertainty of the unclear charge distribution, which is larger compared to using the deformed Fermi distribution in figure a).
(c): Comparison of non-deformed and averaged, deformed Fermi distribution with the same RMS radius. The difference causes the nuclear deformation effect.

Values for the deformation parameter β_2 can be obtained by literature values of the reduced E2-transition probabilities from a nuclear state 2_i^+ to the ground state 0^+ via [166]:

$$\beta_2 = \frac{4\pi}{3Z|e|\sqrt{5\langle r^2\rangle_\rho/3}}\left[\sum_i B(E2;0^+\to 2_i^+)\right]^{1/2}$$

From Eq. (2.4) it is evident that the ND correction is a difference of two finite size effects and therefore especially sensitive on higher order effects. However, for high Z it reaches the 10^{-6} level and therefore is very significant.

It was shown in [82] with the ERM [159] that $\delta g_{\mathrm{FS}}^{(ca\beta)}$ and therefore δg_{ND} mainly depends on the moments $\langle r^2\rangle_\rho$ and $\langle r^4\rangle_\rho$. δg_{ND} can be calculated with the formula [163]

$$\delta g_{\mathrm{FS}}^{(ca\beta)} = \frac{4}{3}\frac{\partial E_{\mathrm{FS}}(c,a,\beta)}{\partial m_e}, \tag{2.8}$$

which is a direct consequence of Eq. (2.4) and where $E_{\mathrm{FS}}(c,a,\beta)$ is the energy correction due to $\rho_{ca\beta}(r,\vartheta)$ compared to the point like nucleus. The effective radius R is defined as the radius of a homogeneously charged sphere with the same energy correction $E_{\mathrm{FS}}^{(\mathrm{sph})}(R)$ as the deformed Fermi distribution via

$$E_{\mathrm{FS}}^{(\mathrm{sph})}(R) = E_{\mathrm{FS}}(c,a,\beta). \tag{2.9}$$

The energy correction can be approximated [159] as

$$E_{\mathrm{FS}}^{(\mathrm{sph})}(R) \approx \frac{(Z\alpha)^2}{10}\left[1+(Z\alpha)^2 f(Z\alpha)\right](2Z\alpha R m_e)^{2\gamma}m_e. \tag{2.10}$$

Here, $f(x) = 1.380 - 0.162x + 1.612x^2$ and the effective radius is approximately

$$R \approx \sqrt{\frac{5}{3}\langle r^2\rangle_{\rho_{ca\beta}}\left[1-\frac{3}{4}(Z\alpha)^2\left(\frac{3}{25}\frac{\langle r^4\rangle_{\rho_{ca\beta}}}{\langle r^2\rangle_{\rho_{ca\beta}}^2}-\frac{1}{7}\right)\right]}. \tag{2.11}$$

While Eq. (2.8) is exact for an arbitrary central potential, provided that E_{FS} is known exactly, Eq. (2.10) is an approximation derived under the assumption of the difference between point-like and extended potential being a small perturbation. The calculation of the ND correction to the bound electron g factor via the effective radius approach therefore relies on a perturbative evaluation of the energy derivative in Eq. (2.8) and is limited by the accuracy of the finite size corrections.

In this work, the ND g-factor correction is calculated with three methods: Firstly, with the previously used analytical ERM described above. Secondly, with a numerical ERM, where instead of the approximative Eqs. (2.10) and (2.11), Eq. (2.9) is solved numerically for R and the ND g-factor correction is obtained by using Eq. (2.3) with the wave functions of the corresponding charged sphere. Finally, we also calculate δg_{ND} non-perturbatively by solving the Dirac equation (3.10) numerically with the dual kinetic balance method [167] for the potential (2.2), including all finite size effects due to the deformed charge distribution $\rho_{ca\beta}(r,\vartheta)$. Then, the g factors in Eq. (2.4) for the ND
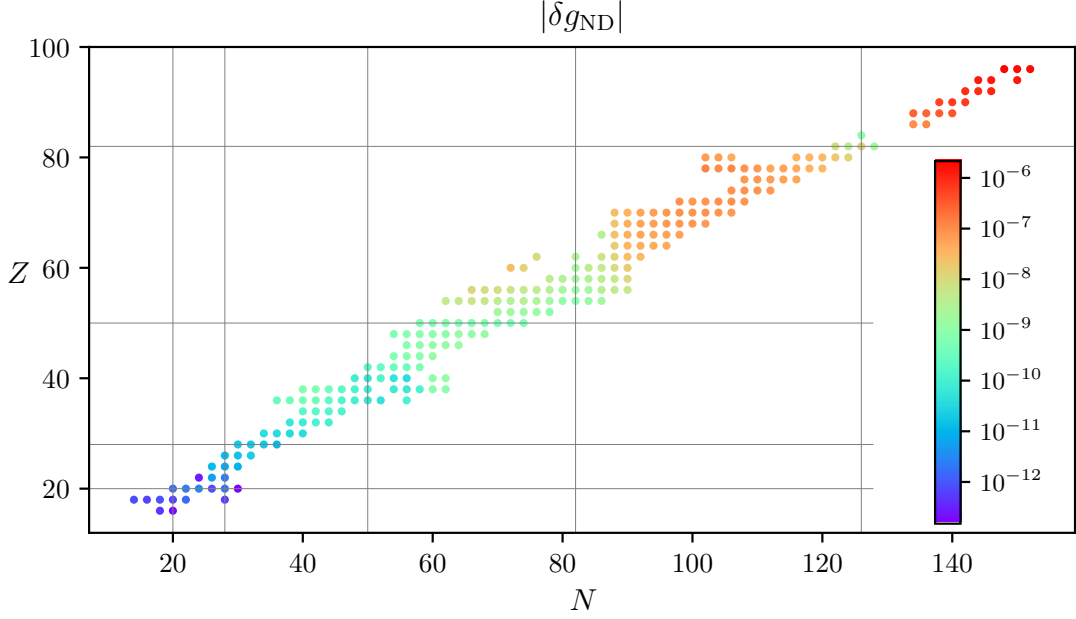
Figure 2.2: Nuclear chart with charge number Z and neutron number N, where the grey lines indicate the magic numbers 20, 28, 50, 82, and 126. The points represent even-even nuclei, where their color displays the ND g-factor correction δg_{ND}, calculated with the numerical, non-perturbative approach, which takes particularly low values around the magic numbers and larger values in between. See [168] for an evaluation with the previously used perturbative method.

correction can be obtained by numerical integration of the wave functions in Eq. (2.3). Alternatively, the derivative of the energies in Eq. (2.4) can be calculated numerically as

$$\frac{\partial E_{n\kappa}}{\partial m_e} \approx \frac{E_{n\kappa}^{(m_e + \delta m_e)} - E_{n\kappa}^{(m_e - \delta m_e)}}{2\delta m_e},$$

with a suitable $\delta m_e/m_e \ll 1$, since the uncertainty of the numerical derivative scales as $(\delta m_e/m_e)^3$. Here, $E_{n\kappa}^{(m_i)}$ stands for the binding energy obtained by solving the Dirac equation with the electron mass replaced by m_i. We find both methods in excellent agreement.

We calculated the ND g-factor correction for a wide range of even-even, both in the proton and neutron number, and therefore spinless nuclei with charge numbers between 16 and 96 using the deformed Fermi distribution from Eq. (2.6) with parameters a, c, and β obtained as described below Eq. (2.4). The required RMS values for the nuclear charge radius are taken from [165] and the reduced transition probabilities needed for the calculation of β via (2.4) from [169]. The resulting values for $|\delta g_{\mathrm{ND}}|$, obtained by the non-perturbative method, are shown in Fig. 2.2 as a function of the charge number Z and the neutron number N. If proton or neutron number is in the proximity of a nuclear magic number 2, 8, 20, 28, 50, 82, and 126, which corresponds to a filled proton

or neutron shell [170], the nuclear shell closure effects also transfer to the bound electron g factor, and the ND correction is reduced, as already indicated perturbatively in [168]. In Table 2.1, a comparison between all our numerical approaches and the analytical ERM from [82] is shown.

Now, let us discuss the main causes for the disagreement of the results as presented in Table 2.1. Both Eqs. (2.10) and (2.11) are approximations derived by perturbation theory, which affects the accuracy of the analytical ERM $\delta g_{\mathrm{ND}}^{(\mathrm{eff,A})}$. Eq. (2.10) has an estimated relative uncertainty $\lesssim 0.2\,\%$ [159] and (2.11) uses only the second and fourth moment of the nuclear charge distribution for finding the effective radius. Also, it was shown in [161] that the analytical ERM for arbitrary charge distributions is incomplete in order $(Z\alpha)^2 m_e (Z\alpha m_e R_N)^3$, where R_N is the nuclear RMS charge radius. Furthermore, even if the effective radius is calculated without approximations according to Eq. (2.9), the wave functions of the corresponding homogeneously charged sphere differ slightly from the ones of the deformed Fermi distribution with the same binding energy. This affects values of the g factor and explains the difference between the numerical ERM $\delta g_{\mathrm{ND}}^{(\mathrm{eff,N})}$ and the direct numerical calculations $\delta g_{\mathrm{ND}}^{(\mathrm{num})}$. Finally, being a difference of two small finite-nuclear-size corrections, the ND correction can exhibit enhanced sensitivity on the uncertainty of the ERM. From Table 2.1, we conclude that for high Z, the difference between analytical ERM and non-perturbative calculations is mainly due to the approximations in Eqs. (2.10) and (2.11).

Concluding, the analytical ERM proved to be a good order-of-magnitude estimate of the ND correction, but for high-precision calculations, non-perturbative methods beyond the ERM and without any expansion in $Z\alpha$ or $Z\alpha\,m_e\,R_N$ are indispensable. Convergence of the numerical methods was checked by varying numerical parameters and using different grids, and the obtained accuracy permits the consideration of nuclear size and shape with an accuracy level much higher than the differences to the perturbative method.

Previously, the uncertainty of the finite nuclear size correction was commonly estimated as the difference between the Fermi distribution and a homogeneously charged sphere, which is a very conservative estimate [86]. If the finite size correction is calculated as $\delta g_{\mathrm{FS}}^{(ca\beta)}$ from Eq. (2.7) including deformation effects, the remaining model uncertainty is reduced to the difference between the deformed Fermi distribution and the true, unknown nuclear charge distribution. As a consequence, precise values for c, a, and β need to be known, e.g. from muonic atoms spectroscopy [112, 171], along with their error bars, which are needed to estimate the difference between deformed Fermi and true charge distribution. The reduction of model uncertainties is demonstrated in Fig 2.1. Here, the averaged charge distribution for the deformed Fermi distribution with parameters from [160] is shown along with errorbars due to the uncertainties in a, c, β_2, and β_4. For comparison, the conventional way of estimating the model dependence is also demonstrated by showing difference between the non-deformed Fermi and charged sphere charge distribution.

For values of the RMS radius, a, β_2, and β_4 of ^{238}U taken from Ref. [160], it is shown it Table 2.2 that accounting for the deformation effects reduces the uncertainty of the finite size correction by more than a factor of two. Also, it shows that the difference of the ERM and the all-order numerical method is larger than the uncertainty due to

nuclear parameters.

In summary, the ND g-factor correction was calculated non-perturbatively for a wide range of nuclei by using quadrupole deformations estimated from nuclear data. By comparing the previously used perturbative ERM and the all-order numerical approach, it was shown that the contributions of the non-perturbative effects can amount up to the $20\,\%$ level. In the low-Z regime, the ND corrections can safely be neglected, especially for the ions considered in [58]. However, considering a ND correction up to the parts-per-million level and an expected parts-per-billion accuracy, or even below, for the g-factor experiments with high-Z nuclei, in this case an all-order treatment is indispensable. For hydrogen-like Uranium, it was shown that inclusion of deformation effects leads to reduced uncertainties in the theoretical prediction of the finite nuclear size correction. On the other hand, since the distribution of electric charge inside the nucleus is a major theoretical uncertainty for g factors with heavy nuclei, the extraction of information thereon from experiments is possible. Our work demonstrates the required accurate mapping of arbitrary nuclear charge distributions to corresponding g factors.

Table 2.1: Comparison of the ND g factor correction obtained by the ERM with the analytical expressions from Eqs. (2.10) and (2.11) $\delta g_{\mathrm{ND}}^{(\mathrm{eff,A})}$, by the ERM with effective radius and corresponding energy correction calculated numerically $\delta g_{\mathrm{ND}}^{(\mathrm{eff,N})}$ and non-perturbatively by direct numerical calculations $\delta g_{\mathrm{ND}}^{(\mathrm{num})}$ for several isotopes. R_N is the RMS nuclear electric charge radius from literature [165] and β_2 is the parameter of the deformed Fermi distribution (2.6). $\beta_4 \approx 0$ is assumed, according to [172]. All methods, as well as the procedure for obtaining the parameters of the deformed Fermi distribution, are described in the text.

	$R_N(\mathrm{fm})$	β_2	$\delta g_{\mathrm{ND}}^{(\mathrm{eff,A})}$	$\delta g_{\mathrm{ND}}^{(\mathrm{eff,N})}$	$\delta g_{\mathrm{ND}}^{(\mathrm{num})}$
$^{58}_{26}$Fe	3.775	0.273	-2.19×10⁻¹¹	-2.02×10⁻¹¹	-2.11×10⁻¹¹
$^{82}_{38}$Sr	4.246	0.263	-3.56×10⁻¹⁰	-3.16×10⁻¹⁰	-3.27×10⁻¹⁰
$^{98}_{44}$Ru	4.423	0.194	-6.00×10⁻¹⁰	-5.25×10⁻¹⁰	-5.41×10⁻¹⁰
$^{116}_{48}$Cd	4.628	0.189	-1.20×10⁻⁹	-1.04×10⁻⁹	-1.07×10⁻⁹
$^{116}_{50}$Sn	4.627	0.108	-5.11×10⁻¹⁰	-4.42×10⁻¹⁰	-4.55×10⁻¹⁰
$^{134}_{54}$Xe	4.792	0.113	-1.09×10⁻⁹	-9.36×10⁻¹⁰	-9.62×10⁻¹⁰
$^{152}_{64}$Gd	5.082	0.202	-1.53×10⁻⁸	-1.29×10⁻⁸	-1.32×10⁻⁸
$^{208}_{82}$Pb	5.501	0.061	-1.35×10⁻⁸	-1.10×10⁻⁸	-1.13×10⁻⁸
$^{244}_{94}$Pu	5.864	0.287	-1.28×10⁻⁶	-1.03×10⁻⁶	-1.05×10⁻⁶
$^{248}_{96}$Cm	5.825	0.299	-1.70×10⁻⁶	-1.36×10⁻⁶	-1.39×10⁻⁶

Table 2.2: Comparison of the finite nuclear size correction for the normal Fermi distribution $\delta g_{\mathrm{FS}}^{(\mathrm{Fermi})}$ and the deformed Fermi distribution $\delta g_{\mathrm{FS}}^{(ca\beta)}$, evaluated with the effective radius method (ERM) and numerically. The number in the first and second parenthesis is the uncertainty due to the RMS charge radius and the model uncertainty, respectively. Parameters are taken from Ref. [160]. The results show that considering a deformed charge distribution can significantly reduce the model uncertainty. Furthermore it demonstrates, that the numerical method needs to be used for precise calculations.

	ERM	Numerical
$\delta g_{\mathrm{FS}}^{(\mathrm{Fermi})}$	$1.2860(11)(31) \times 10^{-3}$	$1.2739(11)(25) \times 10^{-3}$
$\delta g_{\mathrm{FS}}^{(ca\beta)}$	$1.2852(11)(9)\ \times 10^{-3}$	$1.2733(11)(7)\ \times 10^{-3}$

2.5 Conclusion

At first, in this Chapter, the following known results are summarized:

- For spinless nuclei, the angular dependence of the interaction energy averaged out and the bound electron is exposed to a averaged, spherically symmetric nuclear potential.

- For these spherically symmetric potentials, the bound electron g factor can be calculated by solving the Dirac equation and then performing radial integrals or deriving the binding energy by the electron mass.

- Deformed charge distributions cause a nuclear shape or nuclear deformation effect on the g factor, which can be calculated perturbatively with the effective radius method according to [82].

From thereon, the following new results are presented in this thesis:

- The nuclear shape correction is calculated without using the perturbative effective radius method. Instead, the averaged potential is calculated numerically starting from a given deformed charge distribution. Then, finite basis set methods are used to solve the Dirac equation numerically in this potential and the integrals and energy derivatives for the bound electron g factor are also performed numerically. Thereby, nuclear deformation effects on the bound electron g factor are obtained non-perturbatively.

- Results for a wide range of nuclei were presented using the non-perturbative method. It was shown that the results for the deformation effects of the previously used perturbative effective radius method differ from the non-perturbative results on the 20%-level.

- For Uranium-238, it was shown with parameters of the deformed charge distribution that the uncertainty of the finite nuclear size effect can be reduced by a factor of two by considering deformation effects.

Chapter 3

Level structure of muonic atoms

This chapter is devoted to the prediction of the level structure and transition probabilities in muonic atoms with focus on high nuclear charge numbers. Compared to conventional atomic electrons, the much higher muon mass reduces the length- and increases the energy scales by the muon-electron mass ratio. Thereby, all finite nuclear size and shape effects are much more important and excited nuclear states also have to be taken into account.

This chapter is organized in the following way:

At first, a motivation for new structure calculations is given in Section 3.1.1. The current status of existing methods is reviewed and new experiments in the field are explained, which use the results presented in this thesis.

Afterwards, the theoretical framework and implementation of several important effects is shown in Sections 3.1.2 to 3.1.4. Here, finite basis set methods suitable for precision calculations are used and results for selected nuclei are presented.

In Sections 3.2.2 and 3.2.1, improved methods for the calculation of higher order effects in electric hyperfine interactions are presented.

Finally, in Sections 3.3, calculations in combination with recent experiments on isotopically pure rhenium-185 are presented. Here, a combination of theoretical predictions and experimental measurements of muonic transitions enables the extraction of the nuclear quadrupole moment.

In Section 3.4, high-precision calculations for one- and two-loop vacuum polarization corrections to the bound-muon g factor in muonic Helium-4 are shown.

3.1 Calculation of spectra for muonic atoms

3.1.1 Motivation

Atomic nuclei are one of the building blocks of matter and therefore, information on their structure, like the distribution of electric charge inside the nucleus, is of intrinsic interest. Furthermore, the charge radii of atomic nuclei are of importance as an input parameter for the interpretation of other experiments. For example, radium is candidate for measuring atomic parity violation effects, but for this more accurate values of the radium charge radii are needed [173]. There are several methods for extracting information on the nuclear charge distribution, i.e. the distribution of protons inside the atomic nucleus, like electron scattering [174] or laser spectroscopy [175–177]. One method is also muonic atom spectroscopy. Here, a muon, which is a negatively charged elementary particle is brought in the proximity of an atomic nucleus. Then, the negatively charged muon forms

bound states with the positively charged nucleus and radiation due to muonic transitions can be analyzed in order to extract information on the nuclear charge distribution and measure quantities like nuclear charge radii and quadrupole moments.

Correspondingly, the theory of muonic atoms has been developed in order to describe the level structure and the probabilities for muonic transitions. The general approach is that for a given nuclear charge distribution, the spectrum of the corresponding muonic atom needs to be predicted. Then, vice versa, for a measured spectrum the nuclear charge distribution can be extracted. An overview of the different contributions to the energy levels of muonic atoms can be found in [122]. Hitherto, the majority of analyses of the spectra of heavy muonic atoms used the computer programs `MUON` and `RURP` [125]. There are two main differences compared to the approach used in this thesis: Firstly, the dual-kinetic-balance method [149] is used in this thesis. Being a finite basis set method, an approximation of the complete muon spectrum can obtained, i.e. bound states and positive as well as negative continuum states, including the effects of the finite nuclear charge distribution. Thereby, numerical summations over the complete muon spectrum are possible. This enables for example a complete treatment of the second order hyperfine interactions, as presented in Section 3.2.2. Secondly, whereas in the *MUON* and *RURP* codes, the fine and hyperfine structure are calculated separately, in this thesis the calculations of the fine and hyperfine structure are performed at once, based on a given nuclear charge distribution, enabling improved analysis of the dependence of the muonic spectrum on parameters of the nuclear charge distribution.

Furthermore, there are new experiments on high Z muonic atoms being performed by the MuX-Collaboration at the Paul Scherrer Institute (PSI) in Villigen, Switzerland [178]. One of the goals is to measure the charge radius for radium, needed for experiments on atomic parity violations, as mentioned earlier in this Section. Furthermore, measurements on muonic atoms involving several nuclei will be or have been performed for the first time, involving isotopically pure rhenium. The corresponding structure calculations for muonic rhenium were performed during the work on this thesis, and results are presented in Section 3.3.

3.1.2 Theoretical framework

A muon is a charged elementary particle, which is in many aspects similar to the electron, in particular, it has the same electric charge, but it is ≈ 200 times heavier than the electron [179]. When coming close to an atom, a muon can be captured by the nucleus and form a hydrogen-like muonic ion. This atomic system is commonly referred to as a muonic atom. The lifetime of the muon is big enough to be considered stable in the structure calculations of these muonic bound states. In muonic atoms, nuclear effects on the energy levels are much larger compared to conventional electronic atoms. This can be seen by considering the ratio of the nuclear radius and the Bohr radius of the bound fermion, which is the typical length scale for the bound muon or electron. The larger this ratio is, the larger are nuclear finite size effects. The Bohr radius for a hydrogen-like atomic system with a bound fermion of mass m_f and a nuclear charge number Z reads as

$$r_B = \hbar/(m_f c Z \alpha),$$

Table 3.1: Comparison of the ratio of nuclear charge radius R_N to the Bohr radius r_B of a bound electron or muon in the corresponding hydrogen-like atomic system for hydrogen, helium, rhenium, and uranium. If this ratio is small, the finite size of the nucleus does not influence the bound fermion significantly. On the other hand, if this ratio is on the order of 1, large finite nuclear size and nuclear structure effects can be expected. The nuclear charge radii are taken from [165].

Fermion type	Nucleus	R_N[fm]	r_B[fm]	R_N/r_B
e^-	$^1_1$H	0.8783	52917.721	1.660×10^{-5}
μ^-	$^1_1$H	0.8783	255.928	3.432×10^{-3}
e^-	$^4_2$He	1.6755	26458.861	6.332×10^{-5}
μ^-	$^4_2$He	1.6755	127.964	1.309×10^{-2}
e^-	$^{185}_{75}$Re	5.3596	705.570	7.596×10^{-3}
μ^-	$^{185}_{75}$Re	5.3596	3.412	1.571
e^-	$^{238}_{92}$U	5.8571	575.193	1.018×10^{-2}
μ^-	$^{238}_{92}$U	5.8571	2.782	2.105

where $\hbar$ is the Planck's constant, α is the fine-structure constant and c is the speed of light in vacuum. In Table 3.1, the nuclear radius, the Bohr radius for the corresponding electronic and muonic hydrogen-like ion, and their ratio is shown for a selection of nuclei, from very light to very heavy. It can be seen that, that for electronic atoms, the nucleus is generally a few orders of magnitude smaller compared to the extend of the electronic wave function, which is given by the Bohr radius, although for high Z, the electron is much closer to the nucleus due to the strong Coulomb attraction. Since the Bohr radius is inversely proportional to the mass of the bound fermion, the situation in muonic atomic systems is different. While for low Z, the extend of the muonic wave functions is still much larger than the nuclear radius, for high Z, the nuclear radius is actually larger than the muonic Bohr radius. In Fig. 3.1, the muonic and electronic ground state wave functions for hydrogen-like uranium are shown in comparison to the nuclear charge distribution. This means the overlap between muonic wave functions and nucleus is large in this case. Also, a typical energy scale for hydrogen-like systems is the ground state binding energy from Eq. (1.22) for a point-like nucleus, which reads as

$$E_{0,\text{point}} = m_f c^2 (1 - \sqrt{1 - (Z\alpha)^2}),$$

and is proportional the fermion mass. As a consequence, for muonic atoms and high charge numbers, muonic transitions can have an energy of several MeV and fine-structure splitting can be on the order of $100 \, \text{keV}$. Excitation energies of nuclear rotational states are of the same order [169] and therefore a nuclear model has to be used, which besides an extended charge distribution also contains the excited nuclear states of the ground
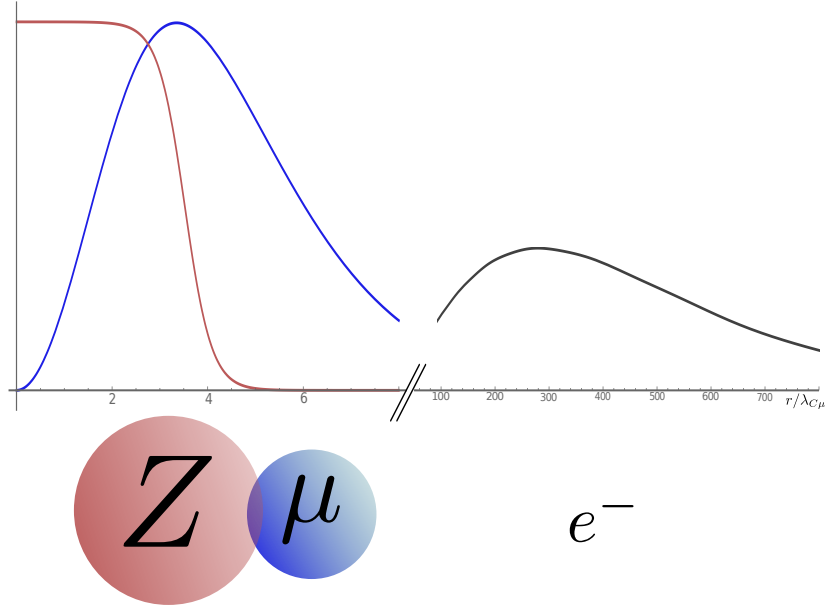
Figure 3.1: The monopole charge distribution for the nucleus (red) and the $1s1/2$ wave functions of the muon (blue) and the electron (gray, enhanced by factor 50) for hydrogen-like uranium. The muonic wave function overlaps strongly with the nuclear charge distribution. Therefore finite nuclear size effects are enhanced in muonic atoms

state rotational band. Here, the symmetric rigid rotor model model for nuclei with axial symmetry has proved successful in describing heavy muonic atoms, e.g. [112, 117, 123, 124] and also is used in this thesis. The symmetric rigid rotor model is presented in Appendix D, where also the expressions for the nuclear wave functions in terms of Wigner D functions can be found. In the symmetric rigid rotor model, the nucleus is described by a charge distribution $\rho(\mathbf{r})$ given in the body fixed nuclear frame, and the Euler angles $\Omega = (\phi, \theta, \psi)$ describe its position in the laboratory frame. The rotational state of the nucleus $|IMK\rangle$ is given by the total nuclear angular momentum quantum number I, its projection on the z axis of the laboratory frame M and on the z axis of the body fixed frame K, where K also corresponds to the ground state angular momentum. As derived in Chapter 1, the muonic bound states without radiative corrections can be obtained by solving the Dirac equation for the nuclear potential. The coupled system of muon as a Dirac particle and nucleus as a rigid rotor therefore is described by the eigenvalue equation

$$\mathrm{H}\left(|N\rangle \otimes |\mu\rangle\right) = \left(\mathrm{H_N} + \mathrm{H}_\mu + V_{\mathrm{el}}\right)\left(|N\rangle \otimes |\mu\rangle\right) = E\left(|N\rangle \otimes |\mu\rangle\right), \tag{3.1}$$

where H_{N} is the nuclear rigid rotor Hamiltonian, and $H_\mu = \boldsymbol{\alpha} \cdot \mathbf{p} + \beta m_\mu$ is the free Dirac Hamiltonian for the muon with momentum $\mathbf{p}$, and $\boldsymbol{\alpha}$, β are the four Dirac matrices. $|N\rangle$ is the nuclear state and $|\mu\rangle$ is the muon state. Following Eq. (1.16), the electric potential

energy between muon and nuclear charge distribution reads as

$$V_{\mathrm{el}}(\mathbf{r}'_\mu) = -Z\alpha \int \mathrm{d}^3 r'_N \frac{\rho(\mathbf{r}'_N)}{|\mathbf{r}'_\mu - \mathbf{r}'_N|}. \tag{3.2}$$

It is important to recall, that the nuclear charge distribution is given in the body fixed nuclear frame, thus the integration in Eq. (3.2) in most conveniently performed in this frame. The resulting expression in dependence of the position of the muon, however, is needed in the laboratory frame. Therefore, in the following, a multipole expansion of Eq. (3.2) is performed, and the result is given as a function of the muon position in the laboratory frame and the Euler angles describing the orientation of the nuclear frame. Here, vectors are written is spherical components as $\mathbf{r}_i = (r_i, \vartheta_i, \varphi_i)$ in the laboratory frame and as $\mathbf{r}'_i = (r'_i, \vartheta'_i, \varphi'_i)$ in the body-fixed nuclear frame. Since rotations do not change the absolute values, it holds that $r'_i = r_i$.

With the multipole expansion of the Coulomb potential [162]

$$\frac{1}{|\mathbf{r}'_\mu - \mathbf{r}'_N|} = \sum_{l=0}^\infty \frac{r_<^l}{r_>^{l+1}} \sum_{m=-l}^l \mathrm{C}^*_{lm}(\vartheta'_N, \varphi'_N)\mathrm{C}_{lm}(\vartheta'_\mu, \varphi'_\mu),$$

where $r_< := \min(r_\mu, r_N)$, $r_> := \max(r_\mu, r_N)$, the electric potential (3.2) can be written as

$$V_{\mathrm{el}}(\mathbf{r}'_\mu) = \sum_{l,m} -Z\alpha \left[\int \mathrm{d}^3 r'_N \frac{r_<^l}{r_>^{l+1}} \mathrm{C}^*_{lm}(\vartheta'_N, \varphi'_N)\rho(\mathbf{r}'_N) \right] \mathrm{C}_{lm}(\vartheta'_\mu, \varphi'_\mu),$$

where $\mathrm{C}_{lm}(\vartheta, \varphi) = \sqrt{4\pi/(2l+1)}\mathrm{Y}_{lm}(\vartheta, \varphi)$ are the normalized spherical harmonics. For axially symmetric charge distributions, only the $m=0$-terms contribute after integrating over the charge distribution. The dependency on the muonic angular variables can be transformed to the laboratory system using the Euler angles by

$$\mathrm{P}_l(\cos\vartheta'_\mu) = \sum_{m=-l}^l C^*_{lm}(\theta, \phi)C_{lm}(\vartheta_\mu, \varphi_\mu),$$

which is a special case of Eq. (C.1). Thereby, the potential as a function of the Euler angles and the muon's position in the laboratory frame reads

$$\begin{aligned}
V_{\mathrm{el}}(\mathbf{r}_\mu, \phi, \theta) &= \sum_{l=0}^\infty -Z\alpha \left[\int \mathrm{d}^3 r'_N \frac{r_<^l}{r_>^{l+1}} \mathrm{P}_l(\cos\vartheta'_N)\rho(\mathbf{r}'_N) \right] \sum_{m=-l}^l \mathrm{C}^*_{lm}(\theta, \phi)\mathrm{C}_{lm}(\vartheta_\mu, \varphi_\mu). \\
&=: \sum_{l=0}^\infty Q_{\mathrm{el}}^{(l)}(r_\mu) \sum_{m=-l}^l C^*_{lm}(\theta, \phi)C_{lm}(\vartheta_\mu, \varphi_\mu) \\
&=: \sum_{l=0}^\infty V_{\mathrm{el}}^{(l)}(\mathbf{r}_\mu, \phi, \theta), \tag{3.3}
\end{aligned}$$

where $Q_{\mathrm{el}}^{(l)}(r_\mu)$ describe the radial distribution of the multipole moments and the de-

pendency on the muonic angles and the Euler angles is in form of a scalar product of spherical tensor operators. This means, as expected the interaction energy does only depend on the relative orientation of the muon with respect to the body fixed nuclear z' axis.

Most nuclei turn out to be symmetric with respect to reflection in the (x', y')-plane [180]. This results in only even-l terms in Eq. (3.3) being non-zero, thus the first to terms are the monopole term $l = 0$ and the quadrupole term $l = 2$. The next term would be the $l = 4$ hexadecapole terms, however, usually, higher order terms are not needed for the correct description of the hyperfine level structure [122]. It follows from Eq. (3.3), that the monopole terms only depends on the muonic radial variable, since it can be written as

$$V_{\text{el}}^{(0)}(r_\mu) = -Z\alpha \int \mathrm{d}^3\mathbf{r}'_N \frac{\rho(\mathbf{r}'_N)}{r_>}.$$

In fact, the $l = 0$ term is the averaged nuclear potential already derived in Eq. (2.2) in the previous chapter on the g factor of spinless nuclei. As a consequence, the $l = 0$-term can be used as a potential in the spherically symmetric Dirac equation to define the unperturbed muonic states as

$$\left(\boldsymbol{\alpha} \cdot \mathbf{p} + \beta m_\mu + V_{\text{el}}^{(0)}(r_\mu)\right) |n\kappa m\rangle = E_{n\kappa} |n\kappa m\rangle. \tag{3.4}$$

The unperturbed nuclear states are the rigid rotor states from Eq. (D.2) with

$$\mathrm{H}_N |IMK\rangle = E_N |IMK\rangle, \tag{3.5}$$

where the excitation energies of the nuclear rotational states are typically taken from experiments [169], and not parametrized by the moment of inertia from Eq. (D.1). The $l = 2$ quadrupole term couples nuclear and muonic degrees of freedom and is treated in perturbation theory in Sections 3.1.3.5, 3.1.4, and 3.2.2. The multipole interaction from Eq. (3.3) in general, and the quadrupole interaction with $l = 2$ in particular has the structure of a scalar product of two irreducible tensor operators, as defined in Eq. (C.4). One operator acts on the nuclear angular variables, i.e. the Euler angles, and one on the muonic angular variables. For these types of operators, the calculation of expectation values can be simplified by using the theory of irreducible tensor operators, as described in Appendix C. For applying formula (C.5). Therefore, states of defined total angular momentum have to be considered as

$$|FM\,IK\,n\kappa\rangle = \sum_{M_N, m} \mathrm{C}_{IM_N\,j(\kappa)m}^{FM} |IM_NK\rangle \, |n\kappa m\rangle \tag{3.6}$$

with total angular momentum F, nuclear angular momentum I and muonic angular momentum j are defined. The muonic angular momentum j is already composed out of the orbital angular momentum l and the spin angular momentum, as described in Eq. (1.19). The total energy of the muon-nucleus system can be calculated as the sum of nuclear energy E_N from Eq. (3.5), the muonic energy from Eq. (3.4) and the expactation value of the quadrupole interaction $\left\langle V_{\text{el}}^{(2)} \right\rangle$ from Eq. (3.3).

3.1.3 Fine and first order hyperfine structure

In this Section, the solution of the Dirac equation for the muon will be discussed, in particular the effects of vacuum polarization in Uehling approximation, recoil corrections, electron screening are implemented, using known methods. Especially, the usage of the dual-kinetic-balance method [149] in the framework of muonic atoms is presented. In the following, the first order hyperfine structure is considered. Results are presented for muonic ^{205}Bi, ^{147}Sm, and ^{89}Zr. This Section follows [1], which was published in the framework of this thesis.

3.1.3.1 Finite nuclear size corrections

For considering monopole and quadrupole interactions, the nuclear charge distribution is divided into a spherically symmetric part $\rho_0(r)$ and a part $\rho_2(r)$ describing the quadrupole distribution in the nuclear frame as [112]

$$\rho(\mathbf{r}') = \rho_0(r') + \rho_2(r') Y_{20}(\vartheta', \varphi'), \tag{3.7}$$

with the spherical harmonics $Y_{lm}(\vartheta, \varphi)$. Since an analogous part for the dipole distribution would be an operator of odd parity, it would vanish after averaging with muon wave functions of defined parity [181], and thus it is not considered here and neither are higher multipoles beyond the quadrupole term. Correspondingly, the electric potential from Eq. (3.3) contains only the monopole and quadrupole part, and can be written as

$$V_{\mathrm{el}}(\mathbf{r}_\mu, \phi, \theta) = V_{\mathrm{el}}^{(0)}(r_\mu) + V_{\mathrm{el}}^{(2)}(\mathbf{r}_\mu, \phi, \theta), \tag{3.8}$$

where the spherically symmetric part of the charge distribution can be written as

$$V_{\mathrm{el}}^{(0)}(r_\mu) = -4\pi Z\alpha \int_0^\infty \mathrm{d}r\, r^2 \frac{\rho_0(r)}{r_>}, \tag{3.9}$$

with $r_> = \max(r, r_\mu)$. This interaction potential will be included in the numerical solution of the Dirac equation for the muon as described in Sec. 3.1.3.1. The quadrupole part of the interaction $V_{\mathrm{el}}^{(2)}$ causes hyperfine splitting, which is calculated perturbatively in Sec. 3.1.3.5.

The appropriate states have well-defined angular momentum, as introduced in Eq. (3.6). As a basis for further calculations, the Dirac equation

$$\left(\boldsymbol{\alpha} \cdot \mathbf{p} + \beta + V_{\mathrm{el}}^{(0)}(r_\mu) \right) |n\kappa m\rangle = (1 - E_{n\kappa}^{(B)}) |n\kappa m\rangle \tag{3.10}$$

is solved for the muon. Here, $E_{n\kappa}^{(B)}$ are the binding energies, and the potential $V_{\mathrm{el}}^{(0)}(r_\mu)$ is the spherically symmetric part of the interaction with the nucleus. This is the monopole contribution from the electric interaction in Eq. (3.9) and, if vacuum polarization is considered, the Uehling potential from Eq. (3.13). A Fermi type charge distribution [182]

is used to model the monopole charge distribution as

$$\rho_0(r) = \frac{N}{1 + \exp((r-c)/a)}, \tag{3.11}$$

where a is a skin thickness parameter and c the half-density radius. The normalization constant N is chosen such that the volume integral is equal to one, since the charge is already included in the fine-structure constant. It has been proven, that $a = t/(4\log 3)$, with $t = 2.30\,\text{fm}$, is a good approximation for most of the nuclei [182]. The parameter c is then determined by demanding, that the charge radius squared

$$\left\langle r^2 \right\rangle = \frac{\int \mathrm{d}r\, r^4 \rho_0(r)}{\int \mathrm{d}r\, r^2 \rho_0(r)}$$

agrees with the values from the literature [165]. Since the potential in Eq. (3.10) is spherically symmetric, the angular part can be separated and the solution with spherical spinors $\Omega_{\kappa m}(\vartheta, \varphi)$ can be written in terms of the spherical spinors from Eqs. (1.18), (1.19) as [42]

$$|n\kappa m\rangle = \frac{1}{r}\begin{pmatrix} G_{n\kappa}(r)\,\Omega_{\kappa m} \\ i\,F_{n\kappa}(r)\,\Omega_{-\kappa m} \end{pmatrix},$$

and the resulting equations for the radial functions are solved with the dual-kinetic-balance method [149] to obtain $G_{n\kappa}$ and $F_{n\kappa}$, and the corresponding eigenenergies numerically.

In Table 3.2, the binding energies for muonic $^{205}_{83}\text{Bi}$, $^{147}_{62}\text{Sm}$, and $^{89}_{40}\text{Zr}$ are shown, where the finite nuclear size effect is illustrated by also including the binding energies $E^{(C)}_{n\kappa}$ from Eq. (1.22) of the pure Coulomb potential $-Z\alpha/r_\mu$, which read [42]

$$E^{(C)}_{n\kappa} = 1 - \left(1 + \frac{(Z\alpha)^2}{\left(n - |\kappa| + \sqrt{\kappa^2 - (Z\alpha)^2}\right)^2}\right)^{-\frac{1}{2}}. \tag{3.12}$$

Furthermore, the corrections from the Uehling potential in Eq. (3.13) are shown separately. The uncertainties include the error in the rms radius value as well as a model error, which is estimated via the difference of the binding energies with the Fermi potential from Eq. (3.11) and the potential of a charged sphere with the same rms radius. For heavy nuclei, the finite nuclear size correction can amount up to $50\,\%$, and thus the binding energy is halved.

3.1.3.2 Vacuum polarization in Uehling approximation

For atomic electrons, there are two QED corrections of the order α, namely the self-energy QED and the vacuum polarization correction [182], which usually are of a similiar size. For muons, however, the vacuum polarization correction is much larger due to virtual electron-positron pairs, which are less suppressed due to their low mass compared to the muon's mass [122]. The spherically symmetric part of the vacuum polarization to first

order in α and $Z\alpha$ is the Uehling potential [143]

$$V_{\text{Uehl}}(r_\mu) = -\alpha \frac{2\alpha}{3\pi} \int_0^\infty \mathrm{d}r' \, 4\pi\rho_0(r') \int_1^\infty \mathrm{d}t \left(1 + \frac{1}{2t^2}\right)$$

$$\times \frac{\sqrt{t^2-1}}{t^2} \frac{\exp(-2m_e|r_\mu - r'|t) - \exp(-2m_e(r_\mu + r')t)}{4m_e r_\mu t}, \qquad (3.13)$$

where m_e is the electron mass and ρ_0 is the spherically symmetric part of the charge distribution from Eq. (3.7). This potential can be directly added to the Dirac equation (3.10). In this way, all iterations of the Uehling potential are included [148]. Results for our calculations can be found in Table 3.2.

3.1.3.3 Recoil corrections

Taking into account the finite mass and the resulting motion of the nucleus leads to recoil corrections to the bound muon energy levels. In nonrelativistic quantum mechanics, as in classical mechanics, the problem of describing two interacting particles can be reduced to a one particle problem by using the reduced mass m_r of the muon-nucleus system [183]. With the mass of the nucleus m_N, the reduced mass reads in the chosen system of units as

$$m_r = \frac{m_N}{m_N + 1}, \qquad (3.14)$$

and the Dirac equation is accordingly modified to

$$\left(\boldsymbol{\alpha} \cdot \mathbf{p} + \beta \, m_r + V_{\text{el}}^{(0)}(r_\mu)\right) |n\kappa m\rangle = (m_r - E_{n\kappa}^{(B)}) |n\kappa m\rangle .$$

In relativistic quantum mechanics, this separation is not possible. We follow an approach used in Refs. [122, 184], which includes the nonrelativistic part of the recoil correction already in the wave functions by using the reduced mass in the Dirac equation and calculating the leading relativistic corrections perturbatively. If $E_{n\kappa}^{(\text{fm})}$ denotes the binding energy of Eq. (3.10) with the finite size potential from Eq. (3.9) but with the reduced mass replaced by the full muon rest mass, and $E_{n\kappa}^{(\text{rm})}$ the binding energy in the same potential but with the reduced mass from Eq. (3.14), then the leading relativistic recoil correction $\Delta E_{n\kappa}^{(\text{rec,rel})}$ according to Ref. [122] reads

$$\Delta E_{n\kappa}^{(\text{rec,rel})} = -\frac{\left(E_{n\kappa}^{(\text{fm})}\right)^2}{2M_N} + \frac{1}{2M_N} \left\langle h(r) + 2E_{n\kappa}^{(\text{fm})} P_1(r) \right\rangle,$$

where M_N is the mass of the nucleus, and the functions $h(r)$ and $P_1(r)$ are defined in Eqs. (109) and (111) of Ref. [122], respectively. In Table 3.3, the binding energies obtained from solving the Dirac equation with the muon rest mass and the reduced mass of the muon-nucleus system are compared, and the leading relativistic recoil correction is shown. The uncertainties include errors in the rms radius, the model of the charge distribution and for the relativistic recoil, and a $(m_\mu/M_N)^2$ term due to higher-order corrections in the mass ratio of muon and nucleus, which dominates the uncertainty for

lower Z.

3.1.3.4 Interaction with atomic electrons

The effect of the surrounding electrons on the binding energies of the muon is commonly refered to as electron screening and was estimated following Ref. [185] by calculating an effective screening potential from the charge distribution of the electrons as

$$V_e(\mathbf{r}_\mu) = -\alpha \int \mathrm{d}V \frac{\rho_e(\mathbf{r})}{|\mathbf{r}_\mu - \mathbf{r}|}, \tag{3.15}$$

and using this potential in the Dirac equation for the muon. The charge distribution of the electrons is obtained by their Dirac wave functions as $\rho_e(\mathbf{r}) = \sum_i \psi_{e_i}^*(\mathbf{r}) \cdot \psi_{e_i}(\mathbf{r})$, where $\psi_{e_i}(\mathbf{r})$ is the four component spinor of the i-th considered electron. In order to obtain the wave functions of the electrons, it has to be taken into account, that the muon essentially screens one unit of charge from the nucleus. The simplest possibility is to replace the nuclear charge by an effective charge $\tilde{Z} = Z - 1$ and then solve the Dirac equation for the electron with this modified nuclear potential. Another possibility is to start solving the Dirac equation for the muon in the nuclear potential without electron screening. Then, the Dirac equation for the electron is solved for all required states, with the screening potential due to the bound muon

$$V_\mu(\mathbf{r}_e) = -\alpha \int \mathrm{d}V \frac{\psi_\mu^*(\mathbf{r}) \cdot \psi_\mu(\mathbf{r})}{|\mathbf{r}_e - \mathbf{r}|},$$

analogously to Eq. (3.15). The interaction between the electrons is not taken into account here. Finally, the Dirac equation for the muon is solved again, now including the nuclear potential and the screening potential (3.15) due the atomic electrons from the considered electron configuration. This procedure can be repeated in the spirit of Hartree's method [186] until the electrons and the muon are self-consistent in the fields of each other, but our studies show that one iteration is usually enough since the overlap of muon and electron wave functions in heavy muonic atoms is small. It is important to note, that here the screening potential depends to a small extent on the state of the muon, since the muon wave function is used in the calculation for the electron wave function. The atomic electrons primarily behave like a charged shell around the muon and the nucleus; thus every muon level is mainly shifted by a constant term, which is not observable in muonic transitions. The correction ΔE_S is defined as the difference of the binding energy without and with screening potential, respectively. Therefore, a positive value indicates that the muon is less bound due to the screening effect. The main contribution to the nonconstant part of the screening potential comes from the $1s$ electrons, since their wave functions have the biggest overlap with the muon; therefore the exact electron configuration has only a minor effect on transition energies [185]. In Table 3.4, results for the screening correction are shown for both mentioned methods and for different electron configurations. Values of the screening correction for different electron configurations show that a 10% error for the non-constant part is a reasonable estimate.

3.1.3.5 Electric quadrupole splitting

Since for heavy nuclei the nuclear radius is comparable to the muon's Compton wavelength [165, 179], the muonic wavefunction overlaps strongly with the nucleus and the muon is sensitive to nuclear shape corrections, which results in hyperfine splitting of the energy levels. The quadrupole part of the electric interaction (3.8) can be rewritten as [160]

$$V_{\text{el}}^{(2)}(\mathbf{r}_\mu, \theta, \phi) = -\alpha \frac{Q_0 F_{\text{QD}}(r_\mu)}{2\, r_\mu^3} \sum_{m=-2}^{2} C_{2m}(\theta, \phi) C_{2m}^*(\vartheta_\mu, \varphi_\mu), \qquad (3.16)$$

where $C_{lm}(\vartheta, \varphi) = \sqrt{4\pi/(2l+1)} Y_{lm}(\vartheta, \varphi)$ and angles with a subscript μ describe the position of the muon in the laboratory frame. Here, the nuclear intrinsic quadrupole moment is defined via the charge distribution from Eq. (3.7) as

$$Q_0 = 2\sqrt{\frac{4\pi}{5}} \int_0^\infty r^4 \rho_2(r)\, \mathrm{d}r,$$

and the distribution of the quadrupole moment is described by the function $F_{\text{QD}}(r_\mu)$, where in the point-like limit $F_{\text{QD}}(r_\mu) = 1$. For the shell model, where the quadrupole distribution is concentrated around the nuclear rms radius R_N, the divergence for $r_\mu = 0$ is removed, and the corresponding quadrupole distribution function is

$$F_{\text{QD}}(r_\mu) = \begin{cases} (r_\mu/R_N)^5 & r_\mu \le R_N \\ 1 & r_\mu > R_N \end{cases}.$$

Formally, this corresponds to a charge distribution with

$$\rho_2(r_\mu) = \frac{Q_0}{2R_N^4} \sqrt{\frac{5}{4\pi}} \delta(r_\mu - R_N).$$

The matrix elements of the quadrupole interaction from Eq. (3.16) in the states (3.6) read [187]

$$\langle FM_F I\kappa | H_E^{(2)} | FM_F I\kappa \rangle = -\alpha(-1)^{j+I+F} \qquad (3.17)$$
$$\times \langle I || \frac{Q_0}{2} \widehat{C}_2(\vartheta_N, \varphi_N) || I \rangle \langle n\kappa || \frac{F_{\text{QD}}(r_\mu)}{r_\mu^3} \widehat{C}_2(\vartheta_\mu, \varphi_\mu) || n\kappa \rangle .$$

The reduced matrix element in the nuclear coordinates can be expressed with the spectroscopic nuclear quadrupole moment Q as

$$\langle I || \frac{Q_0}{2} \widehat{C}_2(\vartheta_N, \varphi_N) || I \rangle = Q \sqrt{\frac{(2I+3)(2I+1)(I+1)}{4I(2I-1)}},$$

and the reduced matrix elements in the muonic coordinates are

$$\langle n\kappa || \, f(r_\mu) \widehat{C}_2(\vartheta_\mu, \varphi_\mu) \, ||n\kappa\rangle = \tag{3.18}$$

$$-\sqrt{\frac{(2j+3)(2j+1)(2j-1)}{16j(j+1)}} \int_0^\infty \left(G_{n\kappa}^2(r_\mu) + F_{n\kappa}^2(r_\mu) \right) \frac{F_{\mathrm{QD}}(r_\mu)}{r_\mu^3} \mathrm{d}r_\mu.$$

The values for the nuclear rms-radii R_N and the spectroscopic quadrupole moments Q are taken from Refs. [165, 188]. In Table 3.5, results for the electric quadrupole hyperfine splitting for the nuclei $^{205}_{83}\mathrm{Bi}$, $^{147}_{62}\mathrm{Sm}$, and $^{89}_{40}\mathrm{Zr}$ are shown for a selection of hyperfine states, with uncertainties stemming from the error in the quadrupole moment and an estimation of the modeling uncertainty.

3.1.3.6 Magnetic dipole splitting

As for the magnetic part, dipole interaction is considered. Therefore, the corresponding interaction Hamiltonian reads [143]

$$H_M = \frac{|e|}{4\pi} \, \boldsymbol{\mu} \cdot \left(F_{\mathrm{BW}}(r) \frac{\mathbf{r}}{r^3} \times \boldsymbol{\alpha} \right), \tag{3.19}$$

with the charge of the muon $e = -|e|$, the nuclear magnetic moment $\boldsymbol{\mu}$, its distribution function F_{BW}, and the Dirac matrices $\boldsymbol{\alpha}$. The difference in the hyperfine splitting between a point-like magnetic moment and a spacial distribution of the magnetization is called the Bohr-Weisskopf effect [189]. In the following, the diagonal matrix elements of the magnetic interaction are analyzed, paying special attention to the distribution function F_{BW}. We expect the contribution of the higher-order terms, namely electric octupole, magnetic quadrupole, and beyond, to be smaller than the uncertainty of the considered terms [123, 190]. Therefore they can be ignored here.

The hyperfine splitting arises from the interaction of the nuclear magnetic moment with the muon's magnetic moment, which is also sensitive to the spatial distribution of the nuclear currents. Since the magnetic moment of the muon is inversely proportional to its mass, the magnetic hyperfine splitting in muonic atoms is less important than in electronic atoms. The matrix elements of the corresponding Hamiltonian (3.19) in the state (3.6) are [187]

$$\langle FM_F I\kappa| \, H_M \, |FM_F I\kappa\rangle = \, [F(F+1) - I(I+1) - j(j+1)] \tag{3.20}$$

$$\times \frac{\alpha}{2m_p} \frac{\mu}{\mu_N} \frac{\kappa}{Ij(j+1)} \int_0^\infty \frac{G_{n\kappa}(r_\mu) F_{n\kappa}(r_\mu) F_{\mathrm{BW}}(r_\mu)}{r_\mu^2} \mathrm{d}r_\mu,$$

where m_p is the proton mass, and the ratio of the observed magnetic moment $\mu :=$ $\langle II| \, (\boldsymbol{\mu})_z \, |II\rangle$ and the nuclear magneton μ_N can be found in the literature [188]. For the simple model of a homogeneous nuclear current, the distribution function of the

Bohr-Weisskopf effect reads

$$F_{\text{BW}}(r_\mu) = \begin{cases} (r_\mu/R_N)^3 & r_\mu \leq R_N \\ 1 & r_\mu > R_N \end{cases}.$$

Furthermore, an additional method is used to obtain the distribution function F_{BW} from the nuclear single particle model, where the nuclear magnetic moment is assigned to the odd nucleon and the Schrödinger equation for this nucleon is solved in the Woods-Saxon potential of the other nucleons [143]. In Table 3.5, results for the magnetic dipole hyperfine splitting for the nuclei $^{205}_{83}\text{Bi}$, $^{147}_{62}\text{Sm}$, and $^{89}_{40}\text{Zr}$ are presented for a selection of hyperfine states, using both methods for obtaining F_{BW}, where the model error is estimated by the difference of these two methods and the uncertainty in the magnetic moment is also taken into account.

3.1.4 Dynamic hyperfine structure

The first order calculation of the electric hyperfine structure due to the quadrupole interaction in heavy muonic atoms is not sufficient for the prediction of the level structure. There are two reasons for this:

Firstly, the fine-structure splitting between states of the same parity, especially between the $2p1/2$ and $2p3/2$ states, is on the energy scale of a few hundred keV. This can be seen for the example of ^{205}Bi in Table 3.2. On the other hand, the first order energy correction due to the electric quadrupole interaction for ^{205}Bi is also more than 100 keV in the $2p3/2$ states, as seen in Table 3.5. Note that the expectation value of the quadrupole interaction in the $2p1/2$ states vanishes because of angular momentum selection rules. The quadrupole interaction is a rank 2 tensor operator, thus the sum of the involved angular momenta must also be larger than or equal to 2. This is not the case for the expectation value in the $2p1/2$ states with $j = 1/2$. There are, however, also the non-diagonal matrix elements with one $2p1/2$ and one $2p3/2$ states, which are also on the hundred keV states for high Z muonic atoms. If the quadrupole hyperfine structure is only calculated in first order perturbation theory, these non-diagonal elements are not considered. Since the separation between the two unperturbed states ($2p1/2$ and $2p3/2$) is on the same level as the non-diagonal matrix elements, first order perturbation theory is not enough. As a consequence, the non-diagonal matrix elements have to be taken into account. One possibility would be using higher order perturbation theory, which involves a sum over the complete muonic spectrum. However, already the consideration of the non-diagonal matrix elements for a muonic fine-structure doublet can explain the majority of the higher order effects. Therefore, the formalism of quasi-degenerate perturbation theory [191] is useful, and the general approach will be briefly reviewed in the following Section. Here, the quadrupole interaction is rediagonalized in finite-dimensional subspaces only using a small number of muonic states.

Secondly, the energy scale of the fine structure and electric quadrupole splitting on the order of hundred keV or more is on the same scale as the typical excitation energy of the excited nuclear states in the rotational ground state band. In addition, the nuclear states in the ground state rotational band have the same parity and thus are coupled by the

quadrupole interaction. This means, the expectation value of the quadrupole operator is generally non-zero, also for the case of different nuclear rotational states. As a consequence, the excited nuclear states have to be taken into account when rediagonalizing the quadrupole interaction in finite-dimensional subspaces as discussed above.

3.1.4.1 Quasi-degenerate perturbation theory

In this Section, the general approach to quasi-degenerate perturbation theory is briefly reviewed, following [122, 191], before it is applied to muonic atoms in the following sections. For simplicity, a system with unperturbed eigenstates $|n\rangle$ and corresponding unperturbed energies $\mathcal{E}_n$ is investigated with the unperturbed eigenvalue equation

$$H_0 |n\rangle = \mathcal{E}_n |n\rangle \,,$$

where H_0 is the unperturbed Hamiltonian. The connection to the muonic atom case can be made by considering $|n\rangle$ as a multi-index for all the quantum numbers F, M, I, K, n, κ, m of the muonic atom and using the quadrupole interaction for the perturbation H_1. The perturbed eigenvalue equation reads

$$(H_0 + H_1) |a\rangle = E_a |a\rangle \,. \tag{3.21}$$

If m different states $|n_i\rangle$ are almost degenerate, which means their energy separation is on the same order as the first order correction due to H_1, the corresponding modelspace is defined as all $|n_i\rangle$ with $i \in \{1, ..., m\}$, if necessary the states have to be relabeled, such that the lowest indices correspond to the states defining the model space. The projector P on the modelspace is defined by acting on an eigenstate $|a\rangle = \sum_n a_n |n\rangle$ of Eq. (3.21) as

$$\mathrm{P} |a\rangle = \sum_{i=1}^{m} a_i |n_i\rangle \,,$$

thus keeping only the coefficients for states inside the modelspace. Analogously, the projector Q is defined as the complement, i.e. keeping only coefficients of states outside of the modelspace. Thereby, it holds that $\mathrm{P} + \mathrm{Q} = \mathbb{1}$ and the following relations [122] can be derived for eigenstates of the total Hamiltonian from Eq. (3.21):

$$\mathrm{Q} |a\rangle = -(H_0 - E_a)^{-1} \mathrm{Q} H_1 |a\rangle$$
$$(H_0 - E_a + \mathrm{P} H_1) \mathrm{P} |a\rangle = -\mathrm{P} H_1 \mathrm{Q} |a\rangle \,.$$

Combining these two equations results in

$$\mathrm{P} \left((H_0 - E_a + H_1) \mathrm{P} |a\rangle - H_1 (H_0 - E_a)^{-1} \mathrm{Q} H_1 |a\rangle \right) = 0, \tag{3.22}$$

which can be expanded in Q. Thereby, states outside of the finite dimensional modelspace can be considered systematically. The zero-order term is obtained by neglecting the term containing a Q operator:

$$\mathrm{P} \left(H_0 + H_1 - E_a \right) \mathrm{P} |a\rangle = 0. \tag{3.23}$$

This is essentially Eq. (3.21), but projected onto the modelspace. As expected, to zeroth order the states outside of the modelspace can be neglected. Since this is a finite dimensional system, this corresponds to constructing the Hamiltonian matrix and diagonalizing it.

Applied to muonic atoms, the unperturbed Hamiltonian is the sum of rigid rotor Hamiltonian for the nucleus and Dirac Hamiltonian with the monopole potential for the muon, and the perturbation is the hyperfine (mainly quadrupole) interaction. Then a modelspace needs to be chosen, for example the first few nuclear rotational states and a muonic fine-structure doublet like the $(2p3/2, 2p1/2)$ or $(3d5/2, 3d3/2)$ states. Finally the diagonal and non-diagonal matrix elements of the hyperfine interactions need to be calculated for all states in the modelspace and the matrix representation of the total Hamiltonian in the modelspace needs to be diagonalized.

The solution of Eq. (3.23) results in an approximation for the eigenstates of the full Hamiltonian as

$$\left|a^{(0)}\right\rangle = \sum_{i=1}^{m} a_i^{(0)} \left|n_i\right\rangle, \tag{3.24}$$

which is a linear combination of the unperturbed states forming the modelspace with the coefficients obtained from the diagonalization of the Hamiltonian matrix. The corresponding eigenvalues are the approximations $E_a^{(0)}$ of the eigenenergy.

For the leading order corrections due to the operator Q, Eq. (3.22) is used, including the Q-dependent term, however, only the effect on the modelspace is investigated, corresponding to the approximation $|a\rangle \approx P |a\rangle$. Using the property of a projection operator $P^2 = P$, Eq. (3.22) can be written as

$$\underbrace{P(H_0 + H_1 - E_a)P}_{\tilde{H}_0} + \underbrace{P(H_1(E_a - H_0)^{-1}QH_1)P}_{\tilde{H}_1} |a\rangle = 0,$$

which takes the form of an eigenvalue problem with the unperturbed Hamiltonian $\tilde{H}_0$ and the perturbation $\tilde{H}_1$. Because of P on the left and right side, this is a finite dimensional problem, although each matrix element of $\tilde{H}_1$ involves a summation over the complete spectrum, as shown below. The unperturbed solutions are already known from Eq. (3.24), thereby the energy correction due to the perturbation $\tilde{H}_1$ can be calculated within first order perturbation theory as

$$E_a^{(1)} = \left\langle a^{(0)} \left| \tilde{H}_1 \right| a^{(0)} \right\rangle \tag{3.25}$$

$$= \sum_{k>m} \frac{\left\langle a^{(0)} \left| H_1 \right| n_k \right\rangle \left\langle n_k \left| H_1 \right| a^{(0)} \right\rangle}{E_a^{(0)} - \mathcal{E}_{n_k}}$$

$$= \sum_{i,j=1}^{m} a_i^{(0)*} a_j^{(0)} \sum_{k>m} \frac{\langle n_i|H_1|n_k\rangle \langle n_k|H_1|n_j\rangle}{E_a^{(0)} - \mathcal{E}_{n_k}},$$

where the projector on states outside of the modelspace is formally written as $Q = \sum_{k>m} |n_k\rangle \langle n_k|$. If there are continuous parts in the spectrum, this sum also involves

integrals. Once the zero order energies and states are found by diagonalizing the Hamiltionian in the modelspace, the first order energy correction due to states outside of the modelspace is calculated by calculating the second order energy correction due to the original perturbation H_1, but the intermediate sum only involves states not contained in the modelspace, i.e. not already considered in the diagonalization. As a result, the sum $E_a = E_a^{(0)} + E_a^{(1)}$ contains a complete second order treatment of the perturbation H_1, and additionally the contributions of the states in the modelspace to all orders.

For actual calculations in the context of muonic atoms, these calculations are very time-consuming for the following reasons: Already the unperturbed Hamiltonian involves a numerical solution of the Dirac equation with an extended nuclear monopole potential. The diagonal and non-diagonal matrix elements of the electric quadrupole interaction have to be calculated via numerical integrations as well, before diagonalizing the total Hamiltonian. Since finite basis set methods [149] are used in this thesis for solving the Dirac equation, a numerical, discrete representation of the complete muonic spectrum is obtained. Therefore, in the framework of this thesis, numerical evaluations of Eq. (3.25) without approximations is possible.

In the following Sections, the approach of quasi-degenerate perturbation theory from Section 3.1.4.1 will be applied to muonic atoms considering electric monopole and quadrupole interaction, as well as magnetic dipole interaction. The starting point is a given deformed nuclear charge distribution $\rho(\mathbf{r})$ and a distribution of the static currents $\mathbf{j}(\mathbf{r})$ inside the nucleus. The necessary steps are the following:

- Definition of the unperturbed and perturbed Hamiltonian,

- Calculation of the potentials starting from the given charge and current distribution,

- Solving the spherical Dirac equation,

- Definition of modelspaces,

- Calculation of diagonal and non-diagonal matrix elements of the, perturbation in the modelspace and rediagonalization,

- Calculation of energy correction due to states outside of the modelspace.

3.1.4.2 Non-diagonal elements of hyperfine interactions

The unperturbed Hamiltonian for describing the muonic atom are already given for the nuclear part in Eq. (3.4) and for the muonic part in Eq. (3.5) in terms of the nuclear charge distribution $\rho(\mathbf{r})$. The corresponding states of define total angular momentum F are given in Eq. (3.6). The next step for calculating the hyperfine structure of muonic atoms in the framework of quasi-degenerate perturbation theory is the calculation of the diagonal and non-diagonal matrix elements of the electric quadrupole and magnetic dipole interactions.

For expressing the electric quadrupole interaction in terms of the charge distribution $\rho(\mathbf{r})$ including the non-diagonal matrix elements, the starting point is the multipole expansion of the electric potential from Eq. (3.3). The quadrupole terms with $l = 2$ is

$$V_{\text{el}}^{(2)}(\mathbf{r}_\mu, \phi, \theta) = -Z\alpha \left[\int \mathrm{d}^3\mathbf{r}'_N \frac{r_<^2}{r_>^3} \mathrm{P}_2(\cos\vartheta'_N)\rho(\mathbf{r}'_N) \right] \sum_{m=-2}^{2} \mathrm{C}_{2m}^*(\theta, \phi)\mathrm{C}_{2m}(\vartheta_\mu, \varphi_\mu). \quad (3.26)$$

As a next step, the matrix element of (3.26) with two arbitrary states from Eq. (3.6) is considered, which reads as

$$\Delta E^{(2)} = \left\langle F_1 M_1\, I_1 K\, n_1\kappa_1 \middle| V_{\text{el}}^{(2)} \middle| F_2 M_2\, I_2 K\, n_2\kappa_2 \right\rangle. \quad (3.27)$$

Keeping in mind that $\mathrm{C}_{lm}^*(\vartheta, \varphi) = (-1)^m \mathrm{C}_{l\,(-m)}(\vartheta, \varphi)$, and that the normalized spherical harmonic are irreducible tensor operators as introduced in Appendix C, the sum in Eq. (3.26) is a scaler product of two rank-2 irreducible tensors. Therefore, Eq. (C.5) can be used for expressing the matrix element from Eq. (3.27) in terms of the reduced matrix elements of the spherical harmonics as

$$\Delta E^{(2)} = - Z\alpha\delta_{F_1 F_2}\delta_{M_1 M_2}(-1)^{F+I_2+j(\kappa_1)} \begin{Bmatrix} I_1 & I_2 & 2 \\ j(\kappa_2) & j(\kappa_1) & F \end{Bmatrix} \langle I_1 K || \mathrm{C}_2 || I_2 K \rangle$$

$$\times \left\langle n_1\kappa_1 \middle\| \mathrm{C}_2 \int \mathrm{d}^3\mathbf{r}'_N \frac{r_<^2}{r_>^3}\mathrm{P}_2(\cos\vartheta'_N)\rho(\mathbf{r}'_N) \middle\| n_2\kappa_2 \right\rangle, \quad (3.28)$$

where it is useful to define

$$f_Q(r_\mu)/r_\mu^3 := \int \mathrm{d}^3\mathbf{r}'_N \frac{r_<^2}{r_>^3}\mathrm{P}_2(\cos\vartheta'_N)\rho(\mathbf{r}'_N), \quad (3.29)$$

since for the approximation of a point-like quadrupole moment or in general for large r_μ it holds that $f_Q(r_\mu) = 1$, and thus the usual r_μ^{-3} radial integral for quadrupole hyperfine structure is recovered. Accordingly, $f_Q(r_\mu)$ describes the finite distribution of the quadrupole moment inside the nucleus. The reduced matrix element in the nuclear coordinates can be calculated using the rigid rotor wave functions from Appendix D and the definition of the reduce matrix element from Eq. (C.2). It is given in Eq. (D.3) and reads as

$$\langle I_1 K || \mathrm{C}_l || I_2 K \rangle = (-1)^{I_2+K}\sqrt{(2I_1+1)(2I_2+1)} \begin{pmatrix} I_1 & I_2 & l \\ -K & K & 0 \end{pmatrix}.$$

The reduced matrix elements in the muonic variables can be evaluated as [181]

$$\langle n_1\kappa_1||f(r_\mu)C_l(\vartheta_\mu,\varphi_\mu)||n_2\kappa_2\rangle = (-1)^{j(\kappa_1)+1/2}\sqrt{(2j(\kappa_1)+1)(2j(\kappa_2)+1)}$$

$$\times \begin{pmatrix} j(\kappa_1) & j(\kappa_2) & l \\ -\frac{1}{2} & \frac{1}{2} & 0 \end{pmatrix}\pi(l(\kappa_1)+l(\kappa_2))\int \mathrm{d}r r^2(g_{n_1\kappa_1}(r)g_{n_2\kappa_2}(r)+f_{n_1\kappa_1}(r)f_{n_2\kappa_2}(r))f(r_\mu),$$

where $f_{n\kappa}(r_\mu)$ and $g_{n\kappa}(r_\mu)$ are the radial wave function (1.20) obtained by solving the Dirac equation (3.4). The function

$$\pi(x) = \begin{cases} 1\,, \text{x even;} \\ 0\,, \text{otherwise} \end{cases} \tag{3.30}$$

is needed for parity selection rules. Thus, the evaluation of one reduced muonic matrix element requires one numerical integration, and for every calculation of $f_Q(r_\mu)$ therein, a numerical integration of Eq. (3.29) has to be performed.

For the magnetic dipole interaction, the diagonal matrix elements have been given by Eq. (3.20). In the following, it will be extended to non-diagonal matrix elements in the framework of the rigid roton nuclear model, following the analysis in [190]. The magnetic Hamiltonian due to the vector potential $\mathbf{A}_N$ caused by the nuclear static currents reads in the nuclear body fixed frame as

$$\mathrm{H}_M(\mathbf{r}_\mu) = |e|\,\boldsymbol{\alpha}\cdot\mathbf{A}_N(\mathbf{r}_\mu),$$

where the vector potential is generated by the static currents in the nucleus, and the connection reads [162]

$$\mathbf{A}_N(\mathbf{r}_\mu) = \frac{1}{4\pi}\int \mathrm{d}^3\mathbf{r}'\,\frac{\mathbf{j}(\mathbf{r}')}{|\mathbf{r}_\mu - \mathbf{r}'|}.$$

For extended nuclei, i.e. without a divergence in the origin, the current distribution can be expressed in terms of the curl of another vector field, since the divergence of the current distribution in the static case is zero [162]. This field is called magnetization $\mathbf{M}(\mathbf{r})$, and the connection between current distribution and magnetization is

$$\mathbf{j}(\mathbf{r}) = \boldsymbol{\nabla} \times \mathbf{M}(\mathbf{r}).$$

The restriction to magnetic dipole interactions is done by writing the magnetization as

$$\mathbf{M}(\mathbf{r}) = \boldsymbol{\mu}f(r) = |\boldsymbol{\mu}|\mathbf{e}'_z\,f(r),$$

where $\boldsymbol{\mu}$ is the nuclear magnetic dipole operator and the second equality follows from the fact, that the symmetric rigid rotor model is used and the magnetic moment has to be aligned with the nuclear body fixed z-axis $\mathbf{e}'_z$ for not violating axial symmetry. In Cartesian coordinates in the laboratory system, the basis vector $\mathbf{e}'_z$ of the body fixed

system reads as

$$\boldsymbol{\mu}(\theta, \phi) = |\boldsymbol{\mu}| \begin{pmatrix} \sin\theta\cos\phi \\ \sin\theta\sin\phi \\ \cos\theta \end{pmatrix}. \tag{3.31}$$

The scalar function $f(r)$ describes the finite distribution of the dipole moment in the nucleus, which is responsible for the Bohr-Weisskopf effect [189] and is normalized by

$$4\pi \int_0^\infty \mathrm{d}r\, r^2\, f(r) = 1.$$

Thereby, the magnetic Hamiltonian can be written as

$$\mathrm{H}_M(\mathbf{r}_\mu, \theta, \phi) = \frac{|e|}{4\pi}\boldsymbol{\mu}(\theta, \phi) \cdot \left(F_{\mathrm{BW}}(r)\frac{\mathbf{r}}{r^3} \times \boldsymbol{\alpha}\right), \tag{3.32}$$

which agrees with Eq. (3.19), and the function $F_{\mathrm{BW}}(r)$ is connected to the distribution function $f(r)$ as

$$F_{\mathrm{BW}}(r) = -4\pi r^2 \partial_r \left(\int_0^\infty \mathrm{d}r' \frac{r'^2 f(r')}{\max(r, r')}\right).$$

The magnetic dipole Hamiltonien from Eq. (3.32) can be written as a scalar product of two rank-1 irreducible tensor operator acting on the muonic and nuclear coordinates, respectively, as [181]

$$\mathrm{H}_M(\mathbf{r}_\mu, \theta, \phi) = \sum_{\lambda=-1}^{1} (-1)^\lambda\, t_\lambda(\mathbf{r}_\mu)\ \mu_{-\lambda}(\theta, \phi),$$

$$t_\lambda(\mathbf{r}_\mu) = \frac{-i\sqrt{2}|e|}{4\pi}\left(\boldsymbol{\alpha} \cdot \mathbf{C}_{1\lambda}^{(0)}(\vartheta_\mu, \varphi_\mu)\right)\frac{F_{\mathrm{BW}}(r_\mu)}{r_\mu^2},$$

where $\mathbf{C}_{bc}^{(a)}(\vartheta, \varphi)$ are the vector spherical harmonics [150, Section 7.], and μ_λ with $\lambda \in \{-1, 0, 1\}$ the spherical components [150, Section 1.] of the magnetic moment operator from Eq. (3.31). Correspondingly, Eq. (C.5) can be used for the calculation of expectation values, and the result is

$$\langle F_1 M_1\, I_1 K\, n_1\kappa_1 | \mathrm{H}_M | F_2 M_2\, I_2 K\, n_2\kappa_2 \rangle = \delta_{F_1 F_2}\delta_{M_1 M_2}(-1)^{F_1 + j(\kappa_2) + I_1}$$

$$\times \begin{Bmatrix} j(\kappa_1) & j(\kappa_2) & 1 \\ I_2 & I_1 & F_1 \end{Bmatrix} \langle n_1\kappa_1 || t || n_2\kappa_2 \rangle\, \langle I_1 K || \mu || I_2 K \rangle.$$

The reduced matrix elements of the nuclear magnetic moment operator can be obtained by using literature values of the magnetic moment from [188] and using Eq. (D.3) and the relation

$$\langle I K || \mu || I K \rangle = |\mu|\, \langle I K || C_1 || I K \rangle.$$

The reduced muonic matrix elements can be evaluated to [181]

$$\langle n_1\kappa_1||t||n_2\kappa_2\rangle = -\frac{|e|}{4\pi}(\kappa_1 + \kappa_2)(-1)^{j(\kappa_1)+1/2}\sqrt{(2j(\kappa_1)+1)+(2j(\kappa_2)+1)}$$

$$\times \begin{pmatrix} j(\kappa_1) & j(\kappa_2) & 1 \\ -1/2 & 1/2 & 0 \end{pmatrix} \pi(l(-\kappa_1)+l(\kappa_2)+1)\int_0^\infty \mathrm{d}r F_{\mathrm{BW}}(r)\,(f_{n_1\kappa_1}g_{n_2\kappa_2}+f_{n_2\kappa_2}g_{n_1\kappa_1})\,.$$

3.1.4.3 Rediagonalization of muonic fine-structure doublets

The concept of rediagonalization in the context of quasi-degenerate perturbation theory was introduced in Section 3.1.4.1. The unperturbed Hamiltonian is introduced in Eqs. (3.4) and (3.5) for the unperturbed states from Eq. (3.6). The matrix elements necessary for the rediagonalization of the hyperfine states are discussed in Section 3.1.4.2 in the general case. Thereby, all necessary ingredients for the rediagonalization in the dynamic hyperfine structure of muonic atoms is available. In this Section, the concept is applied to a simplified part of the muonic ^{185}Re spectrum for clarification. The ^{185}Re nucleus has a ground state angular momentum of 5/2 [188], and in this Section, the first two excited nuclear states with angular momentum quantum numbers of 7/2 and 9/2 are considered. As for the muonic states, the $2p$ fine-structure doublet is considered, these are the $2p{1/2}$ and $2p{3/2}$ states. As a first step, it has to be considered, which unperturbed states $|FMIK\,n\kappa\rangle$ can be formed by the nuclear and muonic states. In general, for every possible value of F, the projection quantum number $M \in \{-F,...,F\}$. The maximal value for F is $F_{\max} = \max(j(\kappa)+I)_{\kappa,I\in M}$. The minimal value for F is $F_{\min} = \min(|j(\kappa)-I|)_{\kappa,I\in M}$. In this example, the values are $F_{\max} = 6$ and $F_{\min} = 1$. As a next step, it has to be checked for every value of F, which combinations of muonic and nuclear states of the modelspace are able to form the F value. For this, the triangle equation $|j(\kappa)-I| \leq F \leq j(\kappa)+I$ has to hold. In this way, a modelspace is separated into distinct blocks, each with a value of F and a corresponding subset of states from the modelspace, which can form this F value. Since the hyperfine interactions are diagonal in F and M, the rediagonalization has to be performed only in the block separately, not in the entire modelspace. The separation of the modelspace into the different blocks is shown in Fig. 3.2. For the experimental nuclear excitation energies from [169] and the RMS radius from [165], the resulting level scheme without and with rediagonalized quadrupole interaction is shown in Fig. 3.3, which demonstrates the rich level structure in this case. Furthermore, there is no clear distinction between the fine- and hyperfine structure, since the nuclear rotational states, the fine-structure splitting and the quadrupole matrix elements are all on the same energy scale. In practice, for the calculations is Sec. 3.3, up to five excited nuclear states are used, which leads to even more energy levels.

After the rediagonalization, the unperturbed states $|FMIK\,n\kappa\rangle$ are mixed. The quantum numbers F and M, describing the total angular momentum of the muon-nucleus system are still well-defined, since the hyperfine structure is diagonal therein. However, different I, κ, and in principle also n are mixed by the rediagonalization, and a mixed
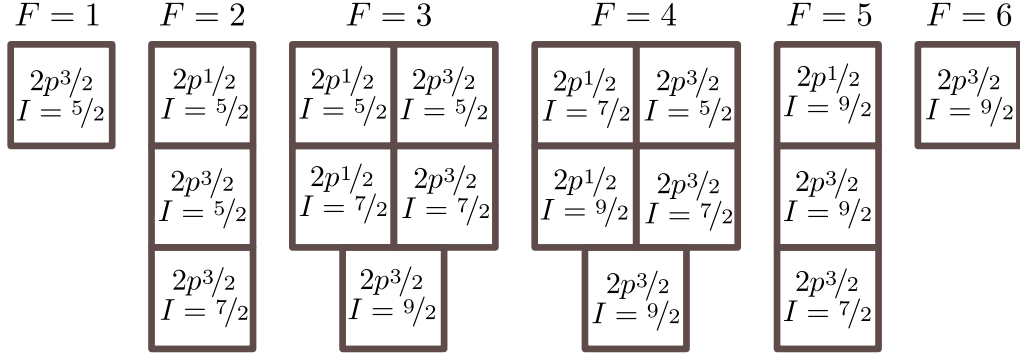
Figure 3.2: Separation of the modelspace consisting of the muonic $2p1/2$ and $2p3/2$ states coupled to the nuclear states with angular momentum 5/2, 7/2, and 9/2. For every possible value of $F \in \{1,...,6\}$, the states are shown, which are involved in the rediagonalization of the hyperfine interaction.

state are written as

$$|FM, i\rangle = \sum_{k=1}^{d} \alpha_k^{(i)} |FM \, I_k K \, n_k \kappa_k\rangle, \tag{3.33}$$

where $i \in \{1,...,d\}$ and d is the number of states in the modelspace, which can form the total angular momentum F. For the example of rhenium in this Section, there is one state for $F \in \{1,6\}$; three states for $F \in \{2,5\}$; and five states for $F \in \{3,4\}$ (see Fig. 3.2). Thus, e.g. for $F = 3$, a 5x5-matrix has to be rediagonalized, and the coefficient-matrix $\alpha_k^{(i)}$ in Eq. (3.33) corresponds to the matrix of corresponding eigenvectors.

3.1.5 Transition probabilities and intensities

It has been shown in Sec. 3.1.4 that the coupling of muonic states and nuclear rotational states in connection with a strong quadrupole interaction leads to a rich and complicated level structure without a clear distinction of fine- and hyperfine structure. As a result, there is a large number of potential transitions between the states. For example, if the L x rays are considered, i.e. the transitions from the $3d$ fine-structure doublet to the $2p$ fine-structure doublet, there are only four transitions if the hyperfine structure is not considered. One of these transitions is suppressed because it is not an electric dipole transition. On the other hand, due to the dynamic hyperfine structure, there could be in principle hundreds of L x rays, many of them electric dipole type. As a consequence, for the comparison with experimental spectra, not only the level structure is needed, but also the corresponding relative intensities. In experimental spectra, the intensity of a transition is proportional to the number of measured photons with the energy of the transition. The intensities are a product of two quantities: Firstly, the intensity is proportional to the transition probability, which can be calculated in principle, as soon as the wave functions and corresponding energies are known. In this thesis, the transition probabilities are calculated relativistically and without the long-wavelength approximation. Secondly, the intensities are proportional to the population of the initial state. However, for calculating the population of the initial states, all transitions to the initial state from

Figure 3.3: Level scheme of the muonic $2p1/2$ and $2p3/2$ states coupled to the nuclear $5/2$, $7/2$, and $9/2$ states in ^{185}Re. Zero energy corresponds to the free, resting muon and the nuclear ground state. Through the nuclear rotational states and the strong quadrupole interaction, there is no clear distinction between fine- and hyperfine structure, which results in a rich structure of the energy levels.

even higher states have to be considered. This eventually leads to a cascade calculation for the muon, where the muon is initially in a highly excited state and drops towards the ground state step-by-step by radiative transitions. In the following the transition probabilities and the the population and cascade calculations are discussed separately.

As a first step, the transition probabilities due to spontaneous emission of a photon in a muonic transition are analyzed in this paragraph. Starting point is the general formula for the Einstein coefficient (transition probability per time) for state with defined total angular momentum from an initial state $|F_i M_i, i_i\rangle$ to a final state $|F_f M_f, i_f\rangle$, where the states, in which the hyperfine structure is diagonalized, are defined in Eq. (3.33). Following [181, Section 6.], this expression reads as

$$A_J^{(\lambda)} = \frac{2\alpha(2J+1)(J+1)}{J}\Delta E \sum_{M,M_i,M_f} \left|\left\langle F_f M_f, i_f \left| \hat{t}_{JM}^{(\lambda)} \right| F_i M_f, i_i \right\rangle\right|^2. \qquad (3.34)$$

Here, ΔE is the energy difference of the initial and final state, J is the total angular momentum of the photon and $\lambda = 1$ corresponds to an electric transition, whereas $\lambda = 0$ stands for a magnetic transition. The multipole transition operator $\hat{t}_{JM}^{(\lambda)}$ is defined in Eqs. (6.120), (6.121), (6.128),(6.129) of [181] in terms of the multipole components of the

54

multipole potential $\mathbf{a}_{JM}^{(\lambda)}$ and of the scalar potential Φ_{JM} as

$$\boldsymbol{\alpha} \cdot \mathbf{a}_{JM}^{(\lambda)}(\mathbf{r}_\mu) - \Phi_{JM}(\mathbf{r}_\mu) = i\sqrt{\frac{(2J+1)(J+1)}{4\pi J}}\hat{t}_{JM}^{(\lambda)}(\mathbf{r}_\mu).$$

Using Eq. (3.33) for the definition of the mixed states is terms of the unperturbed states $|FM\,IK\,n\kappa\rangle$, the matrix elements are written as

$$\left\langle F_f M_f, i_f \left| \hat{t}_{JM}^{(\lambda)} \right| F_i M_f, i_i \right\rangle = \sum_{k_i, k_f} \alpha_{k_f}^{(i_f)*} \alpha_{k_i}^{(i_i)} \left\langle F_f M_f\, I_{k_f} K\, n_{k_f}\kappa_{k_f} \left| \hat{t}_{JM}^{(\lambda)} \right| F_i M_i\, I_{k_i} K\, n_{k_i}\kappa_{k_i} \right\rangle.$$

Since muonic transitions are considered in this section, it acts on the muonic coordinates $\mathbf{r}_\mu$, which is one subsystem of the composite states in Eq. (3.34) with total angular momentum F_i and F_f, respectively. Since the multipole transition operator is an irreducible tensor operator of rank J, Eq. (C.6) can be used for calculating the matrix elements. This results in the following expression for the matrix elements:

$$\left\langle F_f M_f\, I_{k_f} K\, n_{k_f}\kappa_{k_f} \left| \hat{t}_{JM}^{(\lambda)} \right| F_i M_i\, I_{k_i} K\, n_{k_i}\kappa_{k_i} \right\rangle = \delta_{I_{k_f} I_{k_i}} (-1)^{F_i + j(\kappa_{k_f}) + I_{k_i} - J}$$

$$\times \sqrt{2F_i + 1}\, \mathrm{C}_{F_i M_i\, JM}^{F_f M_f} \begin{Bmatrix} j(\kappa_{k_i}) & j(\kappa_{k_f}) & J \\ F_f & F_i & I_{k_i} \end{Bmatrix} \left\langle n_{k_f}\kappa_{k_f} \left|\left| \hat{t}_J^{(\lambda)} \right|\right| n_{k_i}\kappa_{k_i} \right\rangle. \quad (3.35)$$

The Clebsch-Gordan coefficients in Eq. (3.35) do not depend on the summation indices k_i and k_f, and the only dependency on the projection numbers M, M_f, and M_i are as arguments of the Clebsch-Gordan coefficients. Therefore, the summation over M, M_f, M_i only affects the Clebsch-Gordan coefficient and the sum rule [150]

$$\sum_{M, M_i, M_f} \left(C_{F_i M_i\, JM}^{F_f M_f} \right)^2 = 2F_f + 1$$

can be used to simplify the calculation of Eq. (3.34) considerably. The reduced matrix elements in the muonic variables in Eq.(3.35) can be evaluated in length gauge as [181]

$$\left\langle n_f\kappa_f \left|\left| \hat{t}_J^{(1)} \right|\right| n_i\kappa_i \right\rangle = \langle n_f\kappa_f ||C_J|| n_i\kappa_i\rangle \quad (3.36)$$

$$\times \int dr \Big\{ j_J(\Delta E\, r) \left[G_{n_f\kappa_f}(r)G_{n_i\kappa_i}(r) + F_{n_i\kappa_i}(r)F_{n_f\kappa_f}(r) \right]$$

$$+ j_J(\Delta E\, r) \Big[\frac{\kappa_i - \kappa_f}{J+1} \left(G_{n_f\kappa_f}(r)F_{n_i\kappa_i}(r) + G_{n_i\kappa_i}(r)F_{n_f\kappa_f}(r) \right)$$

$$+ \left(G_{n_i\kappa_i}(r)F_{n_f\kappa_f}(r) - G_{n_f\kappa_f}(r)F_{n_i\kappa_i}(r) \right) \Big] \Big\}$$

for electric transitions with $\lambda = 1$ and as

$$\left\langle n_f\kappa_f \left|\left| \hat{t}_J^{(0)} \right|\right| n_i\kappa_i \right\rangle = \langle n_f\,(-\kappa_f) ||C_J|| n_i\kappa_i\rangle$$

$$\times \int dr \frac{\kappa_i + \kappa_f}{J+1} j_J(\Delta E\, r) \left[-G_{n_f\kappa_f}(r)F_{n_i\kappa_i}(r) - F_{n_f\kappa_f}(r)G_{n_i\kappa_i}(r) \right]$$

for magnetic transitions with $\lambda = 0$. $j_J(x)$ are the spherical Bessel functions [192, Eq. 10.47.3]. The reduced matrix elements of the normalized spherical harmonics $\mathrm{C}_{JM}(\vartheta, \varphi)$ read as [181]

$$
\langle n_f \kappa_f || C_J || n_i \kappa_i \rangle = (-1)^{j(\kappa_f)+1/2} \sqrt{(2j(\kappa_i)+1)(2j(\kappa_f)+1)} \begin{pmatrix} j(\kappa_f) & j(\kappa_i) & J \\ -1/2 & 1/2 & 0 \end{pmatrix}
$$
$$
\times \pi(l(\kappa_f) + l(\kappa_i) + J), \tag{3.37}
$$

where the function $\pi(x)$ is defined in Eq. (3.30). The angular momentum selection rules are implemented in the 6j- and 3j-symbols and in the function $\pi(x)$ in Eqs. (3.35) and (3.37). For electric dipole transitions with $J = 1$ and $\lambda = 1$, the following selection rules have to be fulfilled:

$$
\begin{aligned}
j(\kappa_i) &= j(\kappa_f) & &\text{or } j(\kappa_i) = j(\kappa_f) \pm 1; \\
F_i &= F_f & &\text{or } \quad F_i = F_j \pm 1; \\
l(\kappa_i) &= l(\kappa_f) \pm 1. & &
\end{aligned} \tag{3.38}
$$

The relativistic expression for the electric transitions in Eq. (3.36) can be simplified in the non-relativistic, long-wavelenth approximation. The non-relativstic approximation means that the lower component of the radial spinors $F_{n\kappa}(r)$ is small, and therefore mixed terms $F_{n_1\kappa_1}(r)G_{n_2\kappa_2}(r)$ can be neglected. The term $\sim F_{n\kappa}(r)^2$ is kept for convenience, since $G_{n\kappa}(r)^2 + F_{n\kappa}(r)^2$ corresponds to the probability density. The long-wavelength approximation means, that $\Delta E\, r$ is small, and therefore the corresponding spherical Bessel function can be expanded. The spherical Bessel functions can be approximated as

$$
j_J(x) \approx \frac{x^J}{(2J+1)!!},
$$

where the double factorial is evaluated as $y!! = y \cdot (y-2) \cdot (y-4) \cdot \ldots$. Thereby, Eq. (3.36) becomes

$$
\left\langle n_f \kappa_f \left|\left| \hat{t}_J^{(1)} \right|\right| n_i \kappa_i \right\rangle = \langle n_f \kappa_f || C_J || n_i \kappa_i \rangle
$$
$$
\times \frac{\Delta E^J}{(2J+1)!!} \int \mathrm{d}r\, r^J \left(G_{n_f\kappa_f}(r)G_{n_i\kappa_i}(r) + F_{n_i\kappa_i}(r)F_{n_f\kappa_f}(r) \right),
$$

and the corresponding transition probabilities per time from Eq. (3.34) thereby have the typical dependence $\sim \Delta E^{2J+1}$.

After the transition probabilities have been discussed in the last paragraph, the remaining issue of the population of the initial states is discussed in the following. The transition probabilities can be calculated ab initio, independent from experimental details. This is not the case for the population. Here, details of the experimental setup and the capture process have to be considered. Muonic atoms are typically created by shooting a slow muon beem on a target, which contains the isotope of interest [122–124]. The statistical population of the muonic states after the muon has been captured by

the nucleus depends on the state of the incoming muon as well as details of the nuclear target. Additionally, for highly excited states, the muon and the atomic electrons are not well separated, as described in Sec. 3.1.3.4, thus the muon-electron interaction has to be taken into account and e.g. Auger transitions can occur [193]. In heavy nuclei, this leads to a complicated many-body problem. Then, even if an initial population of the low-lying muonic states, where the electron-muon interaction can be neglected, would be known in form of the diagonal elements of the muonic density matrix, the master equation using transition probabilities as described in the previous paragraph has to be solved [193]. Due to the large number of energy levels in the dynamic hyperfine structure and the calculation of the transition probabilities with Eq. (3.34), this is still a very time-consuming calculation.

However, the cascade calculation can be simplified considerable. In experiments, muons typically tend to be captured in circular orbits, these are states with maximal angular momentum $l=n-1$. Additionally, the fastest transitions are electric dipole transitions of the muon, which change the orbital angular momentum quantum number of the muon by one. The most intense sequence of transitions are correspondingly the $5g \rightarrow 4f \rightarrow 3d \rightarrow 2p \rightarrow 1s$ transitions. Especially the $2p \rightarrow 1s$ (K x rays) and $3d \rightarrow 2p$ (L x rays) spectra have been used in the past to obtain information about nuclear structure from experiments with muonic atoms, e.g. in [112, 116–119, 194, 195]. Under the assumption, that the muon starts in a circular orbit and than cascades by electric dipole transitions, the calculation of the intensities is considerably simplified, using the selection rules from Eq. (3.38), since now the $2p$ state can be only populated by the $3d$ states, which can only be populated by the $4f$ states and so on, and this approach will be used also in this thesis. This means, the population of a state in the, say, $2p$ states can be obtained by summing up all intensities of the transitions from the $3d$ states to this state. Finally, only the initial population of the initial states with the highest n (eg. $6h$, $5g$, $4f$) needs to be given. Here, a simple statistical population has proved to describe experiments correctly [194], where every coupled muon-nucleus state with total angular momentum F has a relative population $\sim (2F + 1)$, corresponding to the different M values. Furthermore, initially the nucleus is in its ground state, since the excitation of nuclear rotational levels only occurs during the muonic cascade, when energy is transfered from the muon to the nucleus. The muonic cascade starting from the muonic $4f$ states is visualized in Fig. 3.4. In practice, the calculation of the spectrum begins with the diagonalization the hyperfine interaction in the fine structure doublets of the states with circular orbits ($2p$,$3d$,$4f$). Then, assuming a relative transition proportional to $2F + 1$ in the fine-structure doublet with the highest quantum number $n = n_{\max}$, all transitions to the next states with $n_{\max-1}$ are calculated. The relative population of the $n_{\max-1}$ states is obtained by summing up the intensities of all transitions to this state. This procedure can be repeated until the muonic ground state is reached, and thereby all line-intensities are obtained. A statistical population $\sim 2F + 1$ in the higher states leads to a statistical population in the lower states, as long as the hyperfine-structure splitting can be neglected. In states with $n > 3$, the hyperfine-structure splitting is typically small. Therefore, statistically populated $6h$ states lead to (almost) statistically populated $5g$, which in turn (almost) result in statistically populated $4f$ states. Thereby, the line intensities are insensitive on the starting point of the cascade. The calculation of transition

μ Z

$\dfrac{4f\frac{7}{2}}{4f\frac{5}{2}} \otimes \underline{I_{nucl}} = I_0$ M

$\dfrac{3d\frac{5}{2}}{3d\frac{3}{2}} \otimes \dfrac{\overline{\cdots}}{\underline{I_{nucl}} = I_0 + 1} \quad L$
$\quad\quad\quad\quad \underline{I_{nucl}} = I_0$

$\dfrac{2p\frac{3}{2}}{2p\frac{1}{2}} \otimes \dfrac{\overline{\cdots}}{\underline{I_{nucl}} = I_0 + 1} \quad K$
$\quad\quad\quad\quad \underline{I_{nucl}} = I_0$

$1s\frac{1}{2} \otimes \dfrac{\overline{\cdots}}{\underline{I_{nucl}} = I_0 + 1}$
$\quad\quad\quad \underline{I_{nucl}} = I_0$
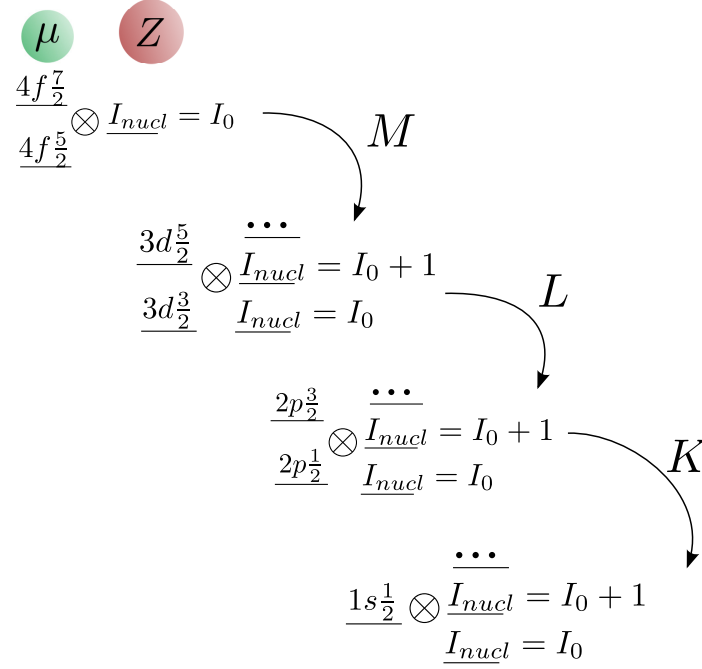
Figure 3.4: Visualization of the muonic cascade, starting from the muonic $4f$ states and the nucleus in its ground state. Then, the muon is cascading towards its ground state through the $3d$ and $2p$ states. Here, excited nuclear rotational states can be populated. The population of a state in the $3d$ modelspace is obtained by summing up all transitions from the $4f$ states to this state, and analogously for the $2p$ states. For a given initial population of the $4f$ states, in this way all intensities can be calculated.

probabilities is used in Sec. 3.3 for analyzing the spectrum of muonic Rhenim-185.

3.2 Higher order corrections for the dynamic hyperfine structure

In this Section, improved calculations of two higher order contributions to the dynamic hyperfine structure are discussed. Firstly, corrections of the quadrupole matrix elements due to vacuum polarization (VP) are considered. Furthermore, a numerical treatment of second order quadrupole interactions is presented.

The contribution of leading order VP to the spherically symmetric part of the charge distribution was briefly discussed in Sec. 3.1.3.2. However, VP influences multipole interactions of all orders, thus in the context of the dynamic hyperfine structure it influences matrix elements of the quadrupole interaction between muon and nucleus. Until now, the corresponding correction to the matrix elements has at most been considered with a power-series expansion [113, 196] or for specific forms of the nuclear charge distribution [197], which does not enable precision calculations for heavy muonic atoms. In this thesis, a new approach is developed in Section 3.2.1 by performing a multipole expansion of the Uehling potential. This enables the calculation of the leading order VP correction to the quadrupole matrix elements for arbitrary charge distributions with all finite size effects.

The approach of quasi-degenerate perturbation theory is discussed in Sec. 3.1.4.1, and the rediagonalization of the perturbation is applied to the hyperfine interaction in Sec. 3.1.4.2 and 3.1.4.3. However, there are residual second order corrections due to contributions from outside of the modelspace, as introduced in Eq. (3.25). A non-relativistic estimation of the residual second order electric quadrupole interaction with states outside of this modelspace has been presented in Ref. [198]. In this thesis, an extended, fully relativistic approach is presented in Sec. 3.2.2.

3.2.1 Quadrupole-Uehling interactions

The resummation of the order $\alpha(Z\alpha)$ vacuum polarization (Uehling potential) has been discussed in Section 1.1.1, with the result that it can be included in the solution of the Dirac equation. The starting point in this Section is the renormalized expression for the Uehling potential for a given, deformed nuclear charge distribution, which reads in the chosen system of units (Appendix A) as [142]

$$V_{\text{uehl}}(\mathbf{r}'_\mu) = -Z\alpha \frac{2\alpha}{3\pi} \int \mathrm{d}^3\mathbf{r}'_N \frac{\rho(\mathbf{r}'_N)}{|\mathbf{r}'_\mu - \mathbf{r}'_N|} K_1(2m_e|\mathbf{r}'_\mu - \mathbf{r}'_N|), \qquad (3.39)$$

where m_e is the electron mass, and primed coordinates belong to the body-fixed nuclear system, as defined in 3.1.2. $K_1(x)$ belongs to the family of functions

$$K_n(x) = \int_1^\infty \mathrm{d}t\, \mathrm{e}^{-xt} \left(\frac{1}{t^3} + \frac{1}{2t^5} \right) \sqrt{t^2 - 1}\, t^n.$$

The functions $K_n(x)$ are related for different n by

$$
\begin{aligned}
K_n(x) &= -\partial_x K_{n-1}(y), \\
K_{n-1}(x) &= -\int^x \mathrm{d}y\, K_n(y).
\end{aligned}
\tag{3.40}
$$

Furthermore, they can be expressed in terms of Meijer G functions from Eq. (B.2) as

$$
K_n(x) = \frac{1}{4}G_{1,3}^{3,0}\left(\frac{x^2}{4}\middle|\begin{array}{c}-\frac{n}{2}+2\\-\frac{n}{2}+\frac{1}{2},0,\frac{1}{2}\end{array}\right) + \frac{1}{8}G_{1,3}^{3,0}\left(\frac{x^2}{4}\middle|\begin{array}{c}-\frac{n}{2}+3\\-\frac{n}{2}+\frac{3}{2},0,\frac{1}{2}\end{array}\right),
\tag{3.41}
$$

which enables evaluation using arbitrary precision implementations of the Meijer G function of existing libraries or programs like [199,200]. The Uehling potential (3.39) depends only on $|\mathbf{r}'_\mu - \mathbf{r}'_N|$, similar to the electric potential (3.3), which can be written as

$$
|\mathbf{r}'_\mu - \mathbf{r}'_N| = |\mathbf{r}_\mu - \mathbf{r}_N| = \sqrt{r_\mu^2 + r_N^2 - 2r_\mu r_N y},
$$

and therefore only depends on the absolute values of the vectors and on $y = \cos(\sphericalangle \mathbf{r}_\mu \mathbf{r}_N)$. The dependence on $|\mathbf{r}'_\mu - \mathbf{r}'_N|$ is more complicated for the Uehling potential, but a multipole expansion can be performed nonetheless by expanding the dependence on y in Legendre polynomials, which reads as

$$
\begin{aligned}
\frac{K_1(2m_e|\mathbf{r}'_\mu - \mathbf{r}'|)}{|\mathbf{r}'_\mu - \mathbf{r}'|} &= \sum_{l=0}^{\infty} c_l(r_\mu, r_N) P_l(y) \\
&= \sum_{l=0}^{\infty} c_l(r_\mu, r_N) \sum_{m=-l}^{l} \mathrm{C}_{lm}^*(\vartheta'_N, \varphi'_N) \mathrm{C}_{lm}(\vartheta'_\mu, \varphi'_\mu),
\end{aligned}
$$

where the second equality is a consequence of the addition theorem (B.8) of Legendre polynomials. The expansion coefficients are still functions of the absolute values of the vectors and are defined as

$$
c_l(r_\mu, r_N) = \frac{2l+1}{2}\int_{-1}^{1}\mathrm{d}y\,\frac{K_1(2m_e|\mathbf{r}_\mu - \mathbf{r}_N|)}{|\mathbf{r}_\mu - \mathbf{r}_N|}P_l(y).
\tag{3.42}
$$

Eq. (3.42) can be either solved by numerical integration, or expressed in closed form, using Eq. (3.41) for the functions $K_n(x)$. For the closed form expression, the integration variable y in Eq. (3.42) is substituted by $z = f^{-1}(y) = 2m_e|\mathbf{r}_\mu - \mathbf{r}_N|$ or $y = f(z) = (r_\mu^2 + r_N^2 - (z/2m)^2)/(2r_\mu r_N)$. Thereby, Eq. (3.42) reads as

$$
c_l(r_\mu, r_N) = \frac{2l+1}{4r_\mu r_N m_e}\int\limits_{2m_e|r_\mu - r_N|}^{2m_e(r_\mu + r_N)}\mathrm{d}z\,K_1(z)P_l(f(z)).
\tag{3.43}
$$

Since $f(z)$ is quadratic in z, it follows that $P_l(f(z))$ is a polynomial of degree $2l$. Thereby, Eq.(3.43) can be integrated by part $2l$-times for the two functions $K_1(z)$ and $P_l(f(z))$,

using the relations from Eq. (3.40), to solve the integral as

$$c_l(r_\mu, r_N) = \frac{2l+1}{4r_\mu r_N m_e} \sum_{i=0}^{2l} K_{-i}(z)\, \partial_y^{(i)} P_l(f(z)) \Big|_{y=2m_e(r_\mu+r_N)}^{y=2m_e|r_\mu-r_N|}.$$

Thereby, the Uehling potential can be written, analogously to the electric potential, as

$$V_{\text{uehl}}(\mathbf{r}_\mu, \phi, \theta) = \sum_{l=0}^{\infty} -Z\alpha \frac{2\alpha}{3\pi} \int d^3 r_N'\, c_l(r_\mu, r_N) P_l(\cos\vartheta_N') \rho(\mathbf{r}_N') \sum_{m=-l}^{l} C_{lm}^*(\theta, \phi) C_{lm}(\vartheta_\mu, \varphi_\mu).$$

$$=: \sum_{l=0}^{\infty} Q_{\text{uehl}}^{(l)}(r_\mu) \sum_{m=-l}^{l} C_{lm}^*(\theta, \phi) C_{lm}(\vartheta_\mu, \varphi_\mu)$$

$$=: \sum_{l=0}^{\infty} V_{\text{uehl}}^{(l)}(\mathbf{r}_\mu, \phi, \theta). \tag{3.44}$$

For $l = 0$, the expression for Uehling potential of a spherical charge distribution [142] which only depends on r_μ is recovered as

$$V_{\text{uehl}}^{(0)}(r_\mu) = -\frac{2\alpha(Z\alpha)}{3m_e r} \int_0^\infty dr'\, \rho_0(r') \left[K_0(2m_e|r - r'|) - K_0(2m_e(r + r')) \right], \tag{3.45}$$

where the spherically averaged part of the charge distribution is

$$\rho_0(r) = \frac{1}{4\pi} \int_0^{2\pi} d\varphi \int_0^\pi d\vartheta \sin(\vartheta) \rho(\mathbf{r}).$$

The approach is applicable for arbitrary charge distributions, and is applied for the quadrupole term with $l = 2$ in Sec. 3.3. In the following, the quadrupole term $l = 2$ is considered for the models of a charged-shell and point-like quadrupole distribution, where the corresponding term in Eq. (3.44) can be simplified. For the charged-shell quadrupole distribution, the nuclear charge distribution is written as

$$\rho(\mathbf{r}_N) \qquad = \rho_0(r_N) + \rho_2(r_N, \vartheta_N)$$

$$\rho_2(r_N, \vartheta_N) = -\alpha Q_0 \frac{5}{8\pi} \frac{\delta(r - R)}{R^4} P_2(\cos\vartheta_N),$$

where the intrinsic quadrupole moment Q_0 is concentrated at the nuclear radius R. Thereby, the quadrupole part of the Uehling potential (3.44) reads

$$V_{\text{uehl}}^{(2)}(\mathbf{r}_\mu, \phi, \theta) = -\alpha Q_0 \frac{\alpha}{3\pi} \frac{c_2(r_\mu, R)}{R^2} \sum_{m=-l}^{l} C_{lm}^*(\theta, \phi) C_{lm}(\vartheta_\mu, \varphi_\mu). \tag{3.46}$$

The limit of a point-like quadrupole moment is the limit of zero nuclear radius R in Eq. (3.46). However, the limit cannot be calculated naively due to the R^2 factor in the denominator, but it turns out that the Taylor expansion of $c_2(r_\mu, R)$ around $R = 0$ has
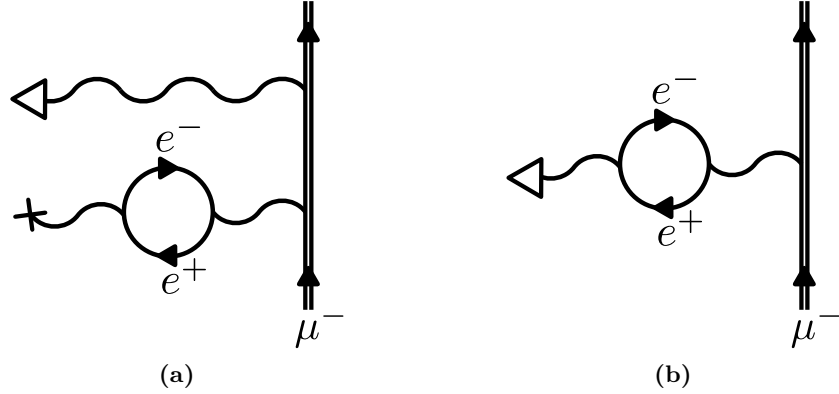
Figure 3.5: Feynman diagrams for the leading order contributions of the vacuum polarization to the quadrupole interaction in muonic atoms. An external double line stands for the bound-muon wave function. A single internal line for the free electron propagator, and a wave line for the photon propagator. A cross represents the interaction with the monopole potential, and a triangle the interaction with the quadrupole potential. Contribution (a) is calculated by including the spherically symmetric contribution of the Uehling potential (3.45) in the Dirac equation; Contribution (b) by including the quadrupole contribution of the Uehling potential (3.44) in the matrix elements.

no constant and linear term. Therefore, $c_2(r_\mu, R)$ can be expanded for small R as

$$c_2(r_\mu, R) = \frac{K_1(2m_e r_\mu) + 2m_e r_\mu K_2(2m_e r_\mu) + 4m_e^2 r_\mu^2/3 K_3(2m_e r_\mu)}{r^3} R^2 + \mathcal{O}(R^3),$$

and therby the point-like limit of quadrupole Uehling potential reads

$$V_{\text{uehl}}^{(2)}(\mathbf{r}_\mu, \phi, \theta) = -\alpha Q_0\, g(r) \sum_{m=-l}^{l} C_{lm}^*(\theta, \phi) C_{lm}(\vartheta_\mu, \varphi_\mu). \tag{3.47}$$

$$g(r) = \frac{\alpha}{3\pi} \frac{K_1(2m_e r_\mu) + 2m_e r_\mu K_2(2m_e r_\mu) + 4m_e^2 r_\mu^2/3 K_3(2m_e r_\mu)}{r^3}.$$

The expressions for the quadrupole Uehling potential for the charged-sphere and point-like distributions from Eqs. (3.46), (3.47), respectively, can be used for testing the implementation of the general case in Eq. (3.44).

3.2.2 Residual second order corrections

The rediagonalization of the hyperfine interaction in muonic atoms is explained in Section 3.1.4, using a modelspace consisting of a muonic fine-structure doublet and the first rotational nuclear states. Also, the leading contribution from states outside of the modelspace is derived in Eq. (3.25). Essentially, it is the second order energy correction due to the hyperfine interaction, excluding all states which are considered in the rediagonalization process. In the following, the residual second order corrections will be discussed

for the example of the rhenium $2p$ modelspace given in Sec. 3.1.4.3. Here, the modelspace consists of the muonic $2p1/2$ and $2p3/2$ states and the nuclear $5/2, 7/2, 9/2$ states. This results in 18 coupled states, with values of the total angular momentum $F = 1, ..., 6$, as shown in Fig. 3.2. The set of these states is called M_μ. The summation over all states, which are not in the modelspace involves all states $|FM I_i K_i\, n_i\kappa_i\rangle$ as defined in Eq. (3.6), where not all quantum numbers coincide with a state in the considered modelspace M_{2p}. In the following, this summation is schematically written as $\sum_{i\notin M_\mu}$.

After the subspace has been chosen and rediagonalization has been performed, the quadrupole interaction with states outside of the subspace leads to residual second order corrections to the energy levels [198]. For the total second order correction a summation/integration over the complete (discrete and continous) spectrum for both nuclear and muonic states has to be performed. For the complete nuclear spectrum, sophisticated models or numerous experimental data are required. However, the muon is a point-like particle and can be described as a Dirac particle. Therefore, in this work, we calculate the second order corrections due to the electric quadrupole (Eq. (3.26)) and quadrupole-Uehling interaction (l=2-term in Eq. (3.44)), where the nucleus stays in the rotational ground state, but the complete muonic spectrum is considered. For a composite state from Eq. (3.33), where the hyperfine interaction is diagonalized in the modelspace, the second order energy shift due to states outside of the modelspace is

$$\Delta E_{2.\text{ord.}}^{(F,k)} = \sum_{i\notin M_\mu} \frac{\left|\langle FMk|\, V_{\text{el}}^{(2)}+V_{\text{uehl}}^{(2)}\,|FMn_i\kappa_i I_i K\rangle\right|^2}{E_{F,k} - E_i}, \tag{3.48}$$

where the sum is to be taken over all states not considered in the rediagonalization, including continuum states of the muon, and the unperturbed energy of the state i is $E_i = E_{n_i\kappa_i} + E_{I_i}$.

3.2.3 Evaluation for ^{185}Re & ^{235}U

Calculations of the quadrupole-Uehling potential and the residual second order corrections have been performed for muonic rhenium and uranium, assuming a deformed Fermi nuclear charge distribution which reads as

$$\rho_{ca\beta}(\vec{r}) = \frac{N}{1 + \exp\left(\frac{r-c(1+\beta Y_{20}(\vartheta))}{a}\right)},$$

where c is the half-density radius, a the skin thickness, β the deformation parameter, and N a normalization constant determined by the condition

$$\int \mathrm{d}^3r\, \rho_{ca\beta}(\vec{r}) = 1.$$

Using the deformed Fermi distribution has proved to be suitable for the description of the level structure of heavy muonic atoms, e.g. [112, 117, 118]. Values for the parameters can be estimated by using a value a=2.3 fm/(4 ln 3), which has proved to be a sufficiently accurate value for most nuclei [182]. Then, c and β are chosen such that the quadrupole

moment and RMS value of the distribution are in agreement with the literature values
from [165, 188]. For the nuclear states involved in the dynamic hyperfine structure,
also the excitation energies are needed from literature [169]. The used parameters are
summarized in Table 3.6. With these parameters, the electric and Uehling potentials,
both monopole and quadrupole parts, can be calculated numerically. The muon wave
functions are obtained by solving the Dirac equation (3.4) with the dual-kinetic-balance
method [149]. Thereby, a complete set of muonic bound and continuum states is obtained.
An overview for the binding energies of muon states important for the dynamic hyperfine
splitting are shown in Table 3.7.

The quadrupole matrix elements can be calculated both for the rediagonalization in
the dynamic hyperfine structure and for the evaluation of the residual second-order terms
(3.48), using Eq. (3.28). As the next step, the total Hamiltonian (3.1) is diagonalized in
finite subspaces or modelspaces consisting of the muonic $(2p1/2, 2p3/2)$ or $(3d3/2, 3d5/2)$
doublet states and nuclear ground state rotational band. For rhenium, the first six states
with $I_N = 5/2, ..., 15/2$ are considered, and for uranium with $I_N = 7/2, ..., 17/2$. The
excitation energies of the nuclear states are summarized, along with other nuclear pa-
rameters, in Table 3.6. Thereby, the composite states and corresponding energies E_{quad}
from Eq. (3.33) are obtained and finally, for each of these states the residual second
order quadrupole correction (3.48) is calculated. Here, the intermediate sum goes over
the rotational nuclear and muonic states not included in the modelspace. For the muonic
ground state, a rediagonalization is not necessary, since the diagonal matrix elements of
the quadrupole interactions vanish for muonic states with $j = 1/2$. The quadrupole-
Uehling contribution to the binding energies can be obtained as the difference of two
calculations; once with the matrix elements both for the rediagonalization and for the
residual second-order corrections containing both the electric and Uehling interaction
$V_{\text{el}}^{(2)} + V_{\text{uehl}}^{(2)}$ and a second time only with the electric part $V_{\text{el}}^{(2)}$ from Eq.(3.28). Results for
the residual second order quadrupole correction from Eq. (3.48) and for the quadrupole-
Uehling corrections can be found in Table 3.8 for a number of states.

To conclude, the improved calculation of the higher order effects, the quadrupole in-
teraction in the framework of the dynamic hyperfine structure in heavy muonic atoms
was analyzed by a fully relativistic treatment of the quadrupole-Uehling potential and of
the residual second order terms. The quadrupole-Uehling interaction was obtained rig-
orously by a multipole expansion of the Uehling potential for an arbitrary nuclear charge
distribution. Since it has the same angular structure as the conventional quadrupole
interaction, the quadrupole-Uehling expectation value also vanishes between two muonic
states with $j = 1/2$, thus it does not affect the muonic ground state. The calculations
for uranium show that it can lead to energy corrections almost on the keV level for very
heavy nuclei with muonic $2p$ states and thus can be potentially visible in the current ex-
periments. Being a short-ranged potential, it falls of quickly for states further away from
the nucleus. For states with $n \geq 3$, we find values below $0.15\,\text{keV}$, even for high Z. The
generalization to Uehling corrections for higher-order multipoles is straight forward. In
the case of muonic atoms, since the influence of higher order multipoles is already small,
this correction can be expected to be negligible. The residual second order quadrupole

corrections in the dynamic hyperfine structure were calculated numerically using a basis of relativistic wave functions including nuclear finite size correction and monopole Uehling correction. In contrast to the first order terms, the muonic ground state energy is affected by the second order corrections. Here, the energy correction amounts up to several keV. Also for muonic $2p$ states, it is of similar size. For the $3d$ levels, we find the energy corrections below half a keV, both for rhenium and uranium. If a more advanced nuclear model instead the rotational model is used, the additional nuclear states appear as intermediate state in the second order corrections, leading to the nuclear polarization corrections. Therefore, the approach presented in this work provides an excellent basis for an accurate treatment of the muonic spectrum for the nuclear polarization effect in deformed muonic atoms.

Table 3.2: Overview of the binding energies for muonic $^{205}_{83}$Bi, $^{147}_{62}$Sm, and $^{89}_{40}$Zr, obtained by solving the Dirac equation with the spherically symmetric parts of the muon-nucleus interaction. E_c are the binding energies (3.12) for a point-like nucleus. E_{fs}, E_{uehl} are the binding energies in the finite-size potential with and without the Uehling correction, respectively. The reduced mass is used to include the non-relativistic recoil corrections from Section 3.1.3.3. All energies are in keV.

	state	E_C	E_{fs}	E_{uehl}
^{205}Bi	1s1/2	21573.3	10699.(51.)	10767.(52.)
	2s1/2	5538.6	3654.(15.)	3674.(15.)
	2p1/2	5538.6	4893.(3.)	4927.(3.)
	2p3/2	4958.9	4706.(5.)	4737.(5.)
	3s1/2	2394.3	1796.(5.)	1804.(6.)
	3p1/2	2394.3	2170.0(5)	2190.1(5)
	3p3/2	2221.4	2131.(1.)	2141.(1.)
	3d3/2	2221.4	2216.9(3)	2227.8(3)
	3d5/2	2174.6	2172.8(2)	2183.0(2)
^{147}Sm	1s1/2	11423.8	7165.(28.)	7213.(29.)
	2s1/2	2895.7	2230.(7.)	2242.(7.)
	2p1/2	2895.7	2778.(2.)	2795.(2.)
	2p3/2	2736.9	2689.(2.)	2706.(2.)
	3s1/2	1268.9	1061.(2.)	1066.(2.)
	3p1/2	1268.9	1228.6(4)	1234.2(4)
	3p3/2	1221.7	1204.7(6)	1210.0(6)
	3d3/2	1221.7	1221.4(1)	1226.2(1)
	3d5/2	1207.6	1207.4	1212.1
^{89}Zr	1s1/2	4595.5	3643.(8.)	3669.(8.)
	2s1/2	1155.2	1021.(2.)	1026.(2.)
	2p1/2	1155.2	1147.8(2)	1153.7(2)
	2p3/2	1129.9	1127.0(2)	1132.6(2)
	3s1/2	510.6	469.8(5)	471.4(5)
	3p1/2	510.6	508.0(1)	509.8(1)
	3p3/2	503.1	502.0(1)	503.8(1)
	3d3/2	503.1	503.1	504.5
	3d5/2	500.7	500.7	502.1

Table 3.3: Relativistic recoil corrections to the binding energies of the muon. fm (full mass) denotes the finite size binding energy, analogous to the fourth column of Table 3.2, but with the rest mass of the muon used in the Dirac equation. $\Delta E_{\text{rec,nr}}$ is the non-relativistic recoil correction, which is the difference between the finite size Dirac solutions with reduced mass and full mass, respectively. $\Delta E_{n\kappa}^{(\text{rec,rel})}$ is the leading relativistic recoil correction from Section 3.1.3.3. All energies are in keV.

	state	$E^{(\text{fm})}$	$\Delta E^{\text{rec,nr}}$	$\Delta E_{n\kappa}^{(\text{rec,rel})}1$
^{205}Bi	1s$1/2$	10702.(51.)	-2.80(4)	0.39(4)
	2s$1/2$	3656.(15.)	-1.42(2)	0.09(3)
	2p$1/2$	4895.6(3.0)	-2.24(1)	0.12(3)
	2p$3/2$	4708.2(4.6)	-2.27(1)	0.01(1)
	3s$1/2$	1796.6(5.5)	-0.78(1)	0.03(3)
	3p$1/2$	2180.0(0.5)	-1.05	0.03(3)
	3p$3/2$	2131.9(1.3)	-1.06	0.03(3)
	3d$3/2$	2218.1(0.3)	-1.21	0.02(2)
	3d$5/2$	2174.0(0.2)	-1.19	0.02(2)
^{147}Sm	1s$1/2$	7168.(28.)	-3.17(4)	0.29(7)
	2s$1/2$	2231.1(6.7)	-1.31(1)	0.05(5)
	2p$1/2$	2779.4(1.5)	-1.97(1)	0.05(5)
	2p$3/2$	2691.2(1.8)	-1.96(1)	0.04(4)
	3s$1/2$	1062.0(2.3)	-0.68(1)	0.02(2)
	3p$1/2$	1229.5(0.4)	-0.89	0.01(1)
	3p$3/2$	1205.6(0.6)	-0.89	0.01(1)
	3d$3/2$	1222.3(0.1)	-0.93	0.01(1)
	3d$5/2$	1208.3	-0.92	0.01(1)
^{89}Zr	1s$1/2$	3646.5(8.2)	-3.36(3)	0.15(15)
	2s$1/2$	1022.4(1.5)	-1.11(1)	0.02(2)
	2p$1/2$	1149.2(0.2)	-1.43	0.01(1)
	2p$3/2$	1128.4(0.2)	-1.41	0.01(1)
	3s$1/2$	470.3(0.5)	-0.54	0.01(1)
	3p$1/2$	508.6(0.1)	-0.64	0.00
	3p$3/2$	502.7(0.1)	-0.63	0.00
	3d$3/2$	503.7	-0.64	0.00
	3d$5/2$	501.3	-0.63	0.00

Table 3.4: Electron screening corrections ΔE_{S} to the bound muon energy levels. The subscript 'eff' are the screening corrections with the effective nuclear charge method, whereas '3step' use the 3 step calculation, both described in Section 3.1.3.4. For the superscript (1), only the 1s electrons are considered, while for (1+2), all electrons from with $n = 1, 2$ are considered. All energies are in keV.

	μ-state	$\Delta E_{\mathrm{S,eff}}^{(1)}$	$\Delta E_{\mathrm{S,eff}}^{(1+2)}$	$\Delta E_{\mathrm{S,3step}}^{(1)}$	$\Delta E_{\mathrm{S,3step}}^{(1+2)}$
^{205}Bi	1s1/2	5.555	10.825	5.555	10.825
	2s1/2	5.537	10.803	5.538	10.805
	2p1/2	5.548	10.817	5.549	10.818
	2p3/2	5.547	10.816	5.548	10.817
	3s1/2	5.490	10.748	5.494	10.753
	3p1/2	5.514	10.776	5.516	10.779
	3p3/2	5.512	10.774	5.515	10.777
	3d3/2	5.526	10.791	5.528	10.793
	3d5/2	5.525	10.789	5.527	10.792
^{147}Sm	1s1/2	3.705	7.312	3.705	7.312
	2s1/2	3.699	7.305	3.700	7.305
	2p1/2	3.703	7.309	3.703	7.309
	2p3/2	3.703	7.309	3.703	7.309
	3s1/2	3.682	7.285	3.683	7.286
	3p1/2	3.689	7.293	3.691	7.295
	3p3/2	3.689	7.293	3.690	7.294
	3d3/2	3.694	7.299	3.695	7.300
	3d5/2	3.694	7.298	3.694	7.299
^{89}Zr	1s1/2	2.214	4.405	2.214	4.405
	2s1/2	2.212	4.402	2.212	4.403
	2p1/2	2.213	4.403	2.213	4.403
	2p3/2	2.213	4.403	2.213	4.403
	3s1/2	2.205	4.395	2.206	4.396
	3p1/2	2.207	4.397	2.208	4.398
	3p3/2	2.207	4.397	2.208	4.398
	3d3/2	2.209	4.399	2.210	4.400
	3d5/2	2.209	4.399	2.209	4.400

Table 3.5: Results for the electric quadrupole and magnetic dipole hyperfine splitting for a selection of hyperfine states of muonic $^{205}_{83}$Bi ($I = \frac{9}{2}$), $^{147}_{62}$Sm ($I = \frac{7}{2}$), and $^{89}_{40}$Zr ($I = \frac{9}{2}$). ΔE_Q are the values of the electric quadrupole splitting. $\Delta E_M^{\mathrm{hom}}$ is the magnetic dipole splitting from Eq. (3.20) using a homogeneous nuclear current distribution and ΔE_M^{sp} using the nuclear magnetization distribution in the single particle model. See Sections 3.1.3.5 and 3.1.3.6 for definitions. All energies are in keV.

nucleus	state	ΔE_Q		$\Delta E_M^{\mathrm{hom}}$		ΔE_M^{sp}	
		$F = I - \frac{1}{2}$	$F = I + \frac{1}{2}$	$F = I - \frac{1}{2}$	$F = I + \frac{1}{2}$	$F = I - \frac{1}{2}$	$F = I + \frac{1}{2}$
^{205}Bi	1s1/2	0	0	-2.27(20)	1.86(16)	-2.41(20)	1.97(16)
	2s1/2	0	0	-0.43(5)	0.35(4)	-0.47(6)	0.38(4)
	2p1/2	0	0	-1.23(11)	1.01(9)	-1.31(11)	1.07(10)
	2p3/2	-175.(24.)	175.(24.)	-0.55(2)	0.010(4)	-0.554(22)	0.098(4)
	3s1/2	0	0	-0.144(20)	0.118(16)	-0.160(20)	0.131(16)
	3p1/2	0	0	-0.311(33)	0.255(26)	-0.336(33)	0.275(27)
	3p3/2	-48.9(8.0)	48.9(8.0)	-0.160(7)	0.028(1)	-0.163(7)	0.029(1)
	3d3/2	-25.4(1.3)	25.4(1.3)	-0.161(6)	0.028(1)	-0.163(6)	0.029(1)
	3d5/2	28.3(1.3)	-28.3(1.3)	-0.103(3)	-0.027	-0.103(3)	-0.027
^{147}Sm	1s1/2	0	0	0.42(18)	-0.33(14)	0.25(17)	-0.20(14)
	2s1/2	0	0	0.072(39)	-0.056(30)	0.033(39)	-0.026(30)
	2p1/2	0	0	0.164(58)	-0.127(45)	0.106(58)	-0.082(45)
	2p3/2	-32.8(3.2)	32.8(3.2)	0.066(8)	-0.004(1)	0.058(8)	-0.004(1)
	3s1/2	0	0	0.023(13)	-0.018(10)	0.010(13)	-0.008(8)
	3p1/2	0	0	0.044(18)	-0.034(14)	0.026(18)	-0.02(1)
	3p3/2	-9.4(1.1)	9.4(1.1)	0.020(3)	-0.001	0.017(3)	-0.001
	3d3/2	-3.2(0.1)	3.2(0.1)	0.015(1)	0.000	0.014(1)	0.000
	3d5/2	3.7(0.2)	-3.7(0.2)	0.010	0.004	0.010	0.004
^{89}Zr	1s1/2	0	0	0.36(13)	-0.29(10)	0.23(12)	-0.19(10)
	2s1/2	0	0	0.053(23)	-0.043(18)	0.030(23)	-0.025(18)
	2p1/2	0	0	0.071(14)	-0.058(11)	0.057(14)	-0.047(11)
	2p3/2	12.2(4.7)	-12.2(4.7)	0.023(1)	-0.004	0.022(1)	-0.004
	3s1/2	0	0	0.016(7)	-0.013(6)	0.009(7)	-0.007(6)
	3p1/2	0	0	0.020(4)	-0.017(4)	0.016(4)	-0.013(4)
	3p3/2	3.6(1.4)	-3.6(1.4)	0.007	-0.001	0.007	-0.001
	3d3/2	0.9(0.3)	-0.9(0.3)	0.004	0.000	0.004	0.000
	3d5/2	-1.1(0.4)	1.1(0.4)	0.003	0.000	0.003	0.000

Table 3.6: Nuclear parameters used in the numerical calculations. I_0 is the nuclear ground state angular momentum. RMS and Q_{spec} are the nuclear RMS radius and spectroscopic quadrupole moment of the nuclear ground state from [165, 188], respectively. c, a, β are the parameters of the deformed Fermi distribution derived from RMS and Q_{spec}. E_I are the excitation energies of the nuclear rotational states with angular momentum I, the values are taken from [169].

		$^{185}_{75}\mathrm{Re}$	$^{235}_{92}\mathrm{U}$
I_0		5/2	7/2
RMS	[fm]	5.3596(172)	5.8337(41)
Q_{spec}	[b]	2.21(4)	4.936(6)
c	[fm]	6.3517	6.9562
a	[fm]	0.5234	0.5234
β		0.2322	0.2711
E_{I_0+1}	[keV]	125.3587(9)	46.108(8)
E_{I_0+2}	[keV]	284.2(3)	103.903(8)
E_{I_0+3}	[keV]	475.7(4)	171.464(13)
E_{I_0+4}	[keV]	697.1(5)	250.014(21)
E_{I_0+5}	[keV]	949.7(5)	339.976(24)

Table 3.7: Binding energies of the low-lying, unperturbed muonic states due to the spherically symmetric parts of the electric and Uehling potential obtained by solving Eq. (3.4) for muonic rhenium and uranium. E_{c} shows the binding energies for a point-like Coulomb potential, E_{fs} and E_{uehl} include the finite size corrections without and with Uehling potential, respectively. All energies are in keV.

	state	E_{c}	E_{fs}	E_{uehl}
$^{185}\mathrm{Re}$	1s1/2	17229.12	9333.46	9394.02
	2s1/2	4398.85	3083.91	3100.44
	2p1/2	4398.85	4032.61	4059.50
	2p3/2	4033.07	3885.75	3910.50
	3s1/2	1912.97	1498.01	1504.28
	3p1/2	1912.97	1789.84	1798.66
	3p3/2	1804.01	1751.38	1759.75
	3d3/2	1804.01	1802.05	1810.30
	3d5/2	1773.14	1772.36	1780.16
$^{235}\mathrm{U}$	1s1/2	27351.29	12100.56	12175.51
	2s1/2	7074.68	4308.67	4332.13
	2p1/2	7074.68	5901.35	5941.39
	2p3/2	6130.65	5674.78	5711.89
	3s1/2	3033.18	2148.86	2158.31
	3p1/2	3033.18	2645.58	2659.26
	3p3/2	2751.54	2588.19	2601.27
	3d3/2	2751.54	2739.69	2754.06
	3d5/2	2679.66	2674.77	2688.10

Table 3.8: Overview of energy corrections due to residual second order electric quadrupole splitting $\Delta E_{2.\text{ord.}}$ and quadrupole-Uehling interaction $\Delta E_{\text{quad-uehl}}$ for ^{185}Re and ^{235}U. F is the total angular momentum of muon and nucleus, I_N is the nuclear angular momentum and μ-state is the muonic state in spectroscopic notation. For the muonic $2p$ and $3d$ states, these are mixed by the dynamic hyperfine structure, thus I_N (main) and μ-state (main) show the states with the largest contribution. E_{quad} is the binding energy without quadrupole Uehling and residual second order quadrupole interaction. The states are ordered descending in the total energy E_{tot}. All energies are in keV.

	F	I_N (main)	μ-state (main)	E_{quad}	$\Delta E_{2.\text{ord.}}$	$\Delta E_{\text{quad-uehl}}$	E_{tot}
^{185}Re	2	$5/2$	$1\text{s}1/2$	9394.02	3.21	0.00	9397.23
	6	$13/2$	$1\text{s}1/2$	8696.92	2.06	0.00	8698.98
	8	$15/2$	$1\text{s}1/2$	8444.32	1.76	0.00	8446.08
	2	$5/2$	$2\text{p}1/2$	4083.31	2.18	0.28	4085.77
	3	$5/2$	$2\text{p}1/2$	4077.79	2.07	0.23	4080.09
	3	$9/2$	$2\text{p}3/2$	3992.27	2.41	0.41	3995.09
	4	$7/2$	$2\text{p}1/2$	3957.33	2.10	0.26	3959.69
	3	$5/2$	$2\text{p}3/2$	3886.35	1.12	-0.22	3887.25
	5	$7/2$	$2\text{p}3/2$	3814.27	2.08	0.28	3816.63
	4	$9/2$	$2\text{p}1/2$	3734.93	1.03	-0.27	3735.69
	6	$9/2$	$2\text{p}3/2$	3650.57	1.95	0.25	3652.77
	5	$9/2$	$2\text{p}3/2$	3556.36	1.13	-0.24	3557.25
	7	$11/2$	$2\text{p}3/2$	3458.14	1.85	0.23	3460.22
	6	$11/2$	$2\text{p}3/2$	3344.35	0.93	-0.19	3345.09
	8	$13/2$	$2\text{p}3/2$	3111.03	0.68	0.02	3111.73
	7	$15/2$	$2\text{p}3/2$	2941.66	0.82	-0.15	2942.33
	8	$15/2$	$2\text{p}3/2$	2938.52	0.67	-0.16	2939.03
	3	$5/2$	$3\text{d}3/2$	1815.47	0.07	0.03	1815.57
	1	$5/2$	$3\text{d}3/2$	1804.28	0.11	-0.03	1804.36
	3	$7/2$	$3\text{d}5/2$	1783.72	0.05	0.02	1783.79
	0	$5/2$	$3\text{d}5/2$	1772.11	0.11	-0.04	1772.18
^{235}U	3	$7/2$	$1\text{s}1/2$	12175.51	6.83	0.00	12182.34
	7	$15/2$	$1\text{s}1/2$	11925.50	4.66	0.00	11930.16
	9	$17/2$	$1\text{s}1/2$	11835.54	3.54	0.00	11839.08
	3	$7/2$	$2\text{p}1/2$	6019.06	5.99	0.85	6025.90
	4	$7/2$	$2\text{p}1/2$	6015.01	5.96	0.83	6021.80
	4	$9/2$	$2\text{p}1/2$	5979.31	6.02	0.86	5986.19
	5	$9/2$	$2\text{p}3/2$	5928.94	6.06	0.88	5935.88
	6	$11/2$	$2\text{p}3/2$	5868.85	6.00	0.89	5875.74
	7	$15/2$	$2\text{p}1/2$	5798.66	5.30	0.91	5804.87
	8	$15/2$	$2\text{p}1/2$	5745.59	4.71	0.87	5751.17
	5	$7/2$	$2\text{p}3/2$	5673.10	3.12	-0.42	5675.80
	6	$9/2$	$2\text{p}3/2$	5621.02	3.02	-0.46	5623.58
	2	$7/2$	$2\text{p}3/2$	5620.12	2.78	-0.56	5622.34
	9	$17/2$	$2\text{p}1/2$	5613.24	2.05	0.13	5615.42
	3	$9/2$	$2\text{p}3/2$	5586.28	2.81	-0.54	5588.55
	7	$13/2$	$2\text{p}1/2$	5556.38	2.60	-0.50	5558.48
	9	$15/2$	$2\text{p}3/2$	5493.59	2.44	0.24	5496.27
	8	$15/2$	$2\text{p}1/2$	5479.30	2.14	-0.53	5480.91
	10	$17/2$	$2\text{p}3/2$	5393.16	1.77	0.13	5395.06
	9	$17/2$	$2\text{p}3/2$	5315.81	1.73	-0.44	5317.10
	3	$7/2$	$3\text{d}3/2$	2767.16	0.44	0.09	2767.69
	1	$7/2$	$3\text{d}5/2$	2663.35	0.61	-0.13	2663.83

3.3 Structure of muonic ^{185}Re & ^{187}Re

The analysis of x-rays emitted due to transitions in muonic atoms is one possibility to obtain information on the nuclear charge distribution and measure properties like RMS charge radii, or nuclear quadrupole moments. This Section analyzes the structure of muonic rhenium-185 and -187. So far, there is no absolute measurement of the charge radius of ^{185}Re [201] and the only experiment reported on muonic rhenium is an extraction of the quadrupole moments of ^{185}Re and ^{187}Re from the N x rays ($n=5 \rightarrow n=4$) of natural Re [202], which is mainly a mixture of these two isotopes. Therefore, the theoretical spectra of both isotopes have been used at the same time for fitting the experimental spectrum. As a consequence, the two extracted quadrupole moments in Ref [202] are not indepentent. During the work on this thesis, the quadrupole moments were extracted independently for the two isotopes. The experimental data used in this Section comes from measurements of muonic x-rays with isotopically pure rhenium have been performed in 2016 by the MuX Collaboration, using the high intensity muon beam at the Paul-Scherrer-Institut [203, 204].

In the following, the muonic transition energies and transition probabilities are analyzed, using the methods described in Sections 3.1 and 3.2. Thereby, the dependence of transitions and intensities of the N x rays ($n = 5 \rightarrow n = 4$) on the quadrupole moment is used in combination with experimental data on isotopically pure ^{185}Re and ^{187}Re to extract the nuclear quadrupole moment. Also, a good qualitative description based on the rigid-rotor nuclear model (Appendix D) of the K x-rays ($2p \rightarrow 1s$) is given.

After the muon beam hits the target, a muon can be captured in the Coulomb field of an atomic nucleus in a highly excited states. Then, it starts cascading towards the ground state. In principle, this is a complicated many-body probmlem, involing the nucleus, the muon and the atomic electrons. However, there is an intermediate region with $n \approx 4-7$, where finite nuclear size effects are still rather small and at the same time, the muon is not influenced significantly by the surrounding atomic electrons. Therefore, the system is essentially hydrogen-like and no many-body problem has to be solved. In addition, the hyperfine structure is mainly determined by the nuclear quadrupole moment. It has been realized, that in this region, more specifically the $n=5 \rightarrow n=4$ transitions, nuclear quadrupole moments can be extracted, which has been done for lutetium-175 in Ref. [194] and for natural rhenium in Ref. [202]. As a first application of the calculation of muonic spectra presented in this thesis, the dependence of the transition energies and intensities of the muonic N x rays on the nuclear quadrupole moment is calculated, and by comparing to measurements of isotopically pure ^{185}Re and ^{187}Re, a value for their spectroscopic quadrupole moment is extracted.

Following Sec. 3.1.5, the most intense transitions are the $E1$-transitions in the circular orbits $5g^{9/2} \rightarrow 4f^{7/2}$ and $5g^{7/2} \rightarrow 4f^{7/2}$. However, also the $5f^{7/2} \rightarrow 4d^{5/2}$, $5g^{7/2} \rightarrow 4f^{7/2}$, and $5f^{5/2} \rightarrow 4d^{5/2}$ transitions have to be considered, since they almost coincide in energy with the $5g^{7/2} \rightarrow 4f^{7/2}$ energies around 365 keV. Therefore, the following approach is chosen for the theoretical prediction: The four fine-structure states of the initial states $5g^{9/2}, 5g^{7/2}, 5f^{7/2}, 5f^{5/2}$ together with the nuclear ground state with $I = 5/2$ define a first model space. Now, the formalism described in Sec. 3.1.4 can be used to calculate the energies in this modelspace, including finite size effects, vacuum polarization (Uehling,

Källen-Sabry, Wichmann-Kroll in point-like approximation, quadrupole-Uehling), and rediagonalization of the electric quadrupole and magnetic dipole hyperfine interaction. In this way, also contributions non-linear in the nuclear quadrupole moment are included, in contrast to [202]. Excited nuclear states were not considered, since the quadrupole interaction in this case is compared to the nuclear rotational states. For the N x rays, the nuclear energy splitting is around three orders of magnitude larger. Furthermore, due to the small hyperfine splitting in the $n=4,5$ states, the residual second order terms, as described in Sec. 3.2.2, are very small. The same procedure is repeated for the final states with $n=4$, i.e. $4f7/2$, $4f5/2$, $4d5/2$, $4d3/2$. Then, the transition probabilities can be calculated from each initial to each final state. For this analysis, the relativistic formulas for $E1$ and $M1$ transitions from Sec. 3.1.5 are used, assuming an initial statistical population $\sim 2F+1$ for each initial state with total angular momentum F. Transitions of higher-order multipolarity have a much smaller transition rate. With this approach, every transition energy and corresponding intensity can be calculated for a given nuclear charge distribution

$$\rho_N(r_N, \vartheta_N) = \frac{N}{1 + \mathrm{e}^{\frac{r - c(1 + \beta Y_{20}(\vartheta))}{a}}},$$

where N is a normalization constant fixed by the condition $\int \mathrm{d}V \rho(r, \vartheta) = Z$. The three parameters a, c, β are calculated using $a = 2.3\,\mathrm{fm}/(4\ln 3)$, which is a reasonable estimate for most nuclei [182], such that the RMS charge radius agrees with the literature value from Ref. [165], and the spectroscopic quadrupole moment with some given value Q. The connection of the spectroscopic quadrupole Q moment with the nuclear charge distribution for a nucleus with ground state angular momentum I is

$$Q = 4\pi \frac{I(2I-1)}{(I+1)(2I+3)} \int\limits_0^\infty \mathrm{d}r_N \int\limits_0^\pi \mathrm{d}\vartheta_N \, r_N^4 \sin\vartheta_N \rho_N(r_N, \vartheta_N) \mathrm{P}_2(\cos\vartheta_N),$$

where $\mathrm{P}_l(x)$ are the Legendre polynomials from Appendix B. The value of the magnetic moment needed for the calculation of the magnetic dipole interaction is taken from [205]. The influence of finite size effects was checked by also using charged shell and homogeneously charged sphere distribution. With this parametrization, the entire spectrum can be calculated for a given spectroscopic quadrupole moment and by fitting the theoretically calculated spectrum to the experimental measured one, the quadrupole moment can be extracted. There are five groups of $E1$-transitions in energy range of the $5g \to 4f$ transitions, namely:

1. $5g9/2 \to 4f7/2$

2. $5g7/2 \to 4f5/2$

3. $5f7/2 \to 4d5/2$

4. $5g7/2 \to 4f7/2$

5. $5f5/2 \to 4d5/2$

Each of those groups consists of 15 or 16 individual lines itself due to the hyperfine structure. Therefore, 77 individual lines and corresponding intensities are taken into account in the fitting process.

The difference between two transition energies is especially sensitive to the quadrupole moment, since the majority of the uncertainty due to the nuclear RMS radius cancels, as described in [202]. Therefore, the energy differences of all $5g9/2 \rightarrow 4f7/2$ transition compared to the most intense transition in this group, called the centroid transition, is calculated and analogously the corresponding intensities are given relative to the centroid transition. The same holds for the other four groups. Then, the energy difference of the $5g9/2 \rightarrow 4f7/2$ centroid compared to the other four centroids is calculated. Thereby, the energy differences of all considered transitions compared to the $5g9/2 \rightarrow 4f7/2$ centroid is parametrized in terms of the nuclear quadrupole moment and the position of the $5g9/2 \rightarrow 4f7/2$ centroid can be fitted to the experimental spectrum as a free parameter. The relative intensities of the 5 different groups are either free fit parameters or obtained from other programs for cascade calculations [206]. It is too expensive to perform full calculations in the fitting process to experimental data. Instead, the full calculations are performed for several values of the quadrupole moment in the proximity of the expected value and a quadratic function is fitted for every transition energy and intensity as

$$\Delta E^{if}(Q) = \Delta E_0^{if} + \Delta E_1^{if} Q + \Delta E_2^{if} Q^2, \tag{3.49}$$

$$I^{if}(Q) = I_0^{if} + I_1^{if} Q + I_2^{if} Q^2. \tag{3.50}$$

The fitted function and the results from the full calculations agree on the 10^{-4} eV level in the region of the determined quadrupole moment. The resulting dependencies for ^{185}Re are given in Table 3.10 for the relative transition energies, in Table 3.11 for the intensities, and in Table 3.9 for fitted energy differences of the centroid transitions. For ^{187}Re, the coefficients differ only to a small extend to to different values for the magnetic moment and RMS charge radius. A main experimental challenge is understanding of the line shape due to the detector response function, which broadens the Lorentzian (due to natural life time) essentially into a Voigt profile. This issue is treated in [207] in detail.

The calculated spectrum parametrized by the nuclear quadrupole moment can now be fitted efficiently to the experimental spectrum and the result is shown in Fig. 3.6. The $5f5/2 \rightarrow 4d5/2$ group turned out not to be visible in the fit. Thereby, the preliminary extracted spectroscopic quadrupole moment of ^{185}Re and ^{187}Re is obtained as

$$Q_{\text{Re-185}} = 2.12(11) \,\text{barn},$$
$$Q_{\text{Re-187}} = x.xx(xx) \,\text{barn}$$

where the largest contribution to the uncertainty stems from the lineshape of the detectors. The value is in agreement with the previous literature values [188].

Furthermore, the low-lying $2p \rightarrow 1s$ transitions, or K x-rays, have been measured during the same experiments. The assumption of statistically populated $5g$ states, i.e. $\sim 2F + 1$, and a cascade $5g \rightarrow 4f \rightarrow 3d \rightarrow 2p \rightarrow 1s$ as explained in Sections 3.1.4 and 3.1.5 can explain the spectrum qualitatively, using the rigid rotor model for the nucleus (Appendix D). The corresponding comparison for the K x rays is shown in
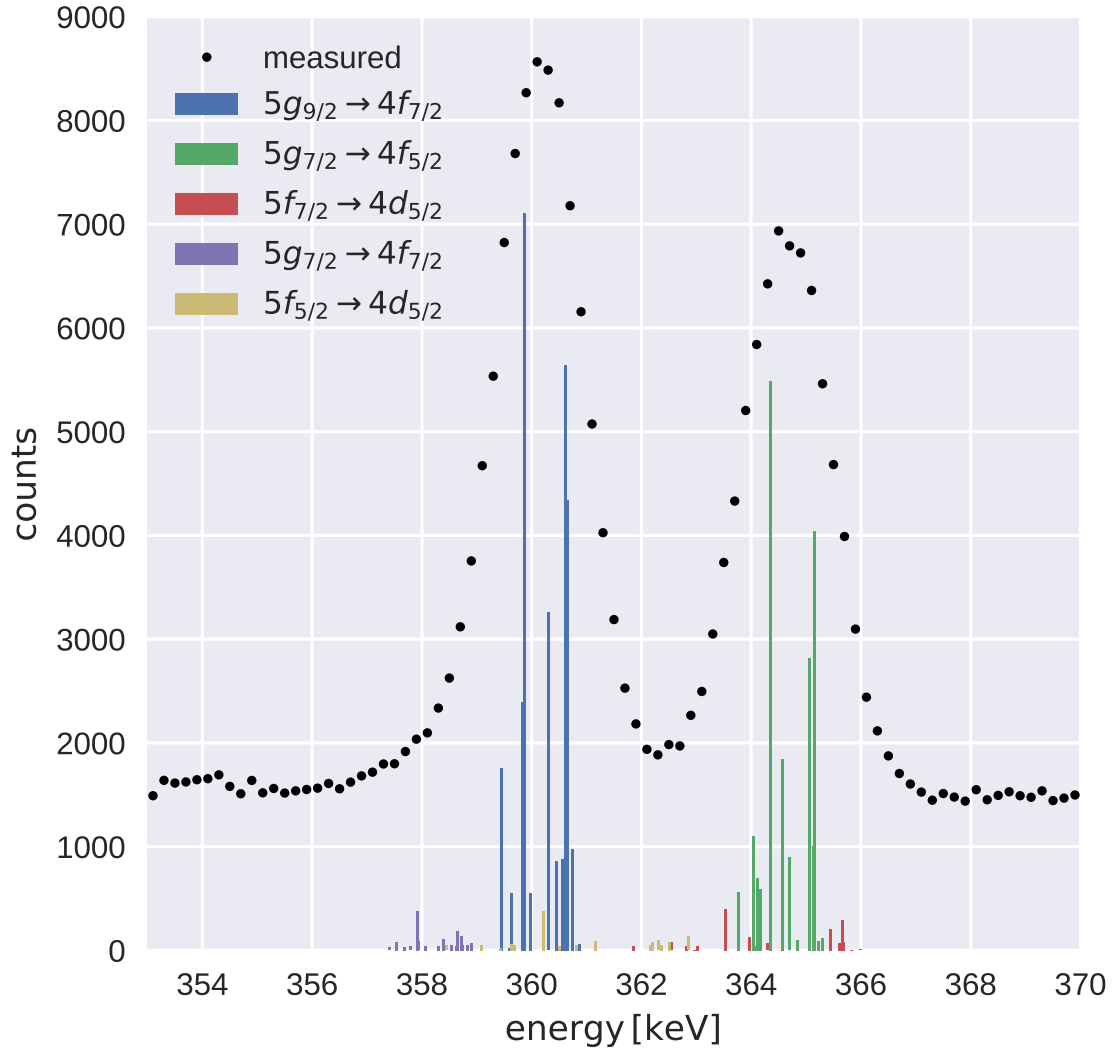
Figure 3.6: Comparison of the experimental spectrum for the $5g^{9/2} \rightarrow 4f^{7/2}$, $5g^{7/2} \rightarrow 4f^{7/2}$, $5f^{7/2} \rightarrow 4d^{5/2}$, $5g^{7/2} \rightarrow 4f^{7/2}$, and $5f^{5/2} \rightarrow 4d^{5/2}$ groups in ^{185}Re. The black dots are the measurements and the colored lines below show the calculations for line positions and corresponding transition probabilities.

Fig. 3.7. For the calculations of the spectra, the first five nuclear rotational states have been considered. In principle, from these spectra, the nuclear RMS radius can be extracted [112]. However, for the low-lying transitions in heavy muonic atoms, the nuclear polarization corrections, e.g. [198], have to be considered. These corrections are due to virtual excitations of nuclear states beyond the rigid rotor model and have to be treated with a more accurate nuclear model or experimental data on nuclear transitions. Thus, updated calculations from the nuclear physics side would be desirable in order to extract nuclear charge radii in connection with the calculations from the muonic side as presented in this thesis, which is discussed in more detail in the conclusion & outlook chapter.

Table 3.9: Quadratic fits of the energies of the centroid transitions. The formula for the energy difference in terms of a give quadrupole moment Q is given in Eq. (3.49). See Sec. 3.3 for details.

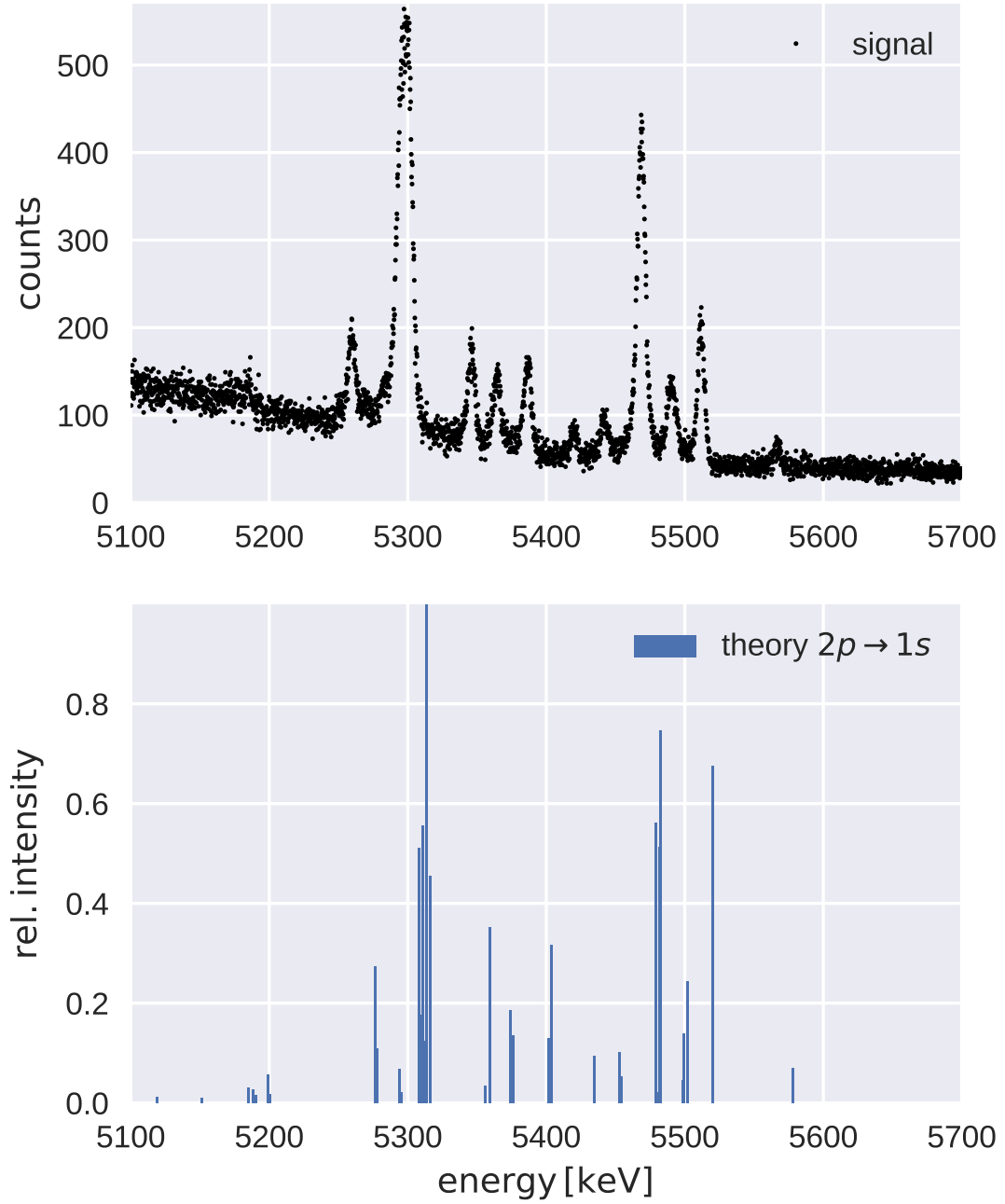| centroid	$F_i \rightarrow F_f$	ΔE_2^{if} [keV/barn^2]	ΔE_1^{if} [keV/barn]	ΔE_0^{if} [keV]
$5g^{9/2} \rightarrow 4f^{7/2}$	$7 \rightarrow 6$	0.0000	-0.1743	360.2145
$5g^{7/2} \rightarrow 4f^{5/2}$	$6 \rightarrow 5$	0.0040	-0.1601	364.6631
$5f^{7/2} \rightarrow 4d^{5/2}$	$6 \rightarrow 5$	-0.0016	-0.4396	364.4165
$5g^{7/2} \rightarrow 4f^{7/2}$	$6 \rightarrow 6$	-0.0004	-0.1775	358.2798
$5f^{5/2} \rightarrow 4d^{5/2}$	$5 \rightarrow 5$	-0.0039	-0.4480	361.1407

Figure 3.7: Comparison of experimental spectrum (upper plot) and theoretical calculations (lower plot) in the area of the K x rays for muonic ^{185}Re. The first 5 rotational states of the ^{185}Re nucleus and a muonic cascade starting from statistically populated $5g$ states have been used for the calculations. The spectrum is complex due to excited nuclear states and large hyperfine splitting in the muonic $2p$ states. The small shift of the theoretical values is due to the non-calculated nuclear polarization corrections. For further details see Sec. 3.3.

Table 3.10: Quadratic fits of the transitions energies for the 15 most intense transitions each for the $5g9/2 \to 4f7/2$, $5g7/2 \to 4f7/2$, $5f7/2 \to 4d5/2$, $5g7/2 \to 4f7/2$, and $5f5/2 \to 4d5/2$ groups in ^{185}Re. The formula for the transition energy in terms of a give quadrupole moment Q is given in Eq. (3.49). See Sec. 3.3 for details.

Group	$F_i \to F_f$	ΔE_2^{if} [eV/barn^2]	ΔE_1^{if} [eV/barn]	ΔE_0^{if} [eV]
$5g9/2 \to 4f7/2$	$7 \to 6$	0.0000	0.0000	0.0000
	$6 \to 6$	0.4349	-112.8421	-4.3710
	$6 \to 5$	-3.9990	374.5405	8.1664
	$5 \to 6$	0.0083	-130.4566	-8.6014
	$5 \to 5$	-4.4255	356.9260	3.9360
	$5 \to 4$	-0.0011	385.3921	20.3954
	$4 \to 5$	-4.3353	397.2028	0.5956
	$4 \to 4$	0.0891	425.6690	17.0550
	$4 \to 3$	-1.3357	210.0265	28.0955
	$3 \to 4$	0.2441	494.0067	14.3378
	$3 \to 3$	-1.1807	278.3642	25.3784
	$3 \to 2$	-2.3757	-23.6926	33.7363
	$2 \to 3$	-1.2154	350.5410	23.3930
	$2 \to 2$	-2.4104	48.4842	31.7510
	$2 \to 1$	-1.5016	-218.4484	36.5602
$5g7/2 \to 4f5/2$	$6 \to 5$	0.0000	0.0000	0.0000
	$5 \to 5$	0.4268	-116.6524	-6.0881
	$5 \to 4$	-4.0133	397.3030	15.1612
	$4 \to 5$	0.3365	-124.8666	-11.3476
	$4 \to 4$	-4.1035	389.0888	9.9017
	$4 \to 3$	-2.6732	339.4603	29.0257
	$3 \to 4$	-4.2588	440.6240	5.7383
	$3 \to 3$	-2.8284	390.9955	24.8623
	$3 \to 2$	-1.6187	86.2278	39.1264
	$2 \to 3$	-2.7939	463.6869	21.6868
	$2 \to 2$	-1.5843	158.9191	35.9509
	$2 \to 1$	-2.4783	-172.9226	46.2225
	$1 \to 2$	-1.3654	223.6477	33.7757
	$1 \to 1$	-2.2595	-108.1940	44.0473
	$1 \to 0$	-3.9788	-312.5737	49.2916
$5f7/2 \to 4d5/2$	$6 \to 5$	0.0000	0.0000	0.0000
	$5 \to 5$	2.3569	-252.5291	-6.3945
	$5 \to 4$	-39.2156	1142.4006	-7.6361
	$4 \to 5$	0.0075	-267.1910	-14.9468
	$4 \to 4$	-41.5650	1127.7387	-16.1884
	$4 \to 3$	-2.9973	940.7303	47.5074
	$3 \to 4$	-40.8162	1239.4485	-21.8866
	$3 \to 3$	-2.2485	1052.4401	41.8091
	$3 \to 2$	-21.1329	231.4531	70.3569
	$2 \to 3$	-1.6192	1208.9013	37.4969
	$2 \to 2$	-20.5036	387.9143	66.0447
	$2 \to 1$	-23.4328	-470.1437	68.4933
	$1 \to 2$	-20.9818	526.1606	63.5780
	$1 \to 1$	-23.9109	-331.8974	66.0266
	$1 \to 0$	1.6436	-869.1530	73.0235
$5g7/2 \to 4f7/2$	$6 \to 6$	0.0000	0.0000	0.0000
	$6 \to 5$	-4.4339	487.3826	12.5375
	$5 \to 6$	0.4268	-116.6524	-6.0881
	$5 \to 5$	-4.0071	370.7302	6.4493
	$5 \to 4$	0.4173	399.1963	22.9087
	$4 \to 5$	-4.0974	362.5159	1.1898
	$4 \to 4$	0.3270	390.9821	17.6492
	$4 \to 3$	-1.0978	175.3397	28.6898
	$3 \to 4$	0.1718	442.5174	13.4858
	$3 \to 3$	-1.2530	226.8749	24.5264
	$3 \to 2$	-2.4480	-75.1819	32.8844
	$2 \to 3$	-1.2185	299.5663	21.3508
	$2 \to 2$	-2.4135	-2.4905	29.7088
	$2 \to 1$	-1.5047	-269.4231	34.5180
	$1 \to 2$	-2.1947	62.2380	27.5336
	$1 \to 1$	-1.2858	-204.6945	32.3428
$5f5/2 \to 4d5/2$	$5 \to 5$	0.0000	0.0000	0.0000
	$5 \to 4$	-41.5725	1394.9297	-1.2415
	$4 \to 5$	2.3621	-267.5452	-10.8732
	$4 \to 4$	-39.2104	1127.3845	-12.1147
	$4 \to 3$	-0.6427	940.3761	51.5811
	$3 \to 4$	-39.9636	1153.2006	-21.9500
	$3 \to 3$	-1.3959	966.1922	41.7458
	$3 \to 2$	-20.2803	145.2052	70.2936
	$2 \to 3$	-2.0370	1124.7959	34.4113
	$2 \to 2$	-20.9214	303.8089	62.9591
	$2 \to 1$	-23.8506	-554.2491	65.4077
	$1 \to 2$	-20.4551	476.5200	57.6634
	$1 \to 1$	-23.3843	-381.5380	60.1120
	$1 \to 0$	2.1702	-918.7936	67.1089
	$0 \to 1$	-22.4779	-275.1695	57.4097

Table 3.11: Quadratic fits of the intensities for the 15 most intense transitions each for the $5g9/2 \rightarrow 4f7/2$, $5g7/2 \rightarrow 4f7/2$, $5f7/2 \rightarrow 4d5/2$, $5g7/2 \rightarrow 4f7/2$, and $5f5/2 \rightarrow 4d5/2$ groups in ^{185}Re. The formula for the transition energy in terms of a give quadrupole moment Q is given in Eq. (3.50). See Sec. 3.3 for details.

Group	$F_i \rightarrow F_f$	I_2^{if} [%/barn^2]	I_1^{if} [%/barn]	I_0^{if} [%]
$5g9/2 \rightarrow 4f7/2$	$7 \rightarrow 6$	0.000	0.000	100.000
	$6 \rightarrow 6$	-0.011	-0.115	8.045
	$6 \rightarrow 5$	-0.008	0.383	78.602
	$5 \rightarrow 6$	0.000	-0.002	0.311
	$5 \rightarrow 5$	-0.012	0.036	12.375
	$5 \rightarrow 4$	0.000	0.214	60.644
	$4 \rightarrow 5$	-0.001	0.012	0.669
	$4 \rightarrow 4$	-0.001	0.109	13.527
	$4 \rightarrow 3$	-0.002	0.007	45.818
	$3 \rightarrow 4$	0.000	0.019	0.837
	$3 \rightarrow 3$	-0.001	0.104	11.900
	$3 \rightarrow 2$	-0.002	-0.102	33.944
	$2 \rightarrow 3$	0.000	0.013	0.619
	$2 \rightarrow 2$	-0.001	0.050	7.725
	$2 \rightarrow 1$	-0.001	-0.105	25.000
$5g7/2 \rightarrow 4f5/2$	$6 \rightarrow 5$	0.000	0.000	100.000
	$5 \rightarrow 5$	0.022	0.218	12.062
	$5 \rightarrow 4$	0.036	0.360	72.591
	$4 \rightarrow 5$	0.003	0.024	0.730
	$4 \rightarrow 4$	0.008	0.088	18.102
	$4 \rightarrow 3$	0.021	0.397	50.423
	$3 \rightarrow 4$	0.001	0.009	1.642
	$3 \rightarrow 3$	0.012	-0.046	19.212
	$3 \rightarrow 2$	0.013	0.257	33.003
	$2 \rightarrow 3$	0.002	-0.022	2.192
	$2 \rightarrow 2$	0.009	-0.097	16.477
	$2 \rightarrow 1$	0.009	0.094	19.797
	$1 \rightarrow 2$	0.001	-0.027	1.829
	$1 \rightarrow 1$	0.004	-0.078	10.989
	$1 \rightarrow 0$	0.005	-0.008	10.262
$5f7/2 \rightarrow 4d5/2$	$6 \rightarrow 5$	0.000	0.000	100.000
	$5 \rightarrow 5$	-0.041	-0.307	12.106
	$5 \rightarrow 4$	-0.106	1.215	72.304
	$4 \rightarrow 5$	0.000	-0.002	0.738
	$4 \rightarrow 4$	-0.106	0.343	18.040
	$4 \rightarrow 3$	-0.007	0.381	50.338
	$3 \rightarrow 4$	-0.016	0.086	1.639
	$3 \rightarrow 3$	-0.002	0.330	19.267
	$3 \rightarrow 2$	-0.019	-0.188	32.976
	$2 \rightarrow 3$	-0.001	0.097	2.206
	$2 \rightarrow 2$	-0.009	0.170	16.510
	$2 \rightarrow 1$	-0.018	-0.275	19.773
	$1 \rightarrow 2$	0.000	0.056	1.836
	$1 \rightarrow 1$	-0.010	0.009	10.995
	$1 \rightarrow 0$	0.000	-0.157	10.257
$5g7/2 \rightarrow 4f7/2$	$6 \rightarrow 6$	0.000	0.000	100.000
	$6 \rightarrow 5$	0.722	1.664	10.899
	$5 \rightarrow 6$	-0.010	-0.401	10.234
	$5 \rightarrow 5$	-0.117	-8.661	68.235
	$5 \rightarrow 4$	0.022	-1.370	15.636
	$4 \rightarrow 5$	-0.009	-1.686	15.656
	$4 \rightarrow 4$	0.101	-3.994	44.693
	$4 \rightarrow 3$	0.210	-3.201	16.754
	$3 \rightarrow 4$	0.019	-1.220	16.889
	$3 \rightarrow 3$	-0.120	0.243	28.837
	$3 \rightarrow 2$	0.149	-2.527	14.555
	$2 \rightarrow 3$	-0.054	0.005	14.624
	$2 \rightarrow 2$	-0.166	1.893	19.289
	$2 \rightarrow 1$	0.015	-0.887	9.296
	$1 \rightarrow 2$	-0.066	0.637	9.265
	$1 \rightarrow 1$	-0.128	1.955	16.650
$5f5/2 \rightarrow 4d5/2$	$5 \rightarrow 5$	0.000	0.000	100.000
	$5 \rightarrow 4$	1.842	3.914	17.965
	$4 \rightarrow 5$	-0.008	-1.155	16.736
	$4 \rightarrow 4$	0.792	-16.181	56.816
	$4 \rightarrow 3$	0.382	-5.451	24.306
	$3 \rightarrow 4$	0.130	-5.071	24.769
	$3 \rightarrow 3$	-0.002	-1.881	25.862
	$3 \rightarrow 2$	0.644	-7.174	24.558
	$2 \rightarrow 3$	-0.017	-1.687	24.986
	$2 \rightarrow 2$	-0.278	3.084	8.988
	$2 \rightarrow 1$	0.079	-3.215	20.127
	$1 \rightarrow 2$	-0.351	2.589	19.702
	$1 \rightarrow 1$	0.043	1.509	1.602
	$1 \rightarrow 0$	-0.122	0.943	10.821
	$0 \rightarrow 1$	-0.154	3.105	10.510

3.4 Bound muon g factor in ${}^{4}_{2}$He

Another application of the calculations described in this thesis are connected to the bound muon g factor in muonic Helium-4, following the work presented in [2] by the first author B. Sikora. Although Helium is a light nucleus, finite nuclear size corrections have to be considered for precise theoretical predictions. In this thesis, the finite nuclear size, electronic Uehling, muonic Uehling, electronic second/higher order Uehling and electronic Källen-Sabry corrections to the bound muon g factor in muonic Helium-4 were calculated. All effects take an extended nuclear charge distribution into account, and the uncertainty due to the value of the RMS charge radius and model dependence of the nuclear charge distribution is taken into account. Other effects, like nuclear polarization, further one- and two-loop QED, recoil, hadronic and weak corrections have been calculated by the other authors in [2]. Thereby, a theoretical prediction of the bound-muon g factor in helium-4 on the 10^{-9} level is obtained.

The calculations are preformed analogously to Chapter 2, but now with a bound muon instead of a bound electron. This is, the Dirac equation

$$[\boldsymbol{\alpha} \cdot \mathbf{p} + \beta m_\mu + V_i(r)] \, |n\kappa m\rangle = E_{n\kappa} \, |n\kappa m\rangle$$

is solved for spherically symmetric potentials $V_i(r)$, which are described below. Then, according to Eq. (2.3), the g factors g_i, including the corrections due to V_i can be obtained by radial integration of the solutions as

$$g_i = \frac{2m_\mu \kappa}{j(j+1)} \int_0^\infty \mathrm{d}r r^3 f_{n\kappa}(r) g_{n\kappa}(r).$$

The finite nuclear size, the electric-loop (Fig. 1.4 with an external muon and internal electron) and muonic-loop Uehling (Fig. 1.4 with an external muon and internal muon) correction as well as the Källen-Sabry correction (Fig. 1.5 with an external muon and internal electron) to the bound muon g factor are considederd by using the corresponding potentials directly in the Dirac equation. A two-parameter Fermi charge distribution for ${}^{4}_{2}$He is used, such that the RMS value agrees with [165] (1.6755 fm):

$$\rho(r) = \frac{N}{1 + \mathrm{e}^{(r-c)/a}}.$$

The uncertainty of this charge distribution is estimated by using the uncertainty in the RMS value and the model dependence is estimated conventionally by varying the parameters a between 0.05 fm and 0.3 fm. The considered potentials are the point-like Coulomb potential $V_C(r)$ from Eq. (1.21), finite size electric potential $V(r)$ from Eq. (1.2), and Uehling potentials $V_{\mathrm{Uehl}}^{(m_e)}(r)$, $V_{\mathrm{Uehl}}^{(m_\mu)}(r)$ from Eq. (1.14) for the electric- and muonic-loop Uehling potential, respectively. Furthermore, the Källen-Sabry potential with electronic loops $V_{\mathrm{KS}}^{(m_e)}(r)$ from Eq. (1.15) is taken into account. The g-factor corrections are obtained as follows:

i	potential	g_i factor	$\delta g_i/10^{-8}$ correction
0	$V_0(r) = V_C(r)$	1.999857988825369	–
1	$V_1(r) = V(r)$	1.999858083413814	$+\ 9.46(4)$
2	$V_2(r) = V(r) + V_{\text{Uehl}}^{(m_e)}(r)$	1.999857602755145	$-48.0659(4)$
3	$V_3(r) = V(r) + V_{\text{Uehl}}^{(m_e)}(r) + V_{\text{Uehl}}^{(m_\mu)}(r)$	1.999857602647854	$-\ 0.01073(2)$
4	$V_4(r) = V(r) + V_{\text{Uehl}}^{(m_e)}(r) + V_{\text{KS}}(r)$	1.999857599294144	$-\ 0.346(1)$

The corrections δg_i are defined as:

correction	definition	effect
δg_1	$g_1 - g_0$	finite nuclear size correction
δg_2	$g_2 - g_1$	electronic-loop Ueling correction
δg_3	$g_3 - g_2$	muonic-loop Ueling correction
δg_4	$g_4 - g_2$	Källen-Sabry correction

Thus, mixed Källen-Sabry and muonic-loop Uehling terms are not considered, but since the individual contributions are already small, the combined contribution can be expected to be even smaller and not visible on the 10^{-10}-level at all. Finally, the electronic-loop Uehling correction can be written as $\delta g_1 = 47.9600 \times 10^{-8} + 0.1059 \times 10^{-8}$, where the first terms corresponds to the first order Uehling correction, which is the expectation value of the Uehling potential, corresponding to diagram Fig. 1.4 (a). The second term corresponds to the second and higher order Uehling corrections, mainly corresponding to diagram Fig. 1.4 (b), but also higher diagrams like Fig. 1.4 (c). Higher order iterations do not contribute on the 10^{-10} level. All calculated contributions to the theoretical prediction of the bound muon g factor in Helium-4 are presented in Table 3.12, where the contributions calculated in this thesis are highlighted in red. There are still uncalculated two-loop light-by-light-scattering diagrams, and the corresponding uncertainty is estimated as 5×10^{-9} [2].

In conclusion, it was demonstrated that the bound-muon g factor in Helium-4 can be calculated on the 10^{-9} level. A measurement of this g factor as g_{exp} with a similar experimental uncertainty could give access to an independent and one order more accurate value of the muon mass. For this, the dependency of the experimental value g_{exp} and the theoretical value g_{theory} on the muon mass has to be solved for an expression of the muon mass in dependency of the experimental and theoretical value as

$$g_{\text{theory}}(m_\mu) \overset{!}{=} g_{\text{exp}}(m_\mu)$$
$$\rightarrow m_\mu = m_\mu(g_{\text{theory}}, g_{\text{exp}}).$$

Alternatively, an independent determination of the muon magnetic moment anomaly of the free muon $g_{\text{free}} - 2$ may be possible by separating the contributions to the free g factor and the binding corrections as $g_{\text{theory}} = g_{\text{free}} + g_{\text{binding}} \overset{!}{=} g_{\text{exp}}$ [2]. However, it

is important to keep in mind, that the life time of a muonic atom is around one micro second, which is too short-lived for measuring the g factor of muonic atoms in the same way as for electronic atoms, for example in [58,60] and thus a measurement of the bound muon g factor on the 10^{-9} level represents a major experimental challenge.

Effect	Term	Numerical value	Ref.
Dirac value		1.999 857 988 8	[66, 130]
Finite nuclear size		0.000 000 094 6(4)	[165]
Nuclear pol.		0.000 000 000 0(10)	
One-loop SE	$(Z\alpha)^0$	0.002 322 819 5	[130, 208]
	all-order binding	0.000 000 084 9(10)	
One-loop VP	eVP, Uehling	-0.000 000 479 6	[209]
	eVP, magnetic loop	0.000 000 127 2(4)	
	μVP, Uehling	-0.000 000 000 1	[209]
	hadronic VP, Uehling	-0.000 000 000 1(1)	
Two-loop QED	$(Z\alpha)^0$	0.000 008 264 4	[210, 211]
	SE-SE, $(Z\alpha)^2$— $(Z\alpha)^5$	-0.000 000 000 1	[70, 71, 212, 213]
	S(eVP)E, $(Z\alpha)^2$	0.000 000 000 4	[210–213]
	Second-order Uehling	-0.000 000 001 1(4)	
	Källén-Sabry	-0.000 000 003 5	
	magnetic loop+Uehling	0.000 000 000 3	
	uncalculated LBL	0.000 000 000 0 (50)	
$\geq$ Three-loop QED	$(Z\alpha)^0$	0.000 000 610 6	[130, 214–216]
Nuclear recoil	$\left(\frac{m_\mu}{M}\right)^1$, all orders in $Z\alpha$	0.000 006 038 2	[81]
	$\left(\frac{m_\mu}{M}\right)^{2+}$, $(Z\alpha)^2$	-0.000 000 488 7	[217]
	radiative recoil	-0.000 000 004 7	[218]
Weak interaction	$(Z\alpha)^0$	0.000 000 003 1	[130, 219]
Hadronic	$(Z\alpha)^0$	0.000 000 139 3(12)	[130, 220–222]
Sum of terms calculated		2.002 195 193 4(20)$_{\text{calc}}$(50)$_{\text{uncalc}}$	

Table 3.12: Various contributions to the g factor of $\mu^4\text{He}^+$. The abbreviations are: eVP/μVP: VP due to virtual $e^-e^+/\mu^-\mu^+$ pairs. The estimated uncertainty of the nuclear size effect stems from the error bar of the root-mean-square nuclear radius and the uncertainty of the nuclear charge distribution model. The uncertainty is negligible, i.e., much less than 1 in the last digit, in the case of the terms for which none is indicated. In the last row, the uncertainties due to the calculated and uncalculated (two-loop LBL) terms are given separately. The table is taken from Ref. [2] and the contributions highlighted in red were performed in the framework of this thesis.

3.5 Conclusion

In this chapter, the following results have been presented:

- An up-to-date numerical approach, namely the dual-kinetic-balance method with B-splines, has been used for fully relativistic precision calculations in muonic atoms. Many important contributions have been implemented, like finite nuclear size effects, magnetic and electric hyperfine interactions, electron screening, QED corrections and cascade calculations in the framework of the dynamic hyperfine structure.

- Additionally, enhanced numerical approaches for calculation of the quadrupole vacuum polarization correction in Uehling approximation and for the treatment of residual second order quadrupole interactions has been presented. The extended nuclear charge distribution is considered without any approximations or expansions.

- The nuclear spectroscopic quadrupole moment of ^{185}Re and ^{187}Re was extracted by fitting theoretical to experimental spectra in connection with the experimental spectrum of isotopically pure muonic rhenium, measured by the MuX collaboration at the Paul-Scherrer-Institute. Also, the spectrum of the low-lying transitions was calculated and is in good qualitative agreement with the measured one. A corresponding manuscript is being prepared [5].

- Calculations of the finite nuclear size -, the firt and higher-order Uehling -, and the Källen-Sabry correction have been performed and have contributed to a theoretical prediction of the bound-muon g factor of helium-4 on a 10^{-9} level. With the same experimental accuracy, a more accurate value of the muon mass could be obtained.

Summary & Outlook

In the present thesis, nuclear structure effects in the spectra of heavy ions and muonic atoms caused by extended and deformed nuclear charge distributions are investigated. Here, the focus is on two topics, namely on the one hand improved calculations of the nuclear shape effect on the bound-electron g factor for spinless nuclei beyond the previously used perturbative evaluation, and on the other hand the analysis of the level structure and spectra of muonic atoms.

Chapter 2 is about non-perturbative calculations of nuclear shape effects on the bound-electron g factor. Here, the previously used perturbative method is introduced, which is called the effective radius method because the radius of a homogeneously charged sphere with approximately the same energy correction as the deformed nuclear charge distribution is used. Then, the non-perturbative, numerical method used in this thesis is explained, wherein the nuclear potential, the solution of the Dirac equation and the corresponding g factor are calculated all-numeric, starting with the deformed nuclear charge distribution. By performing calculations for a wide range of nuclei across the nuclear chart, it is shown that the perturbative evaluation overestimated the nuclear shape effect on the 20% level. The difference of the numerical and perturbative, effective radius method is investigated. The formulas for perturbative calculation of effective radius and corresponding energy correction of the homogeneously charged sphere are mainly responsible for the disagreement, but also the incompleteness of the effective radius method itself is visible.

Furthermore, it is demonstrated how the consideration of deformed nuclei can reduce the uncertainty in the theoretical prediction of finite-nuclear-size effects on the bound-electron g factor. The previous, conservative estimation of this uncertainty is the difference in the g factors due to a homogeneously charged sphere and a Fermi-type nuclear charge distribution. If parameters of the deformed nuclear charge distribution are available, the finite nuclear size and shape g-factor corrections can be calculated from thereon. In this way, the remaining model uncertainty is reduced to the uncertainty due to the parameters describing the deformed nuclear charge distribution. For hydrogenlike Uranium, it is shown that in this way the uncertainty of finite nuclear size effects can be halved.

Chapter 3 deals with high-precision calculations of the spectra of muonic atoms. As a first step, the implementation of the most important effects, namely finite nuclear size, vacuum polarization, recoil, and electron screening on the fine and hyperfine structure is discussed in Sec. 3.1. This includes calculations of the dynamic hyperfine structure, which means that the hyperfine structure is considered beyond first order for the most

important states. A finite basis set method with B-splines has been used, which is well established in atomic physics, but has not been used in the context of muonic atoms before. Thereby, a numerical representation of the complete spectrum of muon wave functions is obtained.

In Sec. 3.2, enhanced theoretical approaches for calculations connected to the electric quadrupole interaction in muonic atoms are presented. Firstly, this includes a numerical evaluation of the leading order vacuum polarization correction (Uehling potential) to the quadrupole matrix elements for an arbitrary, deformed nuclear charge distribution. In contrast to previous works, this is done without any approximations on the shape of the charge distribution or the distance between nucleus and muon. For this, a multi-pole expansion of the Uehling potential is performed. In this thesis, the corresponding expansion coefficients are given in a suitable form for numerical evaluation as well as analytically in terms of special functions. Secondly, the availability of a complete set of muonic states is used to calculate the residual second order quadrupole interaction which is not included in the framework of dynamic hyperfine structure. Both contributions are shown to be potentially visible in upcoming experiments.

In Sec. 3.3, the theoretical calculations of this thesis are combined with state-of-the-art experiments on muonic atom spectroscopy, performed recently at the Paul Scherrer Institute by the MuX collaboration. Theoretical spectra have been fitted to experimental ones by adjusting the parameters of the nuclear model. In this way, nuclear parameters can be extracted, which has been used to extract the nuclear quadrupole moment for $^{185}_{75}$Re from the $n=5 \to n=4$ x rays. Also, the spectra of low-lying muonic x rays in $^{185}_{75}$Re have been explained by the calculations in this thesis.

Finally, in Sec. 3.4, finite nuclear size and several vacuum polarization corrections to the bound muon g factor in $^{4}_{2}$He are presented. In combination with other calculations, this enabled a theoretical prediction of the g factor on the 10^{-9} level. It has been shown that not only the finite nuclear size and first order Uehling correction are important on this level of accuracy, but also the second order Uehling and Källen-Sabry corrections, which are two-loop QED corrections. It can be argued, that an independent and more accurate determination of the muon mass is possible in combination with measurements of a similiar accuracy.

The ongoing experimental campaign on spectroscopy of heavy muonic atoms by the MuX collaboration will provide further possibilities to extract information on atomic nuclei from muonic x rays, where the codes and methods from this thesis can be used. Due to progress in the experiments, it will be possible to analyze muonic x rays for the first time also for radioactive nuclei, which will include the measurement of muonic x rays up to the heaviest elements like $^{248}_{96}$Cu. Interesting are especially the analysis of low lying transitions, since they contain the most information on the nuclear structure, like the RMS radius of the electric charge distribution.

Currently, the limiting factor for theoretical predictions of low-lying transitions is the nuclear polarization correction. This is a second order correction to the bound state energies due to virtual excitation of the atomic nucleus in a muonic atom. Therefore, many excited states of the nucleus contribute and as a consequence, an advanced nuclear

model or plenty of experimental data has to be used for a description of the nuclear polarization correction. The calculation of the residual second order quadrupole interaction, as performed in this thesis, already demonstrated, how the muonic part in second order corrections can be evaluated with finite basis set methods. It would be very interesting and desirable to combine the muonic calculations of this thesis with up-to-date nuclear physics for a precise evaluation of the nuclear polarization correction in heavy muonic atoms.

Thinking further ahead, it would be insightful to crosscheck the consistency of nuclear effects in muonic and electronic atoms in the high-Z regime. For example, muonic atom spectroscopy with $^{248}_{96}\text{Cu}$ can be expected in the near future and the shape of the nuclear charge distribution can be potentially extracted from the corresponding muonic x rays. Although this is a radioactive isotope, it has a half-life of several hundreds of thousands of years, so also Penning trap experiments on the bound electron g factor in $^{248}_{96}\text{Cu}$ might be feasible. Then, the parameters of the nuclear charge distribution obtained from muonic x rays can be used to calculate the finite nuclear size and nuclear shape effects for the bound electron g factor. Provided that all other contributions, like two-loop QED corrections, are under control, a comparison with the measured g factor can test the consistency of nuclear effects in electronic and muonic atoms.
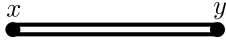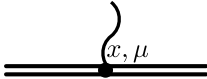
Appendix A

Conventions and notation

Variables

For the relativistic notation in Chapter 1, the symbols x, y, z, z_1, z_2, and p are used for four vectors corresponding to $x^\mu = (x^0, \mathbf{x}) = (x^0, x^1, x^2, x^3)$. The scalar product is $x_\mu y^\mu = x^0 y^0 - \mathbf{x} \cdot \mathbf{y}$, corresponding to the metric $g^{\mu\nu} = \mathrm{diag}(1, -1, -1, -1)$.

In all other chapters, three dimensional vectors in spherical coordinates are written as bold symbols $\mathbf{r} = (r, \vartheta, \varphi)$, where φ is the polar angle and ϑ is the azimuthal angle. The volume element is as usual $\mathrm{d}^3\mathbf{r} = \mathrm{d}r\mathrm{d}\varphi\mathrm{d}\vartheta\, r^2 \sin\vartheta$.

Feynmanrules

In Chapter 1, the following Feynman rules in position space are needed, where the notation follows [136]. If external lines are needed, the corresponding solutions of the Dirac equation have to be used.

fermion propagator (ext. field): $\qquad$ $\qquad S_{\mathcal{A}}(x,y) \quad$ from Eq. (1.8)

fermion propagator (free): $\qquad$ $\qquad S_F(x-y)$ from Eq. (1.4)

photon propagator: $\qquad$ $\qquad g_{\mu\nu} \dfrac{1}{4\pi^2} \dfrac{1}{(x-y)^2 - i\epsilon}$

vertex: $\qquad$ $\qquad -ie\gamma^\mu \int \mathrm{d}^4 x$

Dirac matrices

The following representation of the Dirac matrices is chosen, following [42]:
β *and* γ *matrices:*

$$\beta = \gamma^0 = \begin{pmatrix} \mathbf{1} & \mathbf{0} \\ \mathbf{0} & -\mathbf{1} \end{pmatrix}; \qquad \gamma^i = \begin{pmatrix} \mathbf{0} & \boldsymbol{\sigma}^i \\ -\boldsymbol{\sigma}^i & \mathbf{0} \end{pmatrix}$$

with

$$\mathbf{0} = \begin{pmatrix} 0 & 0 \\ 0 & 0 \end{pmatrix}; \quad \mathbf{1} = \begin{pmatrix} 1 & 0 \\ 0 & 1 \end{pmatrix}; \quad \boldsymbol{\sigma}^1 = \begin{pmatrix} 0 & 1 \\ 1 & 0 \end{pmatrix}; \quad \boldsymbol{\sigma}^2 = \begin{pmatrix} 0 & -i \\ i & 0 \end{pmatrix}; \quad \boldsymbol{\sigma}^3 = \begin{pmatrix} 1 & 0 \\ 0 & -1 \end{pmatrix};$$

α *matrices:*

$$\boldsymbol{\alpha}^i = \gamma^0 \gamma^i = \begin{pmatrix} \mathbf{0} & \boldsymbol{\sigma}_i \\ \boldsymbol{\sigma}_i & \mathbf{0} \end{pmatrix}; \quad \text{with } i \in \{1, 2, 3\}.$$

System of units and physical constants

Relativistic muonic natural units are used, where $\hbar = c = m_\mu = 1$, where $\hbar$ is the reduced Planck's constant, c is the speed of light in vacuum and m_μ is the mass of the considered bound fermion. For example, the electron mass in this system of units has the numerical value of the mass ratio $m_e/m_\mu = 1/206.7682826$ [223]. As in Chapter 2 the bound electron g factor is considered, factors of the electron mass m_e are included in the results. In Chapter 3 on muonic atoms, consequently factors of m_μ are not always explicitly included. Furthermore, Lorentz-Heavyside units of electromagnetism are used, corresponding to $\epsilon_0 = \mu_0 = 1$, where ϵ_0 is the vacuum permittivity and μ_0 the vacuum permeability. Table A.1 gives an overview of the SI-values of the basis units and derived quantities.

Table A.1: Overview of the SI-values of the basis units for the used natural systems of units and other important derived quantities. SI Values for $\hbar$, c, m_μ, ϵ_0, μ_0 are taken from [223].

Planck's constant	$\hbar$	1.054571800	$\times 10^{-34}\,\mathrm{kg\ m^2 s^{-1}}$
speed of light	c	299792458	$\mathrm{m\ s^{-1}}$
muon mass	m_μ	1.883531594	$\times 10^{-28}\,\mathrm{kg}$
vacuum permittivity	ϵ_0	8.854187817	$\times 10^{-12}\,\mathrm{kg^{-1}m^{-3}s^4A^2}$
vacuum permeability	μ_0	12.566370614	$\times 10^{-7}\ \ \mathrm{kg\ m\ s^{-2}A^{-2}}$
distance	$\hbar/(m_\mu c)$	1.86759431	$\times 10^{-15}\,\mathrm{m}$
time	$\hbar/(m_\mu c^2)$	6.22962405	$\times 10^{-24}\,\mathrm{s}$
energy	$m_\mu c^2$	1.69283377	$\times 10^{-11}\,\mathrm{kg\ m^2 s^{-2}}$

Appendix B

Special functions

Gamma function

The Gamma funciton is defined as [192, Eq. 5.2.1]

$$\Gamma(z) = \int_0^\infty e^{-t} t^{z-1} \mathrm{d}t, \tag{B.1}$$

where the real part of the complex number z has to be strictly greater than zero (otherwise via analytic continuation).

Meijer G-function

The Meijer G-function is a general special function, which includes many other functions as special cases. It is defined as

$$G_{p,q}^{m,n}\left(z \left| \begin{matrix} a_1, ..., a_p \\ b_1, ..., b_q \end{matrix} \right. \right) = \frac{1}{2\pi \mathrm{i}} \int_L \left(\frac{\prod_{\ell=1}^m \Gamma(b_\ell - s) \prod_{\ell=1}^n \Gamma(1 - a_\ell + s)}{\left(\prod_{\ell=m}^{q-1} \Gamma(1 - b_{\ell+1} + s) \prod_{\ell=n}^{p-1} \Gamma(a_{\ell+1} - s) \right)} \right) z^s \mathrm{d}s, \tag{B.2}$$

where the integration contour L is a suitable path around the poles of $\Gamma(b_l - l)$ and $\Gamma(1 - a_l + s)$ [192, Eq. 16.17.1], and $\Gamma(z)$ is defined in Eq. (B.1). m, n, p, q are integers with $0 \le m \le q$ and $0 \le n \le p$, and $z, a_1, ..., a_p, b_1, ..., b_q$ are complex numbers where none of the differences $a_i - b_j$ must be a positive integers for $0 \le i \le n$, $0 \le j \le m$.

Arbitrary precision implementations exist in several libraries and computer algebra systems, for example in [199, 200].

Hypergeometric function

The Hypergeometric function $F(a, b, c, z)$ (or sometimes $_2F_1(a, b, c, z)$) is a special case of the Meijer G-function from Eq. (B.2) and can be obtained by

$$F(a, b, c, z) = \frac{\Gamma(c)}{\Gamma(a)\Gamma(b)} G_{2,2}^{1,2}\left(-z \left| \begin{matrix} 1 - a, 1 - b \\ 0, c \end{matrix} \right. \right)$$

It can also be written in terms of Gamma functions as [192, Eq. 15.2.1]

$$F(a, b, c, z) = \frac{\Gamma(c)}{\Gamma(a)\Gamma(b)} \sum_{s=0}^\infty \frac{\Gamma(a+s)\Gamma(b+s)}{\Gamma(c+s)s!} z^s \tag{B.3}$$

for $|z| < 1$ (otherwise via analytic continuation) and c must not be a negative integer or zero.

Wigner D-function

The Wigner D-function is defined via the Hypergeometric function from Eq. (B.3) as [150]

$$D^l_{m_1 m_2}(\alpha, \beta, \gamma) = \mathrm{e}^{-i(m_1\alpha + m_2\gamma)} d^l_{m_1 m_2}(\beta), \tag{B.4}$$

$$d^l_{m_1 m_2}(\beta) = \frac{\xi_{m_1 m_2}}{\mu!} \left(\frac{(s + \mu + \nu)!(s + \mu)!}{s!(s + \nu)!} \right)^{1/2} (\sin \beta/2)^\mu (\cos \beta/2)^\nu$$
$$\times F(-s, s + \mu + \nu + 1, \mu + 1, \sin^2 \beta/2),$$

where $\mu = |m_1 - m_2|$, $\nu = |m_1 + m_2|$, $s = l - (\mu + \nu)/2$ and

$$\xi_{m_1 m_2} = \begin{cases} 1; m_2 \leq m_1 \\ (-1)^{m_2 - m_1}; m_2 < m_1, \end{cases}$$

and $F(a, b, c, x)$ are the hypergeometric functions from Eq. (B.3).

Spherical Harmonics

The spherical harmonics $\mathrm{Y}_{lm}(\vartheta, \varphi)$ are special cases of the Wigner D-functions [150] from Eq. (B.4):

$$\mathrm{Y}_{lm}(\vartheta, \varphi) = \sqrt{\frac{2l + 1}{4\pi}} D^{l*}_{m0}(\varphi, \vartheta, 0) \tag{B.7}$$

The normalized spherical Harmonics $C_{lm}(\vartheta, \varphi)$ are used frequently, which are connected to the spherical harmonics as

$$C_{lm}(\vartheta, \varphi) = \sqrt{\frac{4\pi}{2l + 1}} \mathrm{Y}_{lm}(\vartheta, \varphi).$$

The set of all spherical harmonics $\mathrm{Y}_{lm}(\vartheta, \varphi)$ with positive integer l and $-l \leq m \leq l$ is a complete orthonormal set [150] in the space of functions depending on $(\vartheta, \varphi) \in [0, \pi] \otimes [0, 2\pi]$. Thus, an arbitrary function $f(\vartheta, \varphi)$ can be written as

$$f(\vartheta, \varphi) = \sum_{l=0}^{\infty} \sum_{m=-l}^{l} a_{lm} \mathrm{Y}_{lm}(\vartheta, \varphi),$$

with the expansion coefficients obtained by

$$a_{lm} = \int_0^{2\pi} \mathrm{d}\varphi \int_0^{\pi} \mathrm{d}\vartheta \sin \vartheta \mathrm{Y}^*_{lm}(\vartheta, \varphi) f(\vartheta, \varphi)$$

Legendre Polynomials

The Legendre Polynomials $P_l(\cos\vartheta)$ can be expressed in terms of the Spherical Harmonics from Eq. (B.7) as

$$P_l(\cos\vartheta) = \sqrt{\frac{4\pi}{2l+1}}\, Y_{l0}(\vartheta, 0).$$

For two vectors $\mathbf{r}_i = (r_i, \vartheta_i, \varphi_i)$ with $i \in \{1, 2\}$, let $y = \cos\sphericalangle(\mathbf{r}_1, \mathbf{r}_2)$ be the cosine of the angle between the two vectors. Then, the following addition theorem [150] for Legendre polynomials and spherical harmonics holds:

$$P_l(y) = \frac{4\pi}{2l+1}\sum_{m=-l}^{l} Y_{lm}^*(\vartheta_1, \varphi_1) Y_{lm}(\vartheta_2, \varphi_2). \tag{B.8}$$

Appendix C

Angular momentum theory

Following the notation from [150], important results from the theory of rotations and angular momenta are summarized in this Section.

Rotation of coordinate systems

The passive point of view for rotations is used in this thesis, where vectors are invariant objects and the coordinate axes are rotated. Two systems, the laboratory system with unprimed coordinates and the body-fixed system with primed coordinates are considered. The position of the axes of the body-fixed system is described by the Euler angles $\Omega = (\phi, \theta, \psi)$ in terms of the following three successive rotations of the axes of the laboratory system:

1. Angle ψ about z axis

2. Angle θ about (original) y axis

3. Angle ϕ about (original) z axis

Let **r** be a vector with coordinates (r, ϑ, φ) in the laboratory frame and $(r', \vartheta', \varphi')$ in the body fixed frame. Then, the primed angles are a function of the unprimed angles and the three Euler angles and the corresponding relations relations between the coordinates are

$$
\begin{aligned}
r &= r', \\
\cos \vartheta' &= \cos \vartheta \ \cos \theta + \sin \vartheta \sin \theta \cos(\varphi - \phi), \\
\cot(\varphi' + \psi) &= \cot(\varphi - \phi) \cos(\theta) - \frac{\cot \vartheta \sin \theta}{\sin(\varphi - \phi)}.
\end{aligned}
$$

This gives the following relation for spherical harmonics as a function of (ϑ', φ') and the corresponding (ϑ, φ):

$$
\mathrm{Y}_{lm}(\vartheta', \varphi') = \sum_{m_2 = -l}^{l} \mathrm{Y}_{lm_2}(\vartheta, \varphi) D^l_{m_2\, m}(\phi, \theta, \phi), \tag{C.1}
$$

where $D^l_{m_1\, m_2}(\alpha, \beta, \gamma)$ are the Wigner D functions defined in Eq. (B.4) and $\mathrm{Y}_{lm}(\vartheta, \varphi)$ are defined in Eq. (B.4).

Irreducible tensor operators

An irreducible tensor operator [150] of rank l is a $m = 2l + 1$-component operator $t_{lm}(\mathbf{x})$, depending on the variables $\mathbf{x}$, where the components transform like the spherical harmonics in Eq. (C.1) under a rotation of the coordinate system described by the Euler angles (ϕ, θ, ψ) as

$$t_{lm}(\mathbf{x}') = \sum_{m_2=l}^{l} t_{lm_2}(\mathbf{x}) D^l_{m_2 m}(\phi, \theta, \psi)$$

where the new coordinates $\mathbf{x}'$ are a function of the old $\mathbf{x}$ and the Euler angles (ϕ, θ, ψ). The expectation values of irreducible tensor in rotational states $|l_1 m_1\rangle$, and $|l_2 m_2\rangle$ of defined angular momenta l_1, l_2 with projections m_1, m_2 on the z axis, respectively, can be written as [150]

$$\left\langle l_1 m_1 \middle| \hat{t}_{lm} \middle| l_2 m_2 \right\rangle = (-1)^{l_1-m_1} \begin{pmatrix} l_1 & l & l_2 \\ -m_1 & m & m_2 \end{pmatrix} \left\langle l_1 \middle\| \hat{t}_l \middle\| l_2 \right\rangle, \tag{C.2}$$

where the double-bar matrix element on the right hand side is called the *reduced matrix element*, and the Wigner-$3j$-symbol is defined in [150, Section 8.]. This is also known as the Wigner-Eckardt-theorem, and thereby, the dependence of the matrix element on m_1, m_2, and m can be explicitly written in terms of the Wigner-$3j$-symbol. In practice, this means that matrix elements of irreducible operators only have to be calculated once for a convenient choice of m_1, m_2, and m, and then can be translated to other values of the projections.

Let two systems, system 1 and 2, with rotational states $|j_1 m_1\rangle$ and $|j_2 m_2\rangle$ be coupled to states with defined total angular momentum j as

$$|jm\, j_1 j_2\rangle = \sum_{m_1, m_2} \mathrm{C}^{jm}_{j_1 m_1\, j_2 m_2} |j_1 m_1\rangle \otimes |j_1 m_1\rangle, \tag{C.3}$$

and analogously for j', m', j_1', j_2'. Here, $\mathrm{C}^{jm}_{j_1 m_1\, j_2 m_2}$ are the Clebsch-Gordan-coefficients, as defined in [150, Section 9.], and let $t^{(1)}_{lm_1}$, $t^{(2)}_{lm_2}$ be two irreducible tensor operators acting on system 1 and system 2, respectively. Then, the scalar product of these to operators is defined as

$$t^{(1)}_l \cdot t^{(2)}_l = \sum_m (-1)^{-m}\, t^{(1)}_{lm} \cdot t^{(2)}_{l\,-m}, \tag{C.4}$$

and matrix elements thereof can be expressed in terms of the reduced matrix elements as [150]

$$\left\langle j'm'\, j_1'j_2' \middle| t^{(1)}_l \cdot t^{(2)}_l \middle| jm\, j_1 j_2 \right\rangle = \delta_{j'j} \delta_{m'm} (-1)^{j+j_1+j_2'} \begin{Bmatrix} j_1' & j_1 & l \\ j_2 & j_2' & j \end{Bmatrix} \left\langle j_1' \middle\| t^{(1)}_l \middle\| j_1 \right\rangle \left\langle j_2' \middle\| t^{(2)}_l \middle\| j_2 \right\rangle. \tag{C.5}$$

Another frequently used application of the coupled representation is calculation of the matrix element of one operator $t_{lm_1}^{(1)}$ acting only on the coordinates of system 1, when the states are given in the coupled representation from Eq. (C.3). In this case, the matrix element reads as [150]

$$\left\langle j'm'\, j_1'j_2' \middle| t_{lm_l}^{(1)} \middle| jm\, j_1 j_2 \right\rangle = \delta_{j_2'j_2}(-1)^{j+j_1'+j_2-l}\sqrt{2j+1}\, \mathrm{C}_{jm\,lm_l}^{j'm'} \begin{Bmatrix} j_1 & j_2 & j \\ j' & l & j_1' \end{Bmatrix} \left\langle j_1' \middle\| t_l^{(1)} \middle\| j_1 \right\rangle.$$

(C.6)

Appendix D

Symmetric Rigid Rotor Model

In this thesis, a nuclear model is needed which can account for the two following aspects: Firstly, for the description of hyperfine interactions, it needs to describe the angular momentum of the nucleus in its ground state rotational band, both for nuclei with vanishing and integer or half-integer non-zero ground state angular momentum. Secondly, finite nuclear-size effects need to be included. Therefore, the nuclear model needs to include the charge distribution and correspondingly, the distribution of higher-order multipoles, like the electric quadrupole and magnetic dipole. The simplest collective nuclear model which complies with these requirements is the symmetric rigid rotor model. Here, the nucleus is described by rigid charge distribution in a body fixed nuclear frame, i.e. the nucleus does not change the shape of the charge distribution, but it can rotate, which is described by a rotation of the nuclear body-fixed frame in the laboratory frame. The following derivations follow [150, 224, 225], where the notation and conventions follow [150]. Generally, rotations of coordinate system are described by the three Euler angles $\Omega = (\phi, \theta, \psi)$, where ϕ, θ are the polar and azimuthal angles, respectively, describing the position of the body-fixed z' axis in the laboratory frame. ψ is the polar angle describing the orientation of the x' and y' axes with respect to the z' axis. Correspondingly, these are the degrees of freedom for the rigid rotor model. Motivated by the classical kinetic energy of an axially symmetric rotating rigid body, the total energy can be expressed in terms of the moments of inertia $\Theta_1 {=} \Theta_2$, Θ_3 and corresponding angular velocities ω_i of the rigid body as

$$E_{\mathrm{rot}} = \frac{1}{2}\Theta_1\left(\omega_1^2 + \omega_2^2\right) + \frac{1}{2}\Theta_3\omega_3^2$$

The angular velocities can be expressed in terms of the Euler angles as

$$\omega_1 = \dot{\theta}\sin\psi - \dot{\phi}\sin\theta\cos\psi,$$
$$\omega_2 = \dot{\theta}\cos\psi + \dot{\phi}\sin\theta\sin\psi,$$
$$\omega_3 = \dot{\phi}\cos\theta + \dot{\psi},$$

and thereby, the Hamiltonian is obtained by introducing the generalized momenta $p_x = \partial E/\partial x$ for $x \in \{\phi, \theta, \psi\}$ as

$$\mathrm{H}(\theta, p_\phi, p_\theta, p_\psi) = \frac{1}{2\Theta_1\Theta_3}\left(\Theta_1 p_\psi^2 + \Theta_3 p_\theta^2 + \Theta_3\left(\frac{p_\psi}{\tan\theta} - \frac{p_\phi}{\sin\theta}\right)^2\right) - \frac{(\theta p_\theta - p_\theta\theta)\cot\theta}{2\Theta_1}p_\theta.$$

Since non-cartesian coordinates are used, the last term vanishes for the classical theory but is needed for the correct quantum theory with naiv canonical quantization due to operator ordering [226]. The corresponding Schrödinger equation for the quantized symmetric rigid rotor can now be obtained by substituting $p_x \rightarrow -i\partial_x$. The eigenenergies E and corresponding eigenfunctions can be found by solving the equation [224]

$$-\frac{1}{2\Theta_1}\left\{\partial_\theta^2 + \cot\theta\partial_\theta + \left(\frac{\Theta_1}{\Theta_3} + \cot^2\theta\right)\partial_\psi^2 + \frac{1}{\sin^2\theta}\partial_\phi - \frac{2\cos\theta}{\sin^2\theta}\partial_\phi\partial_\psi\right\}D(\phi,\theta,\psi)$$
$$= ED(\phi,\theta,\psi).$$

The eigenfunctions turn out to be the complex conjugate of the Wigner D functions $D_{MK}^{I*}(\phi,\theta,\psi)$ and the corresponding eigenenergies are [227]

$$E_{IK} = \frac{I(I+1)}{2\Theta_1} + \left(\frac{1}{2\Theta_3} - \frac{1}{2\Theta_1}\right)K^2. \tag{D.1}$$

Here, K is angular momentum in the body-fixed nuclear frame, corresponding to the ground state angular momentum, if the nucleus is in its ground-state rotational band, and $I(I+1)$ is the squared total angular momentum with the z component in the laboratory frame M. With the correct normalization, the wave functions of the symmetric top read as

$$\langle\phi\,\theta\,\psi|IMK\rangle = \sqrt{\frac{2I+1}{8\pi^2}}D_{MK}^{I*}(\phi,\theta,\psi), \tag{D.2}$$

where the Wigner D functions are defined in Eq. (B.4). Instead of the energies E_{IK}, also the measured energies of the corresponding nuclear states [169] are used. Matrix elements of operators $O(\phi,\theta,\psi)$ depending on the Euler angles are calculated as

$$\langle I'M'K'|\hat{O}|IMK\rangle =$$
$$\frac{\sqrt{(2I+1)(2I'+1)}}{8\pi^2}\int_0^{2\pi}\mathrm{d}\phi\int_0^\pi\mathrm{d}\theta\sin\theta\int_0^{2\pi}\mathrm{d}\psi D_{M'K'}^{I'}(\phi,\theta,\psi)O(\phi,\theta,\psi)D_{MK}^{I*}(\phi,\theta,\psi)$$

For example, in atomic structure calculations, the matrix elements, reduced in M but not in K, of spherical harmonics $Y_{lm}(\theta,\phi)$ with rigid rotor states are needed:

$$\langle I_1K||Y_l(\theta,\phi)||I_2K\rangle = (-1)^{I_2+K}\sqrt{(2I_1+1)(2I_2+1)(2l+1)/(4\pi)}\begin{pmatrix} I_1 & I_2 & l \\ -K & K & 0 \end{pmatrix}.$$
$$\tag{D.3}$$

Bibliography

[1] N. Michel, N. S. Oreshkina, and C. H. Keitel, "Theoretical prediction of the fine and hyperfine structure of heavy muonic atoms," Phys. Rev. A **96**, 032510 (2017).

[2] B. Sikora, H. Cakir, N. Michel, V. Debierre, N. S. Oreshkina, N. A. Belov, V. A. Yerokhin, C. H. Keitel, and Z. Harman, "Improving the accuracy of the muon mass and magnetic moment anomaly via the bound-muon g factor," Phys. Rev. D **97**, 111301 (2018).

[3] Niklas Michel, Natalia S. Oreshkina, "Higher-order corrections for the dynamic hyperfine structure of muonic atoms," ArXiv e-prints **arXiv:1809.06623** (2018).

[4] Niklas Michel, Jacek Zatorski, Natalia S. Oreshkina, Christoph H. Keitel, "Non-perturbative analysis of nuclear shape effects on the bound electron g factor," ArXiv e-prints **arXiv:1806.00405** (2018).

[5] A. Adamczak, A. Antognini, K. Kirch., N. Ritjoho, A. Skawaran, N. Berger, R. Pohl, F. Wauters, T. E. Cocolios, N. Seveijns, R. Dressler, R. Eichler, A. Knecht, A. Papa, E. Rapisarda, P. Indelicato, K. Jungmann, L. Willmann, N. Michel, N. S. Oreshkina, C. H. Keitel, M. Pospelov, P. Reiter, and S. Roccia, "On the analysis of the hyperfine splitting in muonic spectra: Re-185 and re-187," In preparation (2018).

[6] N. S. Oreshkina, S. M. Cavaletto, N. Michel, Z. Harman, and C. H. Keitel, "Hyperfine splitting in simple ions for the search of the variation of fundamental constants," Phys. Rev. A **96**, 030501 (2017).

[7] W. H. Wollaston, "A method of examining refractive and dispersive powers, by prismatic reflection," Phil. Trans. R. Soc. Lond. **92**, 365 (1802).

[8] J. Fraunhofer, "Bestimmung des Brechungs- und des Farbenzerstreungs-Vermögens verschiedener Glasarten, in Bezug auf die Vervollkommnung achromatischer Fernröhre," Annalen der Physik **56**, 264 (1817).

[9] G. Kirchhoff and R. Bunsen, "Chemische Analyse durch Spectralbeobachtungen," Annalen der Physik **186**, 161 (1860).

[10] G. Kirchhoff and R. Bunsen, "Chemische Analyse durch Spectralbeobachtungen," Annalen der Physik **189**, 337 (1861).

[11] A. J. Ångström, "Ueber die fraunhofer'schen linien im sonnenspectrum," Annalen der Physik **193**, 290 (1862).

[12] J. J. Balmer, "Notiz über die Spectrallinien des Wasserstoffs," Annalen der Physik **261**, 80 (1885).

[13] A. J. Ångström, "Optische Untersuchungen," Annalen der Physik **170**, 141 (1853).

[14] W. Huggins, "On the spectrum of the flame of hydrogen," Proceedings of the Royal Society of London **30**, 576 (1880).

[15] H. W. Vogel, "Über die neuen Wasserstofflinien und die Dissociation des Calciums," Berichte der deutschen chemischen Gesellschaft **13**, 274 (1880).

[16] J. R. Rydberg, *Recherches sur la constitution des spectres d'émission des éléments chimiques*, vol. 23 of *Kungliga vetenskapsakademiens handlingar* (Kungliga Vetenskapsakademien, 1889).

[17] I. Martinson and L. Curtis, "Janne rydberg – his life and work," Nuclear Instruments and Methods in Physics Research Section B: Beam Interactions with Materials and Atoms **235**, 17 (2005). The Physics of Highly Charged Ions.

[18] T. Lyman, "The spectrum of hydrogen in the region of extremely short wave lengths," Astrophysical Journal **23**, 181 (1906).

[19] F. Paschen, "Zur Kenntnis ultraroter Linienspektra," Annalen der Physik **332**, 537 (1908).

[20] F. S. Brackett, "Visible and infra-red radiation of hydrogen," Astrophysical Journal **56**, 154 (1922).

[21] A. H. Pfund, "The emission of nitrogen and hydrogen in the infrared," The Journal of the Optical Society of America **9**, 193 (1924).

[22] C. J. Humphreys, "The sixth series in the spectrum of atomic hydrogen," Journal of Research of the National Bureau of Standards **50**, 1 (1953).

[23] J. J. Thomson, "Cathode rays," Philosophical Magazine **44**, 293 (1953).

[24] H. Rechenberg, "The electron in physics - selection from a chronology of the last 100 years," European Journal of Physics **18**, 145 (1997).

[25] E. Rutherford, "The scattering of α and β particles by matter and the structure of the atom," The London, Edinburgh, and Dublin Philosophical Magazine and Journal of Science **21**, 669 (1911).

[26] M. Planck, "Über das Gesetz der Energieverteilung im Normalspektrum," in "Von Kirchhoff bis Planck: Theorie der Wärmestrahlung in historisch-kritischer Darstellung," , H.-G. Schöpf, ed. (Vieweg+Teubner Verlag, Wiesbaden, 1978), pp. 178–191.

[27] N. Bohr, "On the constitution of atoms and molecules," Philosophical Magazine **26**, 1 (1913).

[28] J. J. Thomson, "On the structure of the atom : an investigation of thee stability and-periods of oscillation of a number of corpuscles arranged at equal intervals around the circumference of a circle; with application of the results to the theory of atomic structure," Philosophical Magazine **7**, 6 (1904).

[29] A. Sommerfeld, "Zur quantentheorie der spektrallinien," Annalen der Physik **356**, 1 (1916).

[30] E. Schrödinger, "Quantisierung als Eigenwertproblem (erste Mitteilung)," Annalen der Physik **384**, 361 (1926).

[31] E. Schrödinger, "Quantisierung als Eigenwertproblem (zweite Mitteilung)," Annalen der Physik **384**, 489 (1926).

[32] E. Schrödinger, "Quantisierung als Eigenwertproblem (dritte Mitteilung)," Annalen der Physik **385**, 437 (1926).

[33] E. Schrödinger, "Quantisierung als Eigenwertproblem (vierte Mitteilung)," Annalen der Physik **386**, 109 (1926).

[34] W. Heisenberg, "Über quantentheoretische Umdeutung kinematischer und mechanischer Beziehungen." Zeitschrift für Physik **33**, 879 (1925).

[35] M. Born and P. Jordan, "Zur Quantenmechanik," Zeitschrift für Physik **34**, 858 (1925).

[36] M. Born, W. Heisenberg, and P. Jordan, "Zur Quantenmechanik. II." Zeitschrift für Physik **35**, 557 (1926).

[37] E. Schrödinger, "Über das Verhältnis der Heisenberg-Born-Jordanschen Quantenmechanik zu der meinem," Annalen der Physik **384**, 734.

[38] P. Zeeman, "Ueber einen Einfluss der Magnetisirung auf die Natur des von einer Substanz emittirten Lichtes," Verhandlungen der Physikalischen Gesellschaft zu Berlin (1896).

[39] G. E. Uhlenbeck and S. Goudsmit, "Ersetzung der Hypothese vom unmechanischen Zwang durch eine Forderung bezüglich des inneren Verhaltens jedes einzelnen Elektrons," Die Naturwissenschaften **47**, 953 (1925).

[40] P. A. M. Dirac, "The quantum theory of the electron," Proceedings of the Royal Society of London A: Mathematical, Physical and Engineering Sciences **117**, 610 (1928).

[41] B. Thaller, *The Dirac equation* (Springer-Verlag, 1992).

[42] W. Greiner, *Relativistic Quantum Mechanics* (Springer-Verlag, Berlin Heidelberg, 2000), 3rd ed.

[43] W. E. Lamb and R. C. Retherford, "Fine structure of the hydrogen atom by a microwave method," Phys. Rev. **72**, 241 (1947).

[44] J. E. Nafe, E. B. Nelson, and I. I. Rabi, "The hyperfine structure of atomic hydrogen and deuterium," Phys. Rev. **71**, 914 (1947).

[45] P. Kusch and H. M. Foley, "Precision measurement of the ratio of the atomic 'g values' in the $^2p_{\frac{3}{2}}$ and $^2p_{\frac{1}{2}}$ states of gallium," Phys. Rev. **72**, 1256 (1947).

[46] P. Kusch and H. M. Foley, "The magnetic moment of the electron," Phys. Rev. **74**, 250 (1948).

[47] J. Schwinger, "On quantum-electrodynamics and the magnetic moment of the electron," Phys. Rev. **73**, 416 (1948).

[48] T. W. Hänsch, A. L. Schawlow, and G. W. Series, "The spectrum of atomic hydrogen," Scientific America **240**, 94 (1979).

[49] B. Odom, D. Hanneke, B. D'Urso, and G. Gabrielse, "New measurement of the electron magnetic moment using a one-electron quantum cyclotron," Phys. Rev. Lett. **97**, 030801 (2006).

[50] D. Hanneke, S. Fogwell, and G. Gabrielse, "New measurement of the electron magnetic moment and the fine structure constant," Phys. Rev. Lett. **100**, 120801 (2008).

[51] T. Kinoshita and M. Nio, "Improved α^4 term of the electron anomalous magnetic moment," Phys. Rev. D **73**, 013003 (2006).

[52] T. Aoyama, M. Hayakawa, T. Kinoshita, and M. Nio, "Revised value of the eighth-order contribution to the electron $g - 2$," Phys. Rev. Lett. **99**, 110406 (2007).

[53] T. Aoyama, M. Hayakawa, T. Kinoshita, and M. Nio, "Tenth-order electron anomalous magnetic moment: Contribution of diagrams without closed lepton loops," Phys. Rev. D **91**, 033006 (2015).

[54] T. Aoyama, M. Hayakawa, T. Kinoshita, and M. Nio, "Erratum: Tenth-order electron anomalous magnetic moment: Contribution of diagrams without closed lepton loops [phys. rev. d 91, 033006 (2015)]," Phys. Rev. D **96**, 019901 (2017).

[55] G. Gabrielse, D. Hanneke, T. Kinoshita, M. Nio, and B. Odom, "New determination of the fine structure constant from the electron g value and qed," Phys. Rev. Lett. **97**, 030802 (2006).

[56] G. Gabrielse, D. Hanneke, T. Kinoshita, M. Nio, and B. Odom, "Erratum: New determination of the fine structure constant from the electron g value and qed [phys. rev. lett. 97, 030802 (2006)]," Phys. Rev. Lett. **99**, 039902 (2007).

[57] H. Haffner, T. Beier, N. Hermanspahn, H.-J. Kluge, W. Quint, S. Stahl, J. Verdu, and G. Werth, "High-accuracy measurement of the magnetic moment anomaly of the electron bound in hydrogenlike carbon," Phys. Rev. Lett. **85**, 5308 (2000).

[58] S. Sturm, F. Köhler, J. Zatorski, A. Wagner, Z. Harman, G. Werth, W. Quint, C. Keitel, and K. Blaum, "High-precision measurement of the atomic mass of the electron," Nature **506**, 467 (2014).

[59] J. Verdu, S. Djekic, H. Haffner, S. Stahl, T. Valenzuela, M. Vogel, G. Werth, H.-J. Kluge, and W. Quint, "Electronic g factor of hydrogenlike oxygen $^{16}o^{7+}$," Phys. Rev. Lett. **92**, 093002 (2004).

[60] S. Sturm, A. Wagner, B. Schabinger, J. Zatorski, Z. Harman, W. Quint, G. Werth, C. H. Keitel, and K. Blaum, "g factor of hydrogenlike $si13+28$," Phys. Rev. Lett. **107**, 023002 (2011).

[61] L. S. Brown and G. Gabrielse, "Geonium theory: Physics of a single electron or ion in a penning trap," Rev. Mod. Phys. **58**, 233 (1986).

[62] S. Sturm, G. Werth, and K. Blaum, "Electron g-factor determinations in penning traps," Ann. Phys. **525**, 620 (2013).

[63] S. Sturm, M. Vogel, F. Köhler-Langes, W. Quint, K. Blaum, and G. Werth, "High-precision measurements of the bound electron's magnetic moment," Atoms **5**, 4 (2017).

[64] M. Vogel and W. Quint, "Aspects of fundamental physics in precision spectroscopy of highly charged ions in penning traps," Annalen der Physik **525**, 505 (2013).

[65] M. Vogel *et al.*, "Penning-trap experiments for spectroscopy of highly-charged ions at hitrap," Physica Scripta **2015**, 014066 (2015).

[66] G. Breit, "The magnetic moment of the electron," Nature **122**, 649 (1928).

[67] S. G. Karshenboim, "Non-relativistic calculations of the g-factor of a bound electron," Physics Letters A **266**, 380 (2000).

[68] K. Pachucki *et al.*, "Nonrelativistic qed approach to the bound-electron g factor," Phys. Rev. Lett. **93**, 150401 (2004).

[69] K. Pachucki, U. D. Jentschura, and V. A. Yerokhin, "Erratum: Nonrelativistic qed approach to the bound-electron g factor [phys. rev. lett. 93, 150401 (2004)]," Phys. Rev. Lett. **94**, 229902 (2005).

[70] K. Pachucki *et al.*, "Complete two-loop correction to the bound-electron g factor," Phys. Rev. A **72**, 022108 (2005).

[71] A. Czarnecki, M. Dowling, J. Piclum, and R. Szafron, "Two-loop binding corrections to the electron gyromagnetic factor," Phys. Rev. Lett. **120**, 043203 (2018).

[72] V. A. Yerokhin and Z. Harman, "One-loop electron self-energy for the bound-electron g factor," Phys. Rev. A **95**, 060501 (2017).

[73] V. A. Yerokhin and Z. Harman, "Two-loop qed corrections with closed fermion loops for the bound-electron g factor," Phys. Rev. A **88**, 042502 (2013).

[74] B. Sikora, V. A. Yerokhin, N. S. Oreshkina, H. Cakir, C. H. Keitel, and Z. Harman, "Theory of the two-loop self-energy correction to the g factor in non-perturbative Coulomb fields," ArXiv e-prints **arXiv:1804.05733** (2018).

[75] D. A. Glazov and V. M. Shabaev, "Finite nuclear size correction to the bound-electron g factor in a hydrogenlike atom," Physics Letters A **297**, 408 (2002).

[76] A. V. Nefiodov, G. Plunien, and G. Soff, "Nuclear-polarization correction to the bound-electron g factor in heavy hydrogenlike ions," Phys. Rev. Lett. **89**, 081802 (2002).

[77] A. V. Volotka and G. Plunien, "Nuclear polarization study: New frontiers for tests of qed in heavy highly charged ions," Phys. Rev. Lett. **113**, 023002 (2014).

[78] M. I. Eides and T. J. S. Martin, "Universal binding and recoil corrections to bound state g factors in hydrogenlike ions," Phys. Rev. Lett. **105**, 100402 (2010).

[79] K. Pachucki, "Nuclear mass correction to the magnetic interaction of atomic systems," Phys. Rev. A **78**, 012504 (2008).

[80] V. M. Shabaev, "Qed theory of the nuclear recoil effect on the atomic g factor," Phys. Rev. A **64**, 052104 (2001).

[81] V. M. Shabaev and V. A. Yerokhin, "Recoil correction to the bound-electron g factor in h-like atoms to all orders in αz," Phys. Rev. Lett. **88**, 091801 (2002).

[82] J. Zatorski, N. S. Oreshkina, C. H. Keitel, and Z. Harman, "Nuclear shape effect on the g factor of hydrogenlike ions," Phys. Rev. Lett. **108**, 063005 (2012).

[83] J. Zatorski, B. Sikora, S. G. Karshenboim, S. Sturm, F. Köhler-Langes, K. Blaum, C. H. Keitel, and Z. Harman, "Extraction of the electron mass from g-factor measurements on light hydrogenlike ions," Phys. Rev. A **96**, 012502 (2017).

[84] V. A. Yerokhin, K. Pachucki, Z. Harman, and C. H. Keitel, "Qed theory of the nuclear magnetic shielding in hydrogenlike ions," Phys. Rev. Lett. **107**, 043004 (2011).

[85] G. Werth, H. Häffner, N. Hermanspahn, H.-J. Kluge, W. Quint, and J. Verdú, "The g factor of hydrogenic ions: A test of bound state qed," in "The Hydrogen Atom: Precision Physics of Simple Atomic Systems," , S. G. Karshenboim, F. Bassani, F. Pavone, M. Inguscio, and T. Hänsch, eds. (Springer Berlin Heidelberg, Berlin, Heidelberg, 2001), pp. 204–220.

[86] V. M. Shabaev, D. A. Glazov, N. S. Oreshkina, A. V. Volotka, G. Plunien, H.-J. Kluge, and W. Quint, "g-factor of heavy ions: A new access to the fine structure constant," Phys. Rev. Lett. **96**, 253002 (2006).

[87] V. A. Yerokhin, E. Berseneva, Z. Harman, I. I. Tupitsyn, and C. H. Keitel, "g factor of light ions for an improved determination of the fine-structure constant," Phys. Rev. Lett. **116**, 100801 (2016).

[88] S. G. KARSHENBOIM, "Precision study of positronium: Testing bound state qed theory," International Journal of Modern Physics A **19**, 3879 (2004).

[89] A. Pineda and J. Soto, "Potential nrqed: The positronium case," Phys. Rev. D **59**, 016005 (1998).

[90] K. Pachucki and S. G. Karshenboim, "Complete results for positronium energy levels at order $m\alpha^6$," Phys. Rev. Lett. **80**, 2101 (1998).

[91] A. Czarnecki, K. Melnikov, and A. Yelkhovsky, "Positronium s-state spectrum: Analytic results at $o(m\alpha^6)$," Phys. Rev. A **59**, 4316 (1999).

[92] J. Zatorski, "$o(m\alpha^6)$ corrections to energy levels of positronium with nonvanishing orbital angular momentum," Phys. Rev. A **78**, 032103 (2008).

[93] A. P. Mills and G. H. Bearman, "New measurement of the positronium hyperfine interval," Phys. Rev. Lett. **34**, 246 (1975).

[94] M. W. Ritter, P. O. Egan, V. W. Hughes, and K. A. Woodle, "Precision determination of the hyperfine-structure interval in the ground state of positronium. v," Phys. Rev. A **30**, 1331 (1984).

[95] K. Danzmann, M. S. Fee, and S. Chu, "Doppler-free laser spectroscopy of positronium and muonium: Reanalysis of the 1s-2s measurements," Phys. Rev. A **39**, 6072 (1989).

[96] D. Hagena, R. Ley, D. Weil, G. Werth, W. Arnold, and H. Schneider, "Precise measurement of n=2 positronium fine-structure intervals," Phys. Rev. Lett. **71**, 2887 (1993).

[97] M. S. Fee, A. P. Mills, S. Chu, E. D. Shaw, K. Danzmann, R. J. Chichester, and D. M. Zuckerman, "Measurement of the positronium 1^3s_1-2^3s_1 interval by continuous-wave two-photon excitation," Phys. Rev. Lett. **70**, 1397 (1993).

[98] K. P. Jungmann, "Past, Present and Future of Muonium," ArXiv e-prints **nucl-ex/0404013** (2004).

[99] D. Casperson, T. Crane, V. Hughes, P. Souder, R. Stambaugh, P. Thompson, H. Orth, G. zu Putlitz, H. Kaspar, H. Reist, and A. Denison, "A new high precision measurement of the muonium hyperfine structure interval $\delta\nu_1$," Physics Letters B **59**, 397 (1975).

[100] W. Liu, M. G. Boshier, S. Dhawan, O. van Dyck, P. Egan, X. Fei, M. Grosse Perdekamp, V. W. Hughes, M. Janousch, K. Jungmann, D. Kawall, F. G. Mariam, C. Pillai, R. Prigl, G. zu Putlitz, I. Reinhard, W. Schwarz, P. A. Thompson, and K. A. Woodle, "High precision measurements of the ground state hyperfine structure interval of muonium and of the muon magnetic moment," Phys. Rev. Lett. **82**, 711 (1999).

[101] K. Pachucki, "$\alpha(z\alpha)^2 e_f$ correction to hyperfine splitting in hydrogenic atoms," Phys. Rev. A **54**, 1994 (1996).

[102] S. G. Karshenboim, "Leading logarithmic corrections and uncertainty of muonium hyperfine splitting calculations," Zeitschrift für Physik D Atoms, Molecules and Clusters **36**, 11 (1996).

[103] S. A. Blundell, K. T. Cheng, and J. Sapirstein, "All-order binding corrections to muonium hyperfine splitting," Phys. Rev. Lett. **78**, 4914 (1997).

[104] M. Nio and T. Kinoshita, "Radiative corrections to the muonium hyperfine structure. ii. the $\alpha(z\alpha)^2$ correction," Phys. Rev. D **55**, 7267 (1997).

[105] M. I. Eides, H. Grotch, and V. A. Shelyuto, "Second order in mass ratio radiative-recoil corrections to hyperfine splitting in muonium," Phys. Rev. D **58**, 013008 (1998).

[106] "Muonium Spectroscopy Experiment Using Microwave," http://museum.kek.jp/, called 2018-11-13.

[107] S. J. Brodsky and R. F. Lebed, "Production of the smallest qed atom: True muonium ($\mu^+\mu^-$)," Phys. Rev. Lett. **102**, 213401 (2009).

[108] A. Bogomyagkov, V. Druzhinin, E. Levichev, A. Milstein, and S. Sinyatkin, "Low-energy electron-positron collider to search and study ($\mu^+\mu^-$) bound state," ArXiv e-prints **physics.acc-ph/1708.05819** (2017).

[109] W. Y. Chang, "A cloud-chamber study of meson absorption by thin pb, fe, and al foils," Rev. Mod. Phys. **21**, 166 (1949).

[110] V. L. Fitch and J. Rainwater, "Studies of x-rays from mu-mesonic atoms," Phys. Rev. **92**, 789 (1953).

[111] J. A. Wheeler, "Some consequences of the electromagnetic interaction between μ^--mesons and nuclei," Rev. Mod. Phys. **21**, 133 (1949).

[112] D. Hitlin, S. Bernow, S. Devons, I. Duerdoth, J. W. Kast, E. R. Macagno, J. Rainwater, C. S. Wu, and R. C. Barrett, "Muonic atoms. i. dynamic hyperfine structure in the spectra of deformed nuclei," Phys. Rev. C **1**, 1184 (1970).

[113] A. Zehnder, F. Boehm, W. Dey, R. Engfer, H. Walter, and J. Vuilleumier, "Charge parameters, isotope shifts, quadrupole moments, and nuclear excitation in muonic 170–174,176yb," Nuclear Physics A **254**, 315 (1975).

[114] R. Powers, F. Boehm, P. Vogel, A. Zehnder, T. King, A. Kunselman, P. Roberson, P. Martin, G. Miller, R. Welsh *et al.*, "Muonic x-ray study of the charge distribution of 165ho," Nuclear Physics A **262**, 493 (1976).

[115] Y. Yamazaki, E. B. Shera, M. V. Hoehn, and R. M. Steffen, "Measurement and model-independent analysis of the x rays of muonic ^{150}Sm and ^{152}Sm," Phys. Rev. C **18**, 1474 (1978).

[116] Y. Tanaka, R. M. Steffen, E. B. Shera, W. Reuter, M. V. Hoehn, and J. D. Zumbro, "Precision muonic-atom measurements of nuclear quadrupole moments and the sternheimer effect in rare-earth atoms," Phys. Rev. Lett. **51**, 1633 (1983).

[117] Y. Tanaka, R. M. Steffen, E. B. Shera, W. Reuter, M. V. Hoehn, and J. D. Zumbro, "Systematics of ground-state quadrupole moments of odd-a deformed nuclei determined with muonic m x rays," Phys. Rev. C **29**, 1830 (1984).

[118] Y. Tanaka, R. M. Steffen, E. B. Shera, W. Reuter, M. V. Hoehn, and J. D. Zumbro, "Measurement and analysis of the muonic x rays of ^{151}Eu and ^{153}Eu," Phys. Rev. C **29**, 1897 (1984).

[119] P. Bergem, G. Piller, A. Rueetschi, L. A. Schaller, L. Schellenberg, and H. Schneuwly, "Nuclear polarization and charge moments of ^{208}Pb from muonic x rays," Phys. Rev. C **37**, 2821 (1988).

[120] R. Powers, F. Boehm, A. Zehnder, A. Kunselman, and P. Roberson, "A precision determination of the radial charge parameters and the quadrupole moment of 181ta using muonic x-rays," Nuclear Physics A **278**, 477 (1977).

[121] G. Fricke, C. Bernhardt, K. Heilig, L. Schaller, L. Schellenberg, E. Shera, and C. Dejager, "Nuclear ground state charge radii from electromagnetic interactions," Atomic Data and Nuclear Data Tables **60**, 177 (1995).

[122] E. Borie and G. A. Rinker, "The energy levels of muonic atoms," Rev. Mod. Phys. **54**, 67 (1982).

[123] S. Devons and I. Duerdoth, *Muonic Atoms* (Springer US, Boston, MA, 1995), pp. 295–423.

[124] C. S. Wu and L. Wilets, "Muonic atoms and nuclear structure," Annual Review of Nuclear Science **19**, 527 (1969).

[125] G. Rinker, "Static and dynamic muonic-atom codes-muon and rurp," Computer Physics Communications **16**, 221 (1979).

[126] R. Pohl *et al.*, "The size of the proton," Nature **466**, 213 (2010).

[127] A. Antognini, F. Nez, K. Schuhmann, F. D. Amaro, F. Biraben, J. M. R. Cardoso, D. S. Covita, A. Dax, S. Dhawan, M. Diepold, L. M. P. Fernandes, A. Giesen, A. L. Gouvea, T. Graf, T. W. Hänsch, P. Indelicato, L. Julien, C.-Y. Kao, P. Knowles, F. Kottmann, E.-O. Le Bigot, Y.-W. Liu, J. A. M. Lopes, L. Ludhova, C. M. B. Monteiro, F. Mulhauser, T. Nebel, P. Rabinowitz, J. M. F. dos Santos, L. A. Schaller, C. Schwob, D. Taqqu, J. F. C. A. Veloso, J. Vogelsang, and R. Pohl, "Proton structure from the measurement of 2s-2p transition frequencies of muonic hydrogen," Science **339**, 417 (2013).

[128] R. Pohl, F. Nez, L. M. P. Fernandes, F. D. Amaro, F. Biraben, J. M. R. Cardoso, D. S. Covita, A. Dax, S. Dhawan, M. Diepold, A. Giesen, A. L. Gouvea, T. Graf,

T. W. Hänsch, P. Indelicato, L. Julien, P. Knowles, F. Kottmann, E.-O. Le Bigot, Y.-W. Liu, J. A. M. Lopes, L. Ludhova, C. M. B. Monteiro, F. Mulhauser, T. Nebel, P. Rabinowitz, J. M. F. dos Santos, L. A. Schaller, K. Schuhmann, C. Schwob, D. Taqqu, J. F. C. A. Veloso, and A. Antognini, "Laser spectroscopy of muonic deuterium," Science **353**, 669 (2016).

[129] A. Beyer, L. Maisenbacher, A. Matveev, R. Pohl, K. Khabarova, A. Grinin, T. Lamour, D. C. Yost, T. W. Hänsch, N. Kolachevsky, and T. Udem, "The rydberg constant and proton size from atomic hydrogen," Science **358**, 79 (2017).

[130] P. J. Mohr, D. B. Newell, and B. N. Taylor, "Codata recommended values of the fundamental physical constants: 2014," Rev. Mod. Phys. **88**, 035009 (2016).

[131] J. Arrington and I. Sick, "Evaluation of the proton charge radius from electron–proton scattering," Journal of Physical and Chemical Reference Data **44**, 031204 (2015).

[132] H. Fleurbaey, S. Galtier, S. Thomas, M. Bonnaud, L. Julien, F. m. c. Biraben, F. m. c. Nez, M. Abgrall, and J. Guéna, "New measurement of the $1s-3s$ transition frequency of hydrogen: Contribution to the proton charge radius puzzle," Phys. Rev. Lett. **120**, 183001 (2018).

[133] G. W. Bennett, B. Bousquet, H. N. Brown, G. Bunce, R. M. Carey, P. Cushman, G. T. Danby, P. T. Debevec, M. Deile, H. Deng, W. Deninger, S. K. Dhawan, V. P. Druzhinin, L. Duong, E. Efstathiadis, F. J. M. Farley, G. V. Fedotovich, S. Giron, F. E. Gray, D. Grigoriev, M. Grosse-Perdekamp, A. Grossmann, M. F. Hare, D. W. Hertzog, X. Huang, V. W. Hughes, M. Iwasaki, K. Jungmann, D. Kawall, M. Kawamura, B. I. Khazin, J. Kindem, F. Krienen, I. Kronkvist, A. Lam, R. Larsen, Y. Y. Lee, I. Logashenko, R. McNabb, W. Meng, J. Mi, J. P. Miller, Y. Mizumachi, W. M. Morse, D. Nikas, C. J. G. Onderwater, Y. Orlov, C. S. Özben, J. M. Paley, Q. Peng, C. C. Polly, J. Pretz, R. Prigl, G. zu Putlitz, T. Qian, S. I. Redin, O. Rind, B. L. Roberts, N. Ryskulov, S. Sedykh, Y. K. Semertzidis, P. Shagin, Y. M. Shatunov, E. P. Sichtermann, E. Solodov, M. Sossong, A. Steinmetz, L. R. Sulak, C. Timmermans, A. Trofimov, D. Urner, P. von Walter, D. Warburton, D. Winn, A. Yamamoto, and D. Zimmerman, "Final report of the e821 muon anomalous magnetic moment measurement at bnl," Phys. Rev. D **73**, 072003 (2006).

[134] S. Weinberg, *The Quantum theory of fields. Vol. 1: Foundations* (Cambridge University Press, 2005), 3rd ed.

[135] W. H. Furry, "On bound states and scattering in positron theory," Physical Review **81**, 115 (1951).

[136] C. Itzykson and J.-B. Zuber, *Quantum field theory* (Dover, 2005).

[137] M. E. Peskin and D. V. Schroeder, *An Introduction to quantum field theory* (Addison-Wesley, 1995).

[138] V. Shabaev, "Two-time green's function method in quantum electrodynamics of high-z few-electron atoms," Physics Reports **356**, 119 (2002).

[139] E. A. Uehling, "Polarization effects in the positron theory," Physical Review **48**, 55 (1935).

[140] E. H. Wichmann and N. M. Kroll, "Vacuum polarization in a strong coulomb field," Physical Review **101**, 843 (1956).

[141] G. Källen, "Fourth order vacuum polarization," K. Dan. Vidensk. Selsk. Mat.-Fys. Medd. **29**, No (1955).

[142] L. W. Fullerton and G. A. Rinker, "Accurate and efficient methods for the evaluation of vacuum-polarization potentials of order $z\alpha$ and $z\alpha^2$," Phys. Rev. A **13**, 1283 (1976).

[143] A. A. Elizarov, V. M. Shabaev, N. S. Oreshkina, and I. I. Tupitsyn, "Hyperfine splitting in heavy ions with the nuclear magnetization distribution determined from experiments on muonic atoms," Nucl. Instrum. Methods Phys. Res. B **235**, 65 (2005).

[144] R. Barbieri, J. A. Mignaco, and E. Remiddi, "On the fourth-order radiative corrections to the electron-photon vertex," Lettere al Nuovo Cimento (1969-1970) **3**, 588 (1970).

[145] R. Barbieri, J. A. Mignaco, and E. Remiddi, "Electron form factors up to fourth order. - i," Il Nuovo Cimento A (1965-1970) **11**, 824 (1972).

[146] R. Barbieri, J. A. Mignaco, and E. Remiddi, "Electron form factors up to fourth order. - ii," Il Nuovo Cimento A (1965-1970) **11**, 865 (1972).

[147] R. Barbieri and E. Remiddi, "Infra-red divergences and adiabatic switching. fourth-order vaccum polarization," Il Nuovo Cimento A (1965-1970) **13**, 99 (1973).

[148] P. Indelicato, "Nonperturbative evaluation of some qed contributions to the muonic hydrogen $n = 2$ lamb shift and hyperfine structure," Phys. Rev. A **87**, 022501 (2013).

[149] V. M. Shabaev, I. I. Tupitsyn, V. A. Yerokhin, G. Plunien, and G. Soff, "Dual kinetic balance approach to basis-set expansions for the dirac equation," Phys. Rev. Lett. **93**, 130405 (2004).

[150] D. A. Varshalovich, A. N. Moskalev, and V. K. Khersonskii, *Quantum Theory of Angular Momentum* (World Scientific, Singapore, 1988).

[151] M. Rose, *Relativistic Electron Theory* (John Wiley and Sons, 1961).

[152] W. R. Johnson, S. A. Blundell, and J. Sapirstein, "Finite basis sets for the dirac equation constructed from b splines," Physical Review A **37**, 307 (1988).

[153] G. W. F. Drake and S. P. Goldman, "Application of discrete-basis-set methods to the dirac equation," Physical Review A **23**, 2093 (1981).

[154] F. Köhler, S. Sturm, A. Kracke, G. Werth, W. Quint, and K. Blaum, "The electron mass from g -factor measurements on hydrogen-like carbon 12 c 5+," J. Phys. B: At. Mol. Opt. Phys. **48**, 144032 (2015).

[155] F. Köhler, K. Blaum, M. Block, S. Chenmarev, S. Eliseev, D. A. Glazov, M. Goncharov, J. Hou, A. Kracke, D. A. Nesterenko, Y. N. Novikov, W. Quint, E. Minaya Ramirez, V. M. Shabaev, S. Sturm, A. V. Volotka, and G. Werth, "Isotope dependence of the zeeman effect in lithium-like calcium," Nature Communications **7**, 10246 EP (2016).

[156] H.-J. Kluge *et al.*, "Chapter 7 hitrap: A facility at gsi for highly charged ions," in "Current Trends in Atomic Physics," , vol. 53 of *Advances in Quantum Chemistry*, S. Salomonson and E. Lindroth, eds. (Academic Press, 2008), pp. 83 – 98.

[157] V. A. Yerokhin, P. Indelicato, and V. M. Shabaev, "Evaluation of the self-energy correction to the *g* factor of *s* states in h-like ions," Phys. Rev. A **69**, 052503 (2004).

[158] A. Czarnecki and R. Szafron, "Light-by-light scattering in the lamb shift and the bound electron *g* factor," Phys. Rev. A **94**, 060501 (2016).

[159] V. M. Shabaev, "Finite nuclear size corrections to the energy levels of the multi-charged ions," J. Phys. B: At. Mol. Opt. Phys. **26**, 1103 (1993).

[160] Y. S. Kozhedub, O. V. Andreev, V. M. Shabaev, I. I. Tupitsyn, C. Brandau, C. Kozhuharov, G. Plunien, and T. Stöhlker, "Nuclear deformation effect on the binding energies in heavy ions," Phys. Rev. A **77**, 032501 (2008).

[161] S. G. Karshenboim and V. G. Ivanov, "Finite-nuclear-size contribution to the *g* factor of a bound electron: Higher-order effects," Phys. Rev. A **97**, 022506 (2018).

[162] J. D. Jackson, *Classical electrodynamics* (Wiley, New York, 1999), 3rd ed.

[163] S. G. Karshenboim, R. N. Lee, and A. I. Milstein, "*g* factor of an electron or muon bound by an arbitrary central potential," Phys. Rev. A **72**, 042101 (2005).

[164] B. Hahn, D. G. Ravenhall, and R. Hofstadter, "High-energy electron scattering and the charge distributions of selected nuclei," Phys. Rev. **101**, 1131 (1956).

[165] I. Angeli and K. Marinova, "Table of experimental nuclear ground state charge radii: An update," Atomic Data and Nuclear Data Tables **99**, 69 (2013).

[166] F. Träger, "On the charge distribution of calcium nuclei," Zeitschrift für Physik A Hadrons and Nuclei **299**, 33 (1981).

[167] V. M. Shabaev, I. I. Tupitsyn, V. A. Yerokhin, G. Plunien, and G. Soff, "Dual kinetic balance approach to basis-set expansions for the dirac equation," Phys. Rev. Lett. **93**, 130405 (2004).

[168] N. Michel, *Precision Physics of the Bound Electron g-factor* (Master Thesis, Ruprecht-Karls-Universität, Heidelberg; http://hdl.handle.net/11858/00-001M-0000-0028-48C8-0, 2015).

[169] Evaluated Nuclear Structure Data Files (ENSDF) (http://www.nndc.bnl.gov/ensdf/).

[170] P. Ring and P. Schuck, *The Nuclear Many-Body Problem* (Springer-Verlag, 1980).

[171] D. A. Close, J. J. Malanify, and J. P. Davidson, "Nuclear charge distributions deduced from the muonic atoms of ^{232}th, ^{235}u, ^{238}u, and ^{239}pu," Phys. Rev. C **17**, 1433 (1978).

[172] P. Möller *et al.*, "Nuclear ground-state masses and deformations," At. Data Nucl. Data Tables **59**, 185 (1995).

[173] L. W. Wansbeek, S. Schlesser, B. K. Sahoo, A. E. L. Dieperink, C. J. G. Onderwater, and R. G. E. Timmermans, "Charge radii of radium isotopes," Phys. Rev. C **86**, 015503 (2012).

[174] H. D. Vries, C. D. Jager, and C. D. Vries, "Nuclear charge-density-distribution parameters from elastic electron scattering," Atomic Data and Nuclear Data Tables **36**, 495 (1987).

[175] L.-B. Wang, P. Mueller, K. Bailey, G. W. F. Drake, J. P. Greene, D. Henderson, R. J. Holt, R. V. F. Janssens, C. L. Jiang, Z.-T. Lu, T. P. O'Connor, R. C. Pardo, K. E. Rehm, J. P. Schiffer, and X. D. Tang, "Laser spectroscopic determination of the ^{6}He nuclear charge radius," Phys. Rev. Lett. **93**, 142501 (2004).

[176] H. De Witte, A. N. Andreyev, N. Barré, M. Bender, T. E. Cocolios, S. Dean, D. Fedorov, V. N. Fedoseyev, L. M. Fraile, S. Franchoo, V. Hellemans, P. H. Heenen, K. Heyde, G. Huber, M. Huyse, H. Jeppessen, U. Köster, P. Kunz, S. R. Lesher, B. A. Marsh, I. Mukha, B. Roussière, J. Sauvage, M. Seliverstov, I. Stefanescu, E. Tengborn, K. Van de Vel, J. Van de Walle, P. Van Duppen, and Y. Volkov, "Nuclear charge radii of neutron-deficient lead isotopes beyond $n = 104$ midshell investigated by in-source laser spectroscopy," Phys. Rev. Lett. **98**, 112502 (2007).

[177] P. Mueller, I. A. Sulai, A. C. C. Villari, J. A. Alcántara-Núñez, R. Alves-Condé, K. Bailey, G. W. F. Drake, M. Dubois, C. Eléon, G. Gaubert, R. J. Holt, R. V. F. Janssens, N. Lecesne, Z.-T. Lu, T. P. O'Connor, M.-G. Saint-Laurent, J.-C. Thomas, and L.-B. Wang, "Nuclear charge radius of ^{8}He," Phys. Rev. Lett. **99**, 252501 (2007).

[178] K. Kirch, "Slow Muons and Muonium," ArXiv e-prints (2016).

[179] P. J. Mohr, D. B. Newell, and B. N. Taylor, "Codata recommended values of the fundamental physical constants: 2014," Rev. Mod. Phys. **88**, 035009 (2016).

[180] W. Zickendraht, "Why are most nuclei axially symmetric?" Annalen der Physik **503**, 229 (1991).

[181] W. R. Johnson, *Atomic Structure Theory* (Springer, Berlin Heidelberg, 2007), 1st ed.

[182] T. Beier, "The gj factor of a bound electron and the hyperfine structure splitting in hydrogenlike ions," Physics Reports **339**, 79 (2000).

[183] L. D. Landau and L. M. Lifshitz, *Quantum Mechanics Non-Relativistic Theory, Third Edition: Volume 3* (Butterworth-Heinemann, 1981), 3rd ed.

[184] J. Friar and J. Negele, "Breit equation analysis of recoil corrections to muonic atom energy levels," Physics Letters B **46**, 5 (1973).

[185] P. Vogel, "Electron screening in muonic atoms," Phys. Rev. A **7**, 63 (1973).

[186] H. Bethe and E. Salpeter, *Quantum Mechanics of One- and Two-Electron Systems* (Plenum Publishing Corporation, 1977).

[187] E. Y. Korzinin, N. S. Oreshkina, and V. M. Shabaev, "Hyperfine splitting of low-lying levels in heavy li-like ions," Physica Scripta **71**, 464 (2005).

[188] N. J. Stone, "Table of nuclear magnetic dipole and electric quadrupole moments," Atomic Data and Nuclear Data Tables **90**, 75 (2005).

[189] A. Bohr and V. F. Weisskopf, "The influence of nuclear structure on the hyperfine structure of heavy elements," Phys. Rev. **77**, 94 (1950).

[190] R. M. Steffen, "Precision measurements of nuclear quadrupole moments by muonic x-rays," Hyperfine Interactions **24**, 223 (1985).

[191] J. J. Sakurai, *Modern Quantum Mechanics* (Addison-Wesley, 1994), 2nd ed.

[192] "*NIST Digital Library of Mathematical Functions*," http://dlmf.nist.gov/, Release 1.0.19 of 2018-06-22. F. W. J. Olver, A. B. Olde Daalhuis, D. W. Lozier, B. I. Schneider, R. F. Boisvert, C. W. Clark, B. R. Miller and B. V. Saunders, eds.

[193] V. Pisano, G. Puddu, P. Quarati, and L. Sulis, "The use of the master equation in the cascade of exotic systems in a pure coulomb field," Il Nuovo Cimento A (1965-1970) **72**, 27 (1982).

[194] W. Dey, P. Ebersold, H. Leisi, F. Scheck, H. Walter, and A. Zehnder, "Nuclear spectroscopic ground-state quadrupole moments from muonic atoms," Nuclear Physics A **326**, 418 (1979).

[195] S. D. Wit, G. Backenstoss, C. Daum, J. Sens, and H. Acker, "Measurement and analysis of muonic x-ray spectra in deformed nuclei," Nuclear Physics **87**, 657 (1966).

[196] B. Fricke, "Zur vakuumpolarisation in myonenatomen," Zeitschrift für Physik A Hadrons and nuclei **218**, 495 (1969).

[197] J. Pearson, "Vacuum polarization induced by the nuclear quadrupole moment in mu-mesonic atoms," Nuclear Physics **45**, 401 (1963).

[198] M.-y. Chen, "Nuclear polarization in muonic atoms of deformed nuclei," Phys. Rev. C **1**, 1176 (1970).

[199] W. R. Inc., "Mathematica, Version 11.3," Champaign, IL, 2018.

[200] F. Johansson *et al.*, *mpmath: a Python library for arbitrary-precision floating-point arithmetic (version 0.18)* (2013). `http://mpmath.org/`.

[201] H. Schopper, *Nuclear Charge Radii* (Springer, Berlin, Heidelberg, 2004).

[202] J. Konijn, J. Panman, J. Koch, W. V. Doesburg, G. Ewan, T. Johansson, G. Tibell, K. Fransson, and L. Tauscher, "Pionic 4f - 3d transition in 181ta, natural re, and 209bi and the strong interaction level shift and width of the pionic 3d state," Nuclear Physics A **326**, 401 (1979).

[203] "*LTP Experiments*," https://www.psi.ch/ltp/experiments, called 2018-09-20.

[204] "*LTP Facilities*," https://www.psi.ch/ltp/facilities, called 2018-09-20.

[205] N. Stone, "Table of nuclear electric quadrupole moments," Atomic Data and Nuclear Data Tables **111-112**, 1 (2016).

[206] E. Rapisarda, *Private communication* (2018).

[207] S. Vogiatzi, *Master Thesis* (Eidgenössische Technische Hochschule, Zürich, 2018).

[208] J. Schwinger, "On quantum-electrodynamics and the magnetic moment of the electron," Phys. Rev. **73**, 416 (1948).

[209] S. G. Karshenboim, V. G. Ivanov, and V. M. Shabaev, "Vacuum polarization in a hydrogen-like relativistic atom: g factor of a bound electron," J. Exp. Theor. Phys. Lett. **93**, 477 (2001).

[210] A. Peterman, Helv. Phys. Act **30**, 407 (1957).

[211] C. M. Sommerfield, "The magnetic moment of the electron," Ann. Phys. **5**, 26 (1958).

[212] M. I. Eides and H. Grotch, "Gyromagnetic ratios of bound particles," Annals of Physics **260**, 191 (1997).

[213] A. Czarnecki, K. Melnikov, and A. Yelkhovsky, "Anomalous magnetic moment of a bound electron," Phys. Rev. A **63**, 012509 (2000).

[214] S. Laporta and E. Remiddi, "The analytical value of the electron (g - 2) at order α^3 in qed," Phys. Lett. B **379**, 283 (1996).

[215] T. Aoyama, M. Hayakawa, T. Kinoshita, and M. Nio, "Revised value of the eighth-order contribution to the electron g-2," Phys. Rev. Lett. **99**, 110406 (2007).

[216] T. Aoyama, M. Hayakawa, T. Kinoshita, and M. Nio, "Tenth-order qed contribution to the electron g-2 and an improved value of the fine structure constant," Phys. Rev. Lett. **109**, 111807 (2012).

[217] K. Pachucki, "Nuclear mass correction to the magnetic interaction of atomic systems," Phys. Rev. A **78**, 012504 (2008).

[218] H. Grotch, "Electron *g* factor in hydrogenic atoms," Phys. Rev. Lett. **24**, 39 (1970).

[219] A. Czarnecki, B. Krause, and W. J. Marciano, "Electroweak corrections to the muon anomalous magnetic moment," Phys. Rev. Lett. **76**, 3267 (1996).

[220] J. Prades, E. de Rafael, and A. Vainshtein, *The hadronic light-by-light scattering contribution to the muon and electron anomalous magnetic moments* (World Scientific, Singapore, 2010), vol. 20 of *Advanced Series on Directions in High Energy Physics*, chap. 9, pp. 303–317.

[221] D. Nomura and T. Teubner, "Hadronic contributions to the anomalous magnetic moment of the electron and the hyperfine splitting of muonium," Nucl. Phys. B **867**, 236 (2013).

[222] A. Kurz, T. Liu, P. Marquard, and M. Steinhauser, "Hadronic contribution to the muon anomalous magnetic moment to next-to-next-to-leading order," Phys. Lett. B **734**, 144 (2014).

[223] P. J. Mohr, D. B. Newell, and B. N. Taylor, "Codata recommended values of the fundamental physical constants: 2014," Rev. Mod. Phys. **88**, 035009 (2016).

[224] A. Edmonds, *Angular Momentum in Quantum Mechanics* (Princeton University Press, 1960), 2nd ed.

[225] J. Brown and A. Carrington, *Rotational Spectroscopy of Diatomic Molecules* (Cambridge University Press, 2003).

[226] B. Podolsky, "Quantum-mechanically correct form of hamiltonian function for conservative systems," Phys. Rev. **32**, 812 (1928).

[227] R. d. L. Kronig and I. I. Rabi, "The symmetrical top in the undulatory mechanics," Phys. Rev. **29**, 262 (1927).

Acknowledgements

In the end, I want to express my gratitude to all people who contributed to this thesis:
First of all, I want to thank my supervisors Prof. Christoph H. Keitel and Dr. Natalia S. Oreshkina for the possibility to work on my phd project at such a prestigious institute and inspiring environment; for the numerous discussions, helpful advice, and at the same time enough space for following my own ideas.

I wish to thank PD Dr. Wolfgang Quint for his efforts in being the second referee and Prof. Maurits W. Haverkort and Prof. Kurt Roth for being part of the examination committee.

Furthermore, I am very thankful to Dr. Elisa Rapisarda, Dr. Aldo Antognini, Dr. Andreas Knecht, Stella M. Vogiatzi, and everyone else from the MuX collaboration. It was a great motivation and inspiration to have a theoretical project which is at the same time closely connected to exciting experiments.

I want to thank my office colleagues Shika Bhadoria, Jiri Danek, Kamil Dzikowski, Jonas Gunst, Nicolas Teeny, and all other division members for the good atmosphere, nice conversations and interesting discussions in the office and during breaks.

Many thanks to Natalia, Shikha, Bastian, Halil, Jiri, Kamil, and Zoltan for proof reading the thesis.

Finally, I am deeply grateful to my family and to Kasia for their love and support, especially during my time as a doctoral student.